UNIVERSITE DE MONS-HAINAUT

Faculté des Sciences
Service de Physique Générale et de Physique des
Particules Elémentaires

Asymmetry measurement of strange quark production in e^+e^- interactions at LEP at the Z^0 mass.

Kathy HUET
1997

Thèse présentée pour
l'obtention du grade légal
de Docteur en Sciences

PRÉFACE

LETTRE A MA FILLE ...

La THÈSE est le point d'orgue du parcours universitaire.
Elle empanache son concepteur d'une aura particulière : l'ouvrage prend dignement place sur les rayons de la bibliothèque du discours scientifique.

La Thèse marque l'aboutissement d'un héritage.
Elle prouve la pertinence de l'effort.

La Thèse achève la cérémonie rituelle de reconnaissance scientifique. Elle est la lettre de créance de l'utilité scientifique et sociale et de la compétence du chercheur.

Le cérémonial de cet ultime passage démontre cela : les lecteurs se partagent le double rôle du dedans et du dehors. Si le discours du chercheur est buissonnier, il est néanmoins inscrit dans le paysage mental du discours scientifique tel qu'il est dessiné par les architectures ou les urbanistes du savoir.

L'aveu final de cette reconnaissance s'effectue dans un dernier combat.
La présentation de l'oeuvre s'assure une défense.
Le jury enquête et le candidat plaide : il est une dernière fois suspecté.
Dans le maquis du savoir et du pouvoir, la Thèse est le mot de passe de l'adoubement scientifique et social.
La Thèse est l'exposé d'une requête : une demande de filiation.

Si la Thèse est exposé, elle est aussi témoignage.
Témoigner est apporter des preuves. Prouver c'est montrer une capacité. Dire sa capacité, c'est nommer sa compétence. Etre compétent, c'est signifier son utilité.

La Thèse se rattache à une tradition humaniste et universitaire qui apprécie le formel et qui consacre le mot.
Ne vaut que ce qui se nomme.
L'écrit consacre la maîtrise de la chose : pas de religion, sans prophétie, pas de sorcellerie sans formule, pas de politique sans discours.
Le mot exorcise l'action. Le mot convoque l'action.

L'écrit est une valeur de culture et de civilisation ;
L'écrit est trace ineffaçable. Il enracine le présent.
La Thèse rend infiniment présent : elle est le temps continué, prolongé.

La Thèse serait le repère archéologique de notre savoir.

La Thèse surpasse en importance tout le reste.
Non seulement elle paraphe le parcours universitaire mais elle le mesure à lui tout seul.

Chère Kathy,

Durant vingt-trois ans, tu t'es précipitée aux sources de la connaissance.
Durant vingt-trois ans, tu as ingéré, tu as digéré, tu as mâché, tu as trituré de nombreux champs du savoir.
Durant vingt-trois ans, tu as réfléchi, tu as exercé, tu as affiné tes compétences et tes qualités.
Durant vingt-trois ans, à l'appui de tes travaux, tu as exprimé ta réflexion, son étendue et sa diversité.

Eh bien ! Sais-tu quoi ?

Tout cela n'est rien. Rien, tu m'entends, rien.

La Thèse, en quelque sorte, entérine dans sa sanction l'incompétence de ta pratique, de ton savoir et son inconvenance sociale et scientifique.

Tout sera à recommencer ... Si tu le veux !

Voilà ce que m'inspire, vois-tu, la rédaction de ta Thèse.
Elle s'inscrit dans un ensemble.
Elle participe à ce jeu scientifique et social dont j'essaie en vain de te dessiner les imbrications complémentaires.

Tu arrives à la fin mais tu auras l'impression d'être au seuil.
Débutant ta formation universitaire et scientifique, tu t'interrogeais sur son issue.
L'achevant, tu vas questionner tes commencements.
Tu vas remiser le doute, non la certitude de la question.

Choisis donc l'interrogation de l'éternel recommencement.
L'interrogation du choix devient questionnement du soi.
L'itinéraire scientifique et social devient cheminement de l'incontournable et de l'indicible.
Soi-même à soi-même toujours répété.

Tout est en place. Le savoir est posé, la connaissance est assise, l'expérience est réfléchie.

Tout est en place... Tout peut commencer.

J'avais cru de bonne foi achever ma péripétie préfacielle.
Un hoquet a étouffé ma relecture.
Je me suis précipité sur ma plume implorant les mânes de nos ancêtres qui ont déjà gagné leur salut et les dieux irascibles qui m'auraient alors volé le mien.

J'ai eu une curieuse impression.
La ressemblance de nos traits m'a frappé.

Je me suis dit : tiens comme le lien familial déteint !

Ce sera le mot de notre fin provisoire.

Chère Kathy, bonne route...

Jean Huet.

A mes parents.
A Bernard.

" L'esprit expérimental accomplit sa marche en s'appuyant à chaque pas sur l'observation des faits et des situations. Il soumet la pensée à l'expérience et recherche la réalité objective. Il possède l'art d'interroger correctement la nature et de lui poser des questions justes, soucieux de vérifier rigoureusement les réponses par un contrôle méthodique. Ce souci prédominant d'objectivité lucide et modeste conduit l'homme à subordonner ses idées, ses jugements et ses normes non pas à des opinions toutes faites répandues dans un milieu, ni à des sentiments si élevés soient-ils, ni à des principes même traditionnels, mais à l'expérience des faits."

Pierre Angers in "Problèmes de culture au Canada français", Montréal, Beauchemin, 1961.

Acknowledgements

This thesis is the fruit of the work of many people, directly or indirectly. I willingly take here the opportunity to thank all of them.

First of all, I would like to express my gratitude to my supervisor Prof. Philippe Herquet for having accepted me into his experimental group of the University of Mons. He also deserves a special thank for his valuable guidance and helpful suggestions during my time as Ph.D student, for the thorough remarks while writing this thesis and his proof-reading.

I am greatly indebted to Prof. Fernand Grard for our many fruitful discussions (in particular about theoretical questions), his unconditional support and good advice.

This thesis would not have been possible without the tremendous work performed by all the technicians, engineers and physicists of the DELPHI collaboration in providing excellent performance of the detector.
During my frequent stays at CERN, I enjoyed working in the DELPHI RICH group. I greatly profited from our pit shifts during which I learned a lot operating the RICH detectors. In particular, I owe very much to Dr. Peter Kluit for extensively explaining me the complexity of the RICH detectors and the analysis procedure of their raw data.
I would like to thank also my other colleagues of the 's-inclusive' analysis team and especially M. Dracos and F. Scuri for their judicious comments.

I want to extend my thanks to Prof. Pierre Gillis for having proposed me an interesting subject for my "thèse annexe" and for having helped me to develop it within the RMN group of Mons University.

Finally, special thanks to all my colleagues of Mons : Sophie and Arnaud for our giggles, Evelyne and Isabelle for our 'hardware' lunch time. Joseph, Biscuit and Francis for their logistic support, Jacqueline for her strong coffee ... as well as my other colleagues that I did not mention specifically.

Last but not least, I warmly acknowledge my family for their patience and continuous encouragements to reach this goal.

Outlines

According to the Standard Model, theoretical model which describes the strong and electroweak interactions, the fermion-antifermion pairs resulting from the collisions between electrons and positrons at centre-of-mass energies close to the Z^0 mass, are emitted in an asymmetric way with respect to the direction of incidence. This forward-backward asymmetry in the case of the production of $b\bar{b}$ and $c\bar{c}$ pairs has been measured by experiments at the LEP collider. The measurement of the production asymmetry of $s\bar{s}$ pairs is an important complementary test of the Standard Model.
In this thesis, we present for the first time in details a measurement of the $s\bar{s}$ asymmetry from the analysis of the data collected in 1994 at LEP with the DELPHI detector. Actually, the $s\bar{s}$ asymmetry has been deduced from the angular distribution of high momentum charged kaons which have been identified individually thanks to the unique facility of DELPHI with its Barrel and Forward RICH detectors. Therefore, this measurement depends on the thorough knowledge and control of the performances of such detectors.
The original method that we have settled to extract the $s\bar{s}$ asymmetry from the experimental charged kaon asymmetry allowed us to obtain the following precise value : $A^0_{s\bar{s}} = 0.114 \pm 0.019(stat.) \pm 0.005(syst.)$.

The present thesis is organised as follows :
In chapter 1, the theoretical context of the Standard Model is presented.

A description of the experimental apparatus with emphasis on the new developments and performances since the DELPHI detector has been just in operation is given in chapter 2. The end of the chapter is devoted to the procedure used to convert raw data produced by the detector into standard physics quantities and to the simulation program used to verify the significance of the measurements.

The definition of the Cherenkov effect, the description of the Ring Imaging CHerenkov detectors which equip the DELPHI experiment as well as their performances are given in chapter 3.

In chapter 4, the presentation of the theoretical formalism used to describe the process $e^+e^- \rightarrow Z^0 \rightarrow s\bar{s}$ with emphasis on cross-section and asymmetry is presented.

Chapter 5 and 6 cover the present measurement with a description of the experimental procedures relevant for the analysis in the former and the complete and detailed presentation of the method used and the results obtained in the latter.

We conclude in chapter 7.

Contents

List of Figures

List of Tables

Chapter 1

Theoretical Overview

1.1 Introduction

Identifying the ultimate constituents of matter and understanding the forces that govern their behaviour are fundamental concepts in particle physics. Nowadays, we distinguish four types of fundamental interactions. Two of them act at the macroscopic scale : the Gravity and the Electromagnetic interactions while the two others operate at the atomic nucleus scale : the Strong interaction and the Weak interaction. These four interactions are characterized and distinguishable by their action range and by coupling constants, numbers without dimension which determine the interactions intensity (see table 1.1).

	Gravity	Weak	Electromagnetic	Strong
Range (cm)	∞	$\sim 10^{-15}$	∞	$\sim 10^{-13}$
Lifetime (s)	–	$\sim 10^{-10}$	$\sim 10^{-16}$	$\sim 10^{-22}$
Coupling Constant	10^{-39}	10^{-5}	$\frac{1}{137} \sim 10^{-2}$	1

Table 1.1: The four interactions and their characteristics.

We notice the small value of the Gravity coupling constant which implies that it does not operate at the level of elementary particles.

One distinguishes two families of elementary particles according to the fact

that they are subject or not to the strong interaction : the hadrons and the leptons, respectively.

The lepton family is made of three generations of spin 1/2 particles : the electron (e) and its neutrino (ν_e), the muon (μ) and its neutrino (ν_μ) and the tau (τ) and its neutrino (ν_τ). One of the most important result of LEP100 is that only three types of neutrinos similar to these ones exist (see table 1.2).

Mass ↗	Leptons		Quarks	
	e	ν_e	d	u
	μ	ν_μ	s	c
	τ	ν_τ	b	t
	Spin 1/2 fermions			
Charge	-1	0	$-1/3$	$2/3$

Table 1.2: The elementary particles.

The hadron family is divided into baryons (half spin) and mesons (integer spin). These particles are not considered as elementary anymore but resulting from the assembly of spin 1/2 fundamental particles : quarks (q) and antiquarks ($\overline{q}$) according to a simple and general architecture : baryon $\equiv qqq$, meson $\equiv q\overline{q}$. These fundamental entities of matter show independent properties without being observable at the free state (this leads to the confining hypothesis).

Like the leptons, the quarks are made of three generations (see table 1.2). Unlike the leptons, each quark exists in three different species distinguished by a "colour". The colour acts as a charge to which the Strong interaction is sensitive.

All the fundamental interactions (except Gravity) are described by theoretical models which present the same mathematical structure characteristic of gauge theories.
According to gauge theories, the interactions between the matter particles (leptons and quarks) would result from the exchange of vector bosons called gauge bosons.

The first of these theories is the Quantum Electro Dynamics (QED) which, at low energy, describes satisfactorily the electromagnetic interaction, the

interaction between charged particles through the exchange of a photon.

This theory has then been extended to lead to the Weinberg-Salam model [3] : a gauge theory elaborated to describe weak and electromagnetic processes (exchange of $W^{\pm}$, Z^0 and γ, respectively) in the same theoretical framework.

The gauge theory describing the strong interaction between quarks is called Quantum Chromo Dynamics (QCD). In this case, quarks interact through the exchange of coloured gauge bosons called gluons. Together with the Weinberg-Salam model, QCD forms the so-called Standard Model (SM).

1.2 The gauge theories

In the framework of a Lagrangian field theory, the dynamics is specified by the Lagrangian density $\mathcal{L}$, which is a function of the various fields ψ_i and their space-time derivatives $\partial_\mu \psi_i$:

$$\mathcal{L} = \mathcal{L}(\psi_i, \partial_\mu \psi_i) \tag{1.1}$$

The index i stands for the different types of matter fields of interest (we drop this index i for simplicity).

A gauge theory, a particular class of field theories, is built on a local symmetry property : a physics system made of interacting matter particles (leptons and quarks) shows a local symmetry if the controlling rule of its time evolution is invariant under a transformation group which can be applied differently at each space-time point.

The construction of such a gauge theory starts from a Lagrangian for free matter particles which is invariant under a group of global transformations (same at each space-time point). This Lagrangian is then transformed such as to be invariant for local transformations. This can only be achieved by the introduction, in the Lagrangian density, of vector fields (the gauge fields). It happens that these gauge fields interact with matter fields in a well prescribed manner.

A gauge theory describes then the interaction between matter particles through the exchange of vector bosons, particles associated to the gauge fields.

In the so-elaborated formalism, these gauge bosons are massless which leads

to interactions of infinite range. Such a theory is thus not suitable to describe the weak interaction which is short range and therefore requires the exchange of corresponding heavy bosons. This problem has been solved by using the so-called Higgs mechanism (section 1.3).

What follows is partially inspired by the Maiani CERN School lectures [1].

1.2.1 The Quantum Electro Dynamics (QED)

Quantum Electro Dynamics is the classical gauge theory which describes the interaction between charged particles through the exchange of photons.

This gauge theory is based on the symmetry group U(1) and can be built as described below :

• We consider a Lagrangian density for free charged fermions $\mathcal{L}_{free}$ which satisfies the global symmetry U(1). For each charged fermion (spin 1/2 fields) the corresponding Lagrangian can be written as :

$$\mathcal{L}_{free} = \overline{\psi}(i\gamma^\mu \partial_\mu - m)\psi \tag{1.2}$$

γ^μ are the 4x4 Dirac matrices (see appendix A) and ψ is a Dirac spinor. $\mathcal{L}_{free}$ is invariant under global phase transformations such as :

$$\psi \longrightarrow \psi' = \psi e^{i\alpha} \tag{1.3}$$

with α being a constant.

• The "minimal prescription", is then adopted. It consists in replacing the derivatives ∂_μ by the covariant derivatives D_μ :

$$\partial_\mu \longrightarrow D_\mu \equiv \partial_\mu + ieA_\mu \tag{1.4}$$

A_μ being vector fields and e being an arbitrary constant.

For each matter fermion, we obtain the following new Lagrangian density $\mathcal{L}(\psi, D_\mu\psi)$:

$$\begin{aligned} \mathcal{L}(\psi, D_\mu\psi) &= \overline{\psi}(i\gamma^\mu(\partial_\mu + ieA_\mu) - m)\psi \\ &= \overline{\psi}(i\gamma^\mu\partial_\mu - m)\psi - e\overline{\psi}\gamma^\mu A_\mu\psi \\ &= \mathcal{L}_{free} + \mathcal{L}_{int} \end{aligned} \tag{1.5}$$

with

$$\mathcal{L}_{int} = -e\overline{\psi}\gamma^\mu A_\mu\psi$$

which expresses the interaction of the matter field ψ with the electromagnetic field A_μ. The above constant e acts as the electric charge.

We notice that the Lagrangian density $\mathcal{L}(\psi, D_\mu\psi)$ is invariant under :

$$\psi \longrightarrow \psi' = \psi \exp^{\alpha(x)} \tag{1.6}$$

with $\alpha(x)$ an arbitrary function of the space-time coordinates x, if the electromagnetic field simultaneously transforms as :

$$A_\mu \longrightarrow A'_\mu = A_\mu - \frac{1}{e}\partial_\mu\alpha(x) \tag{1.7}$$

In such a way, $D_\mu\psi$ transforms as ψ :

$$D_\mu\psi \longrightarrow (D_\mu\psi)' = D_\mu(\psi \exp^{i\alpha(x)}) \tag{1.8}$$

• The Lagrangian density $\mathcal{L}(\psi, D_\mu)$ has to be completed by a kinetic energy term for the electromagnetic field A_μ (to describe the propagation of the gauge fields (Klein-Gordon equation)) :

$$\mathcal{L}_{\text{YM}} = -\frac{1}{4}F_{\mu\nu}(x)F^{\mu\nu}(x) \tag{1.9}$$

called the gauge invariant Yang-Mills Lagrangian density, where

$$F_{\mu\nu}(x) = \partial_\mu A_\nu(x) - \partial_\nu A_\mu(x) \tag{1.10}$$

is the electromagnetic tensor whose elements are the different cartesian components of the electric field $\overrightarrow{E}$ and of the magnetic field $\overrightarrow{H}$. These elements are invariant under the gauge transformations 1.7.

The total Lagrangian density can finally be written for matter fermions as :

$$\mathcal{L}_{tot} = \mathcal{L}_{free} + \mathcal{L}_{int} + \mathcal{L}_{\text{YM}} \tag{1.11}$$

1.2.2 The Weak Interaction

A theory which describes the weak interaction (appearing in the nuclear β-decays) was formulated for the first time in 1934 by Fermi.

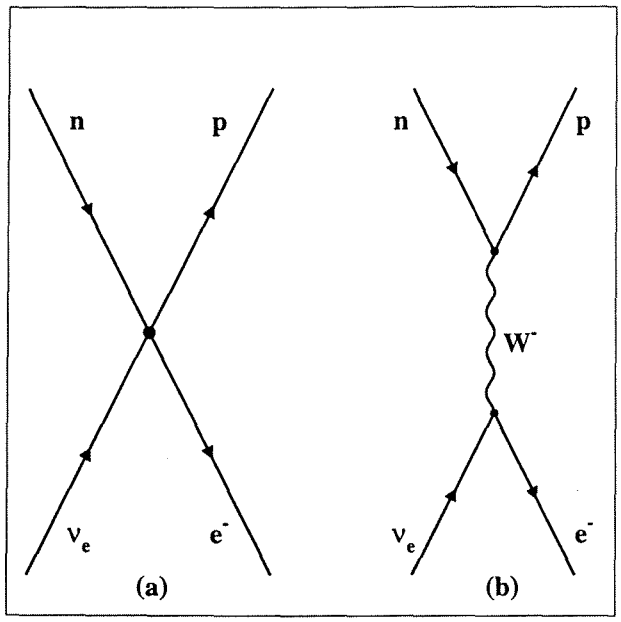

Figure 1.1: β-decay in the weak interaction : (a) according to the Fermi point-like theory; (b) the same interaction explained in terms of the exchange of a $W^{\pm}$ boson.

This theory describes the interaction $n \rightarrow p + e^- + \nu_e$ as a four-particle contact interaction as shown in figure 1.1(a).

The (relativist invariant) amplitude is written in its general form as the sum of Lorentz invariant terms of the type " product of two currents and a coupling constant " :

$$A = \sum_i G_i(\overline{\psi}_p O_i \psi_n)(\overline{\psi}_e O_i \psi_\nu) \tag{1.12}$$

where :

- ψ_k are Dirac spinors $(k = p, e, n, \nu)$
- the index i represents the different covariant forms : Scalar (S), Vector (V), Axial (A), Tensor (T) and Pseudo-Scalar (PS)
- G_i is the coupling constant relative to the interaction i

- O_i is the matrix operator corresponding to the interaction i :
  - S : $O_i = 1$
  - V : $O_i = \sum_\mu \gamma^\mu$
  - A : $O_i = \sum_\mu \gamma^\mu \gamma^5$
  - T : $O_i = \sum_\mu \sum_{\nu \neq \mu} \gamma^\mu \gamma^\nu$
  - PS : $O_i = \gamma^5$

In 1956, Lee and Yang concluded that the weak interactions do not conserve parity, and thus that the theory is not invariant under spatial inversion.

The Fermi theory (for which experimental results had already rejected S, PS, and T interactions) was then reformulated such as to allow for parity non-conservation and to take into account the experimentally observed (V-A) behaviour of the weak interaction, leading to the so-called V-A theory in which the amplitude for such a process (figure 1.1(a)) is proportional to :

$$A \div G(\overline{\psi}_p \gamma^\mu (1-\gamma^5)\psi_n)(\overline{\psi}_e \gamma^\mu (1-\gamma^5)\psi_\nu) \tag{1.13}$$

But according to this point-like interaction theory, neutrino-nucleon interaction cross-sections would increase to infinity with energy and would violate the "unitarity limit". A solution to this problem was found by considering that the weak interaction proceeds through the exchange, between matter particles, of bosons called "intermediate vector bosons", W^+ and W^- (see figure 1.1(b)), instead of occurring at a unique point.

At low energies, the weak interaction is well described by the Fermi theory. So, if weak interactions are to be mediated by vectors bosons (W), these must be heavy enough to reflect the corresponding short range behaviour of this interaction. This is a consequence of an exchange model : mass is in inverse proportion to range.

Some years afterwards (1973), the neutral currents have been discovered in neutrino-nucleon interactions. This discovery led to postulate the existence of a third intermediate vector boson : the electrically neutral Z^0 which (together with the W^+ and W^- bosons) has effectively been found at the CERN $p\bar{p}$ collider [2]. It was the first experimental verification of the model elaborated in 1968 by S. Weinberg and A. Salam.

S. Weinberg and A. Salam proposed a gauge theory to unify weak and electromagnetic interactions. The procedure to build a gauge theory as see in subsection 1.2 can be generalised to the SU(2)×U(1) group as follows :

• We start from a Lagrangian density $\mathcal{L} = \sum_i \mathcal{L}(\psi_i, \partial_\mu \psi_i)$ for free particles globally invariant under the group SU(2)×U(1), i.e for the following infinitesimal transformations :

$$\psi_i \longrightarrow \psi_i' = \psi_i + i\epsilon^a \frac{\tau_a}{2}\psi_i + i\epsilon' \frac{1}{2}\mathbb{1}\psi_i \tag{1.14}$$

where :

- a=(1,2,3)
- ψ_i are Dirac isospinors satisfying equation 1.2, the Dirac equation.
- The index i stands for all types of isospinors of fermions.
- ϵ^a and ϵ' are arbitrary infinitesimal constant parameters.
- $\mathbb{1}$ is the 2×2 unit matrix.
- τ_a are the 2×2 Pauli matrices[1] which represents the SU(2) group generators. They satisfy the commutation rules :

$$[\frac{\tau_a}{2}, \frac{\tau_b}{2}] = i\epsilon_{abc}\frac{\tau_c}{2}$$

where ϵ_{abc} is the totally antisymmetric tensor[2].

• We then transform the Lagrangian density $\mathcal{L}(\psi_i, \partial_\mu \psi_i)$ into a Lagrangian density which is invariant under local transformations (transformation 1.14 with $\epsilon^a \equiv \epsilon^a(x)$ and $\epsilon' \equiv \epsilon'(x)$) via the minimal prescription :

$$\partial_\mu \longrightarrow \nabla_\mu \equiv \partial_\mu + igA_\mu^a \frac{\tau_a}{2} + ig' B_\mu^a \frac{1}{2}\mathbb{1} \tag{1.15}$$

with the introduction of :

[1]
$$\tau_1 = \begin{pmatrix} 0 & 1 \\ 1 & 0 \end{pmatrix} \quad \tau_2 = \begin{pmatrix} 0 & -i \\ i & 0 \end{pmatrix} \quad \tau_3 = \begin{pmatrix} 1 & 0 \\ 0 & 1 \end{pmatrix}$$

[2]
$$\epsilon_{abc} = \begin{cases} +1 & \text{if } \{abc\} \text{ is an even permutation of } \{123\} \\ -1 & \text{if } \{abc\} \text{ is an odd permutation of } \{123\} \\ 0 & \text{otherwise} \end{cases}$$

- four vector fields (gauge fields), one per generator :
  - an isotriplet A^a_μ (a=1,2,3) for the SU(2) group
  - a singlet B_μ for the U(1) group
- two arbitrary constants, one per group :
  - g for the SU(2) group
  - g' for the U(1) group

The resulting Lagrangian density $\mathcal{L}(\psi, \nabla_\mu \psi)$ is invariant if the four introduced gauge fields are simultaneously transformed as follows :

$$\begin{aligned} A^a_\mu &\longrightarrow A^a_\mu - \epsilon_{abc}\epsilon^b(x)A^c_\mu - \frac{1}{g}\partial_\mu \epsilon^a(x) \\ B_\mu &\longrightarrow B_\mu - \frac{1}{g'}\partial_\mu \epsilon'(x) \end{aligned} \tag{1.16}$$

It describes the interaction between matter particles through the exchange of gauge bosons associated to the gauge fields, g and g' acting as coupling constants.

• The resulting Lagrangian $\mathcal{L}(\psi, \nabla_\mu \psi)$ has to be completed by the gauge invariant Yang-Mills Lagrangian density to describe the propagation of the gauge fields (they must obey the Klein- Gordon equation) :

$$\mathcal{L}_{\mathrm{YM}} = -\frac{1}{4}F^a_{\mu\nu}(F^a)^{\mu\nu} - \frac{1}{4}G_{\mu\nu}G^{\mu\nu} \tag{1.17}$$

where

$$\begin{aligned} F^a_{\mu\nu} &= \partial_\mu A^a_\nu - \partial_\nu A^a_\mu - g\epsilon_{abc}A^b_\mu A^c_\nu \\ G_{\mu\nu} &= \partial_\mu B_\nu - \partial_\nu B_\mu \end{aligned} \tag{1.18}$$

The whole Lagrangian density can be written as :

$$\mathcal{L}_{tot} = \mathcal{L}(\psi, \nabla_\mu \psi) - \frac{1}{4}F^a_{\mu\nu}(F^a)^{\mu\nu} - \frac{1}{4}G_{\mu\nu}G^{\mu\nu} \tag{1.19}$$

Let us remarks that, for a free boson (spin 0 complex fields), the Lagrangian density is :

$$\mathcal{L}_{free} = (\partial_\mu \varphi^+)(\partial^\mu \varphi) - m^2\varphi^+\varphi \tag{1.20}$$

Considering then that the development of $\mathcal{L}_{tot}$ does not contain any quadratic terms in the gauge fields A^a_μ and B_μ, we are led to conclude that the gauge bosons associated to these gauge fields are massless. This is incompatible with the short range character of the weak interaction : the gauge bosons have to be heavy.

In the next section, we will see how by 'Spontaneous Global Symmetry Breaking', the gauge bosons can acquire a mass.

1.3 The Higgs phenomenon

In the previous section, we have shown that because of its observed short range nature, the weak interaction has to be mediated by massive bosons. The gauge theory described above has then to be expanded in order to include massive gauge bosons. A method to deal with this problem was put forward by P.W. Higgs [4] and F. Englert and R. Brout [5] independently. This method, based on the 'Higgs Mechanism', is referred to as the 'Spontaneous Symmetry Breaking Mechanism'. It provides a mass to the weak force mediators (the so-called intermediate bosons : $W^\pm$ and Z^0) while the mediator of the electromagnetic force (the photon γ) remains massless. This has been made possible by the introduction of a scalar field : the Higgs field.

The Higgs mechanism considers a scalar isodoublet φ for which the gauge invariant Lagrangian density $\mathcal{L}_{Higgs}$ is given by :

$$\begin{aligned} \mathcal{L}_{Higgs} &= (D_\mu\varphi^+)(D^\mu\varphi) - \mu^2\varphi^+\varphi - \lambda(\varphi^+\varphi)^2 \\ &= (D_\mu\varphi^+)(D^\mu\varphi) - V(\varphi^+\varphi) \end{aligned} \tag{1.21}$$

where $V(\varphi^+\varphi)$ is a self-interacting potential and D_μ is defined as before.

φ is the scalar isodoublet :

$$\varphi = \begin{pmatrix} \varphi_1 \\ \varphi_2 \end{pmatrix} \tag{1.22}$$

φ_i are complex fields.
$\mathcal{L}_{Higgs}$ is invariant for the SU(2)×U(1) gauge group, the field φ transforming like the matter fields in presence. The parameter λ is chosen such that $\lambda > 0$ to ensure the corresponding Hamiltonian to be 'down-limited' for all the configurations of the field φ. Choosing :

$$\mu^2 < 0$$

the field φ can take a vacuum mean value different from 0. This produces a spontaneous symmetry breaking which leads to massive gauge bosons.

In the Minimal Weinberg-Salam model, the Higgs field has been chosen as :

$$\varphi(x) = \begin{pmatrix} 0 \\ \eta + \frac{\sigma(x)}{\sqrt{2}} \end{pmatrix} \tag{1.23}$$

($\eta = \sqrt{\frac{-\mu^2}{2\lambda}}$ is the vacuum mean value of the field φ at all space-time point).

In 1.21, the development of $(D_\mu \varphi^+)(D^\mu \varphi)$ shows terms which are of second order in the fields A^a_μ $(a = 1, 2, 3)$ associated to the SU(2) symmetry and B_μ fields associated to the U(1) symmetry. These terms are :

- terms in A^1_μ in one hand, and in A^2_μ in the other hand, whose coefficients $(\frac{1}{2}g^2\eta^2)$ are interpreted as being the mass squared associated to the corresponding gauge bosons (A^1 and A^2 from which the physical gauge bosons $W^\pm$ will be built).

- mixed terms in A^3_μ B_μ which have no direct physical interpretation. These terms can be eliminated from the theory by defining the two following orthogonal combinations :

$$\begin{aligned} Z_\mu &= A^3_\mu \cos\theta_w - B_\mu \sin\theta_w \\ A_\mu &= A^3_\mu \sin\theta_w + B_\mu \cos\theta_w \end{aligned} \tag{1.24}$$

with θ_w, the Weinberg-Salam angle or weak mixing angle, chosen such that mixed products of Z_μ A_μ disappear. This is achieved by putting :

$$\tan\theta_w = \frac{g'}{g} \tag{1.25}$$

Applying this substitution in the development of $\mathcal{L}_{Higgs}$, the following term is found :

$$\frac{1}{2}\left(\frac{g^2\eta^2}{2\cos^2\theta}\right) Z_\mu Z^\mu \tag{1.26}$$

whose coefficient is proportional to the mass squared of the Z^0 boson associated to the field Z_μ.

- The absence of terms in $A_\mu A^\mu$ leads to assign a massless boson to the field A_μ. This boson will be identified as being the photon γ.

The three resulting masses are then :

$$M_W^2 = \frac{g^2\eta^2}{2} \; for \; A_\mu^1 \; and \; A_\mu^2 \tag{1.27}$$

$$M_Z^2 = \frac{g^2\eta^2}{2\cos^2\theta_w} = \frac{M_W^2}{\cos^2\theta_w} \; for \; Z_\mu \tag{1.28}$$

$$M_A^2 = 0 \; for \; A_\mu \tag{1.29}$$

A term of second order in the field σ (to which the Higgs boson is associated))

shows up also in the development of the Lagrangian density $\mathcal{L}_{Higgs}$ 1.21 $(\frac{1}{2}(-2\mu^2)\sigma^2)$ which leads to the existence of a massive neutral scalar particle, the so-called Higgs boson H^0 with mass :

$$M_{H^0} = \sqrt{-2\mu^2} \tag{1.30}$$

Therefore, the mass of the Higgs boson is not predicted and must be determined experimentally.

The real gauge fields A_μ^1 and A_μ^2 can be replaced by the complex fields :

$$W_\mu^- = \frac{1}{\sqrt{2}}(A_\mu^1 + iA_\mu^2) \tag{1.31}$$

$$W_\mu^+ = \frac{1}{\sqrt{2}}(A_\mu^1 - iA_\mu^2) \tag{1.32}$$

- W_μ^- and W_μ^+ are identified as the fields corresponding to the charged intermediate bosons W^- and W^+.
- Z_μ is identified as the field corresponding to the neutral intermediate boson Z^0.
- A_μ is identified as the electromagnetic field associated with the photon.

Let us go back to the expression 1.24 and express the terms containing A_μ^3 and B_μ as functions of A_μ and Z_μ, we get :

$$gA_\mu\frac{\tau^3}{2}+\frac{g'}{2}B_\mu\mathbb{1}\!\!\mathrm{I}=g\sin\theta_w QA_\mu+\frac{g}{\cos\theta_w}(\frac{\tau^3}{2}-Q\sin^2\theta_w)Z_\mu \tag{1.33}$$

with $Q=\frac{\mathbb{1}\!\!\mathrm{I}+\tau^3}{2}$.

The coupling constant associated to the massless field A_μ (the electric charge e) is then identified to be :

$$e=g\sin\theta_w \tag{1.34}$$

1.4 The Standard Model

As explained in section 1.2.2, S. Weinberg and A. Salam have proposed a gauge theory to unify weak and electromagnetic interactions, which together with the QCD theory is called : the Standard Model. A concrete model for the weak and electromagnetic interactions of known leptons (e, ν_e, μ and ν_μ) and hadrons (quarks) based on the gauge group SU(2)×U(1) can now be developed taking into account the V-A type of the weak interaction coupling.

1.4.1 The lepton case

Let us introduce the chiral isospin generators of $SU(2)_L$ and $SU(2)_R$:

$$\begin{aligned}L^a&=\frac{1-\gamma_5}{2}\frac{\tau^a}{2}\\ R^a&=\frac{1+\gamma_5}{2}\frac{\tau^a}{2}\end{aligned} \tag{1.35}$$

($a=1,2,3$).

For massless particles, $\frac{1\pm\gamma_5}{2}$ are the projectors respectively on the states of positive and negative helicity. Therefore, L^a acts only on negative helicity states (≡ left-handed states), while R^a acts only on positive helicity states (≡ right-handed states).

The leptons are grouped in weak isospin multiplets. For simplicity, let us consider only two multiplets. The generalisation to three is straightforward.

$$E=\begin{pmatrix}\nu_e\\ e\end{pmatrix}\quad M=\begin{pmatrix}\nu_\mu\\ \mu\end{pmatrix} \tag{1.36}$$

We define the action of an infinitesimal $SU(2)_L$ transformation (δ_L) such that :

$$\begin{aligned} \delta_L E &= i\epsilon^a L^a E \\ \delta_L M &= i\epsilon^a L^a M \end{aligned} \tag{1.37}$$

(where a=(1,2,3))
This transformation corresponds, for massless particles, to an isospin rotation of the left-handed states, the right-handed states remaining unaffected.

We can then define the following left-handed doublets :

$$\begin{aligned} E_L &= \frac{1-\gamma_5}{2}\begin{pmatrix}\nu_e\\ e\end{pmatrix} = \begin{pmatrix}(\nu_e)_L\\ e_L\end{pmatrix} \\ M_L &= \frac{1-\gamma_5}{2}\begin{pmatrix}\nu_\mu\\ \mu\end{pmatrix} = \begin{pmatrix}(\nu_\mu)_L\\ \mu_L\end{pmatrix} \end{aligned} \tag{1.38}$$

such that :

$$\begin{aligned} \delta_L E &= \delta_L E_L \\ \delta_L M &= \delta_L M_L \end{aligned} \tag{1.39}$$

while the right-handed fields behave like weak isosinglets e_R, $(\nu_e)_R$, μ_R, $(\nu_\mu)_R$:

$$\delta_L e_R = \delta_L (\nu_e)_R = \delta_L \mu_R = \delta_L (\nu_\mu)_R = 0 \tag{1.40}$$

At this point, we have to specify the action of the U(1) transformations which are defined to satisfy the requirement that the electromagnetic field A_μ (see equation 1.24) couples to the lepton electric charge :

$$\delta\chi = i\frac{\epsilon}{2} Y\chi \tag{1.41}$$

where χ is defined as :

$$\chi = \begin{vmatrix} (\nu_e)_L \\ e_L \\ (\nu_\mu)_L \\ \mu_L \\ . \\ . \\ . \\ (\nu_e)_R \\ \mu_R \\ . \\ . \\ . \end{vmatrix} \tag{1.42}$$

Y being the so-called weak hypercharge which is a quantum number associated to each type of matter particles (L or R).

The coupling of the matter particles χ to the neutral gauge bosons A_μ and Z_μ are obtained from the development of the Lagrangian terms $(i\bar{\chi}D_\mu\gamma^\mu\chi)$:

$$\begin{aligned} \mathcal{L} = -\bar{\chi}\gamma^\mu(A_\mu g \sin\theta_w(L^3 + \frac{1}{2}Y) \\ + Z_\mu \frac{g}{\cos\theta_w}(L^3 - \sin^2\theta_w(L^3 + \frac{1}{2}Y))\chi \end{aligned} \tag{1.43}$$

From the coupling of the electromagnetic field A_μ to the field χ, the following condition have to be satisfied :

$$Q = L^3 + \frac{1}{2}Y \tag{1.44}$$

which determines for each type of matter particle the weak hypercharge Y, once the electric charge Q and the third component of the weak isospin L^3 are known.

This condition leads to build table 1.3 which gives the weak isospin and the weak hypercharge for left-handed and right-handed leptons. Let us notice that, Q and L^3 being diagonal matrices, so is Y, and U(1) transformations act, in this case, as phase transformations.

	$(\nu_e)_L, (\nu_\mu)_L$	e_L, μ_L	$(\nu_e)_R, (\nu_\mu)_R$	e_R, μ_R
Q	0	-1	0	-1
$\mathbf{L^3}$	$+1/2$	$-1/2$	0	0
Y	-1	-1	0	-2

Table 1.3: Electric charge (Q), third component of the weak isospin (L^3) and weak hypercharge (Y) for the different weak isospin multiplets.

The coupling to the Z_μ field is made through a linear combination of the currents associated to the electric charge and the third component of the weak isospin ($L^3 - Q \sin^2 \theta_w$).

1.4.2 The quark case

A quark model, based on a similar method than the one used for leptons, can be built. The Cabibbo theory postulates that the weak interaction transforms a u quark into a state which is a linear combination of the strong eigenstates d and s :

$$\begin{pmatrix} u \\ d_c \end{pmatrix} = \begin{pmatrix} u \\ d\cos\theta_c + s\sin\theta_c \end{pmatrix} \tag{1.45}$$

where θ_c is the so-called Cabibbo angle, the mixing angle between the d and s quarks participating in the weak interaction.

The orthogonal doublet was introduced by Glashow, Iliopoulos and Maiani in 1970, containing a new quark (the c quark) :

$$\begin{pmatrix} c \\ s_c \end{pmatrix} = \begin{pmatrix} c \\ -d\sin\theta_c + s\cos\theta_c \end{pmatrix} \tag{1.46}$$

For these two generations of quarks, the Lagrangian density for the charged current (CC) part of the interaction can be written :

$$\begin{aligned} \mathcal{L}_{CC} = & -\frac{g}{2\sqrt{2}} W_\mu^+ \bar{u}\gamma_\mu(1-\gamma^5)(d\ \cos\theta_c + s\ \sin\theta_c) \\ & -\frac{g}{2\sqrt{2}} W_\mu^+ \bar{c}\gamma_\mu(1-\gamma^5)(s\ \cos\theta_c - d\ \sin\theta_c) \ +\ h.c. \end{aligned} \tag{1.47}$$

Like in the lepton model, $\begin{pmatrix} u \\ d_c \end{pmatrix}_L$ and $\begin{pmatrix} c \\ s_c \end{pmatrix}_L$ are assumed to be weak isodou-

blets and u_R, d_R, c_R, s_R weak singlets. The Lagrangian density becomes :

$$\mathcal{L}_{CC} = -\frac{g}{\sqrt{2}} W_\mu^+ (\bar{u_L} \bar{c_L}) \gamma_\mu \begin{pmatrix} \cos\theta_c & \sin\theta_c \\ -\sin\theta_c & \cos\theta_c \end{pmatrix} \begin{pmatrix} d_L \\ s_L \end{pmatrix} + h.c. \tag{1.48}$$

The formalism has been extended by Kobayashi and Maskawa (1973) to take into account the existence of two additional quarks by replacing the 2×2 Cabbibo matrix by the so-called Kobayashi-Maskawa 3×3 matrix. The additional quarks are the t quark and the b quark. For three generations the charged current (CC) part of the Lagrangian density is :

$$\mathcal{L}_{CC} = -\frac{g}{\sqrt{2}} W_\mu^+ (\bar{u_L} \bar{c_L} \bar{t_L}) \gamma_\mu \begin{pmatrix} V_{ud} & V_{us} & V_{ub} \\ V_{cd} & V_{cs} & V_{cb} \\ V_{td} & V_{ts} & V_{tb} \end{pmatrix} \begin{pmatrix} d_L \\ s_L \\ b_L \end{pmatrix} + h.c. \tag{1.49}$$

The matrix V is called the Kobayashi-Maskawa matrix. The elements can be expressed in terms of four parameters : three mixing angles θ_i (i = 1,2,3) and one phase δ.

1.4.3 Quark coupling to the Z^0

Let us consider all the Lagrangian density terms which contain the interaction between quarks and the Z^0 boson. Putting them together, we obtain the following condensed form :

$$\frac{g}{\cos\theta_w} Z_\mu (\bar{\chi} \gamma^\mu L^3 \chi - \sin^2\theta_w \bar{\chi} \gamma^\mu Q \chi) \tag{1.50}$$

with χ a column vector containing all the quark fields :

$$\chi = \begin{vmatrix} u_L \\ (d_c)_L \\ c_L \\ (s_c)_L \\ t_L \\ (b_c)_L \\ u_R \\ (d_c)_R \\ c_R \\ (s_c)_R \\ t_R \\ (b_c)_R \end{vmatrix} \tag{1.51}$$

L^3 and Q are diagonal matrices giving the eigenvalues corresponding to the different elements of χ. These values are summarised in table 1.4.

	u_L, c_L, t_L	$(d_c)_L, (s_c)_L, (b_c)_L$	u_R, c_R, t_R	$(d_c)_R, (s_c)_R, (b_c)_R$
Q	$\frac{2}{3}$	$-1/3$	$2/3$	$-1/3$
$\mathbf{L^3}$	$1/2$	$-1/2$	0	0
Y	$1/3$	$1/3$	$4/3$	$-2/3$

Table 1.4: The electric charge (Q), the third component of the weak isospin (L^3) and the weak hypercharge (Y) for the different weak isospin multiplets (quark case).

Let us analyse each term of 1.50 :

- The first term : $\bar{\chi}\gamma^\mu L^3 \chi$ can be developed as :

$$\begin{aligned} =&\frac{1}{2}\{\bar{u}_L\gamma^\mu u_L + \bar{c}_L\gamma^\mu c_L + \bar{t}_L\gamma^\mu t_L \\ &- (\bar{d}_c)_L\gamma^\mu(d_c)_L - (\bar{s}_c)_L\gamma^\mu(s_c)_L - (\bar{b}_c)_L\gamma^\mu(b_c)_L\} \end{aligned} \tag{1.52}$$

  We notice that quarks couple to the Z^0 without any modification of their flavour.

- The second term : $-\sin^2\theta_w \bar{\chi}\gamma^\mu Q\chi$ gives :

$$\begin{aligned} \sin^2\theta_w\{&\frac{1}{3}(2\bar{u}\gamma^\mu u + 2\bar{c}\gamma^\mu c + 2\bar{t}\gamma^\mu t \\ &- \bar{d}_c\gamma^\mu d_c - \bar{s}_c\gamma^\mu s_c - \bar{b}_c\gamma^\mu b_c\} \end{aligned} \tag{1.53}$$

  taking into account that $q_L + q_R \equiv q$, q standing for each quark type.

If we note the elements of χ : χ_L and χ_R, such that :

$$\chi_L = \frac{1}{2}(1-\gamma^5)\chi$$

$$\chi_R = \frac{1}{2}(1+\gamma^5)\chi$$

the terms 1.50 become :

$$\begin{aligned}&\frac{g}{\cos\theta_w} Z_\mu \{\bar{\chi}_L \gamma^\mu L_L^3 \chi_L - \sin^2\theta_w \bar{\chi}_L \gamma^\mu Q \chi_L \\ &- \sin^2\theta_w \bar{\chi}_R \gamma^\mu Q \chi_R\}\end{aligned} \tag{1.54}$$

$$\begin{aligned}&= \frac{g}{\cos\theta_w} Z_\mu \{\bar{\chi}\gamma^\mu \left(\frac{1-\gamma^5}{2}\right) L_L^3 \chi - \sin^2\theta_w \bar{\chi}\gamma^\mu \left(\frac{1-\gamma^5}{2}\right) Q\chi \\ &- \sin^2\theta_w \bar{\chi}\gamma^\mu \left(\frac{1+\gamma^5}{2}\right) Q\chi\}\end{aligned}$$

$$\begin{aligned}&= \frac{g}{\cos\theta_w} Z_\mu \{\bar{\chi}\gamma^\mu (L_L^3 - \sin^2\theta_w Q) \left(\frac{1-\gamma^5}{2}\right) \chi\} \\ &+ \{\bar{\chi}\gamma^\mu (-\sin^2\theta_w Q) \left(\frac{1+\gamma^5}{2}\right) \chi\}\end{aligned} \tag{1.55}$$

$$= \frac{g}{2\cos\theta_w} Z_\mu \{\bar{\chi}\gamma^\mu [(L_L^3 - 2Q\sin^2\theta_w) - \gamma^5 L_L^3]\chi\}$$

It is often convenient to write 1.55 in terms of the so-called vector and axial vector couplings, v_f and a_f , defined respectively as :

$$v_f = L_L^3 - 2Q\sin^2\theta_w$$
$$a_f = L_L^3$$

where the f index stands for each fermion type.

The expression 1.55 becomes :

$$= \frac{g}{2\cos\theta_w} Z_\mu \{\bar{\chi}\gamma^\mu (v_f - \gamma^5 a_f)\chi\} \tag{1.56}$$

In addition to the vector and axial vector couplings, it is useful to define couplings for left and right handed spinors by :

$$(v_f - a_f\gamma^5) = c_R \frac{1}{2}(1+\gamma^5) + c_L \frac{1}{2}(1-\gamma^5) \tag{1.57}$$

giving :

$$c_R = v_f - a_f = -2Q\sin^2\theta_w \tag{1.58}$$
$$c_L = v_f + a_f = 2(L_L^3 - Q\sin^2\theta_w) \tag{1.59}$$

1.4.4 The fermion masses

The fermions (leptons and quarks) are introduced in the theory with a zero mass in order to ensure the invariance of the Lagrangian density under the $SU(2)_L$ symmetry group for chiral isospin transformations. To obtain a non vanishing mass for fermions, we have to postulate that they can interact differently than only through the weak and the electromagnetic interactions : non vanishing masses for the fermions can be generated by the coupling of the Higgs field to the fermions.

Yukawa type interaction terms are introduced into the Lagrangian density. they can be symbolically written as :

$$\mathcal{L}_{\varphi-f_i} = \sum_i g_{si}\varphi\bar{\psi}_i\psi_i \tag{1.60}$$

where i stands for all fermion types (leptons or quarks) and g_{si} is a coupling constant which has to be adjusted in order to get the corresponding fermion mass.

With the Higgs field as written in equation 1.23, one obtains :

$$\mathcal{L}_{\varphi-f_i} = g_{si}\eta\bar{\psi}_i\psi_i + g_{si}\frac{\sigma}{\sqrt{2}}\bar{\psi}_i\psi_i \tag{1.61}$$

The first term is the mass term of the corresponding fermion i which would then be equal to $(g_{si}\eta)$ with η still an arbitrary parameter constraint by the (still unknown) mass of the Higgs boson. The second terms describe a residual, Yukawa type interaction between the Higgs field and the fermion fields. This interaction has to be added to the electroweak interaction framework. This new interaction is characterized by the coupling constant g_{si} and should be sufficiently small so as not to destroy the good agreement (at the present level of accuracy) between the V-A theory and experiment.

From equation 1.61 we deduce the mass of the fermion i :

$$m_{f_i} = g_{si}\eta \tag{1.62}$$

But we have written (see equation 1.27) :

$$M_W = \frac{g\eta}{\sqrt{2}} \tag{1.63}$$

where g is the coupling constant associated to the gauge fields.

Combining 1.62 and 1.63, we can write :

$$g_{si} \approx \frac{m_{f_i}}{\eta} = \sqrt{2} g \frac{m_{f_i}}{M_W} \tag{1.64}$$

and therefore :

$$g_{si} \ll g \tag{1.65}$$

Moreover, the fermion-fermion interaction amplitude through the exchange of a Higgs boson H at low energy is given by :

$$\begin{aligned} A \approx g_{si}^2 \frac{1}{M_H^2} &\approx \frac{g^2}{M_W^2} (\frac{m_{f_i}}{M_H})^2 \\ &\approx G_F \frac{m_{f_i}^2}{M_H^2} \end{aligned} \tag{1.66}$$

where :

$$G_F \approx \frac{\sqrt{2} g^2}{8 M_W^2} \tag{1.67}$$

is the Fermi coupling constant.

Consequently, if the neutral Higgs boson mass (M_H) is greater than the fermion mass ($M_H \gg m_{f,i}^2$ with $M_H = \sqrt{-2\mu^2}$), the coupling terms 1.60 have a negligible action in the weak interaction theory. They are, anyway, theoretically indispensable to generate non vanishing fermion masses.

1.5 Conclusion

In this section we have shown the significance of the various parameters that the Standard Model of the electroweak interactions contains. These are the coupling constants of the SU(2) and U(1) groups g and g' (or, alternatively, e and $\sin^2 \theta_w$), the mass of the Higgs boson m_H and the constant η related to the vacuum expectation value of the Higgs field. The fermion masses are also parameters. Hence the introduction of a fundamental scalar solves the mass generation problem, but only at the expense of introducing arbitrary parameters.

The agreement between the theory (the Standard Model) expectations and the experimental results obtained by the four LEP experiments is very good (within 1%). Still the Higgs boson mass remains unknown : the present lower limit (at 95 % confidence level) from the combined results of the four LEP experiments is 65.2 GeV/c^2 [6]. Higgs boson search at LEP200 should extend the search range up to 90 GeV/c^2. The future LHC project will be designed to find the Standard Model Higgs boson in the whole possible mass range up to 1 TeV/c^2 [7].

Bibliography

[1] G. Maiani, in Proceedings of the 1976 CERN School of Physics, p. 28. (1976).

[2] Arnison G. et al., *Phys. Lett.* **B112** (1983) 103;
Arnison G. et al., *Phys. Lett.* **B126** (1983) 398;
Banner G. et al., *Phys. Lett.* **B122** (1983) 476;
Banner G. et al., *Phys. Lett.* **B129** (1983) 130.

[3] S. L. Glashow, *Nucl. Phys.* **B22** (1961);
S. Weinberg, *Phys. Rev. Lett.* **19** (1967) 1264;
A. Salam, *Proc. of the 8th Nobel Symposium*, Ed. N Svartholm, Almqvist and Wiksell, Stockholm, (1968) 367.

[4] P.W. Higgs, *Phys. Lett.* **12** (1961) 132;
Phys. Rev. Lett. **13** (1964) 508;
Phys. Rev. **145** (1966) 1156.

[5] R. Brout and F. Englert, *Phys. Rev. Lett.* **13** (1964) 321.

[6] J.-F. Grivaz, *Proc. of the International Europhysics Conference on High Energy Physics*, Brussels (1995) 827.

[7] C.W. Fabjan, CERN-PPE/95-25 (1995);
D. Denegri, CERN-PPE/95-183.

Chapter 2

The experimental setup

2.1 The LEP collider

In their concern to confirm the validity of the present theory of the electroweak and strong interactions, known as the "Standard Model", the physicists decided at the beginning of the eighties to build the **L**arge **E**lectron-**P**ositron collider, LEP [1]. It was optimised to operate at centre of mass energies peaked at the Z^0 mass (91 GeV/c^2) to study Z^0 decay properties (LEP 100). In a second phase starting in 1996, LEP is operated at energies up to $\sqrt{s} = 200$ GeV to study essentially $W^{\pm}$ physics (LEP 200).

This biggest particle accelerator ever constructed -the **L**arge **E**lectron **P**ositron (LEP) collider- was built on the franco-suisse border near Geneva at CERN.

The technical installations of LEP accelerator-collider complex are housed in a ring-shaped tunnel, 27 kilometres long, 3.8 metres wide and located between 50 and 70 metres below the surface (figure 2.1). The ring is not a perfect circle but consists of eight 2800 metres curved sections or arcs linked by eight straight sections. In the arcs, the electrons and positrons are kept on a circular orbit by 3392 bending magnets. The beams are focused by 816 quadrupole and 504 sextupole magnets all positioned along the straight sections and the arcs of the ring. Prior to each collision, the electrons and the positrons are accelerated as they pass through radiofrequency accelerating cavities. The collisions of the beams take place at the centre of straight sections.
Before the electrons and positrons enter LEP, full use is made of pre-LEP injectors and accelerators (figure 2.2). This injection system has to feed some five million million electrons and positrons into the main LEP ring about

once every twelve minutes. The electrons are obtained via thermionic emission from a heated filament and subsequent electric field extraction whence they are accelerated to 200 MeV in the **L**EP **I**njector **L**inac (LIL). Some of these electrons are accelerated up to 600 MeV in the second stage of the LIL, after which they enter the **E**lectron **P**ositron **A**ccumulating ring (EPA).
The rest of the 200 MeV electrons are used to obtain the positrons : they are decelerated by a fixed target, producing bremsstrahlung photons which then produce pairs of electrons and positrons. The positrons are separated out by magnetic field extraction, accelerated to 600 MeV and passed to the EPA to join the electrons.
When sufficient positrons are stored, the electrons and the positrons pass separately into the **P**roton **S**ynchrotron (PS) for further acceleration to 3.5 GeV, then into the **S**uper **P**roton **S**ynchrotron (SPS) to be accelerated to 22 GeV. Finally, bunches of electrons and positrons are transferred into the LEP ring in opposite direction.

For the first construction phase, four large experimental halls have been equipped with detectors. The first four experiments on LEP were selected on the basis of their physics potentiality and technical feasibility.

ALEPH, DELPHI, L3 and OPAL[1] are 4 magnetic detectors designed to detect and measure all final state particles produced in e^+e^- collisions. Although the aim of the four experiments is an optimal detection of all the particles created in the collisions between electrons and positrons, they have specific aims and are therefore characterised by particular and complementary technological features. Their most striking properties are mentioned here.

The idea behind ALEPH was to build a general purpose detector, able to cope with all the physics at LEP but with a minimum of components. In a way, it is the simplest of the four detectors, using the smallest number of detector systems to measure and identify charged and neutral particles, with the accent on lepton identification. It has a very powerful Time Projection Chamber (TPC) in a high magnetic field of 1.0 Tesla (for tracking and accurate determination of the momenta of all produced charged particles) surrounded by a fine grain electromagnetic calorimeter (for identifying electrons and measuring energy deposition with very good spatial resolution).

[1]ALEPH stands for "Apparatus for LEP physics"
DELPHI stands for "Detector with Lepton Photon and Hadron Identification"
L3 so named because it was the third Letter of intend
OPAL stands for "Omni Purpose Apparatus for LEP"

The momentum resolution in combination with a micro-vertex detector is 0.12 p_t %[2].

The analysis presented in this thesis is based on the data recorded by DELPHI (Detector with Lepton, Photon and Hadron Identification). DELPHI is described in details in section 2.2. Essentially it is able to measure all the physical characteristics of the leptons and photons and to identify the hadrons produced in the LEP collisions. It can then study in depth the details of the production and the decay of the Z^0 particles that LEP provides in quantity. DELPHI major elements include the biggest superconducting coil ever constructed. Outside the coil are the hadron calorimeter and muon tracker. The particularity of DELPHI comes from its Ring Imaging Cherenkov counters (RICH) (see chapter 3) using the Cherenkov effect in a novel way to identify hadrons.

L3 stands out from the other experiments in its physics aims : it is the largest of the four LEP detectors and provides accurate tracking and high precision in lepton and photon momenta measurement. An energy resolution of $1.2\%/\sqrt{E(GeV/c)}$ can be achieved. Notable features of the detector are the enormous size of magnet (radius = 6.8 m) -its coil (field of 0.5 T) is near the perimeter of the detector and encloses all the experiment concentric detection systems- and the muon detectors designed to have optimum momentum resolution as well as the use of a calorimeter for electromagnetic shower detection and energy measurement.

OPAL uses detector techniques such as drift chambers for its central detector (measurement of the position of the charged particles), lead-glass blocks for electromagnetic detectors (identification of the electrons and photons and measurement of their energy), and streamer tubes (detection of hadron showers). A muon detector which completely surrounds OPAL comprises 10 metres long drift chambers to pick up and locate the penetrating muons produced in the electron-positron interactions. The coil of the magnet (field of 0.4 T) is in the annular space between the central detector (drift jet chamber) and the lead-glass calorimeter (electromagnetic shower counter) in contradistinction with ALEPH where the TPC and the electromagnetic detector lie inside the magnetic field.

The LEP collider tunnel including the experimental halls has been con-

[2] p_t is the transverse momentum expressed in GeV/c.

structed over a period of four years. Installation of the experiments was started at the end of 1987. The first particle beams were circulating in the LEP machine in June 1989. In August 1989 a first pilot run for physics was performed.

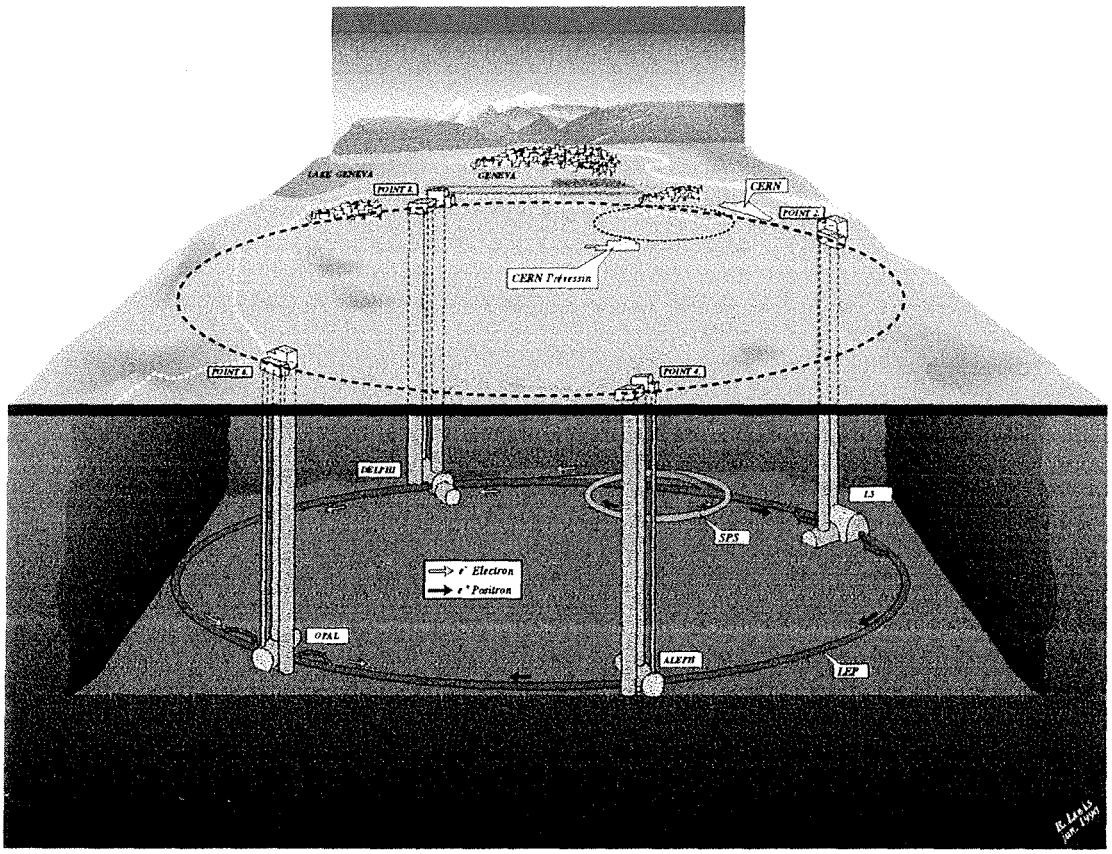

Figure 2.1: Cross-section of the LEP installation with the Alps in the background, the Geneva plain in the middle and the LEP underground experimental areas in the foreground.

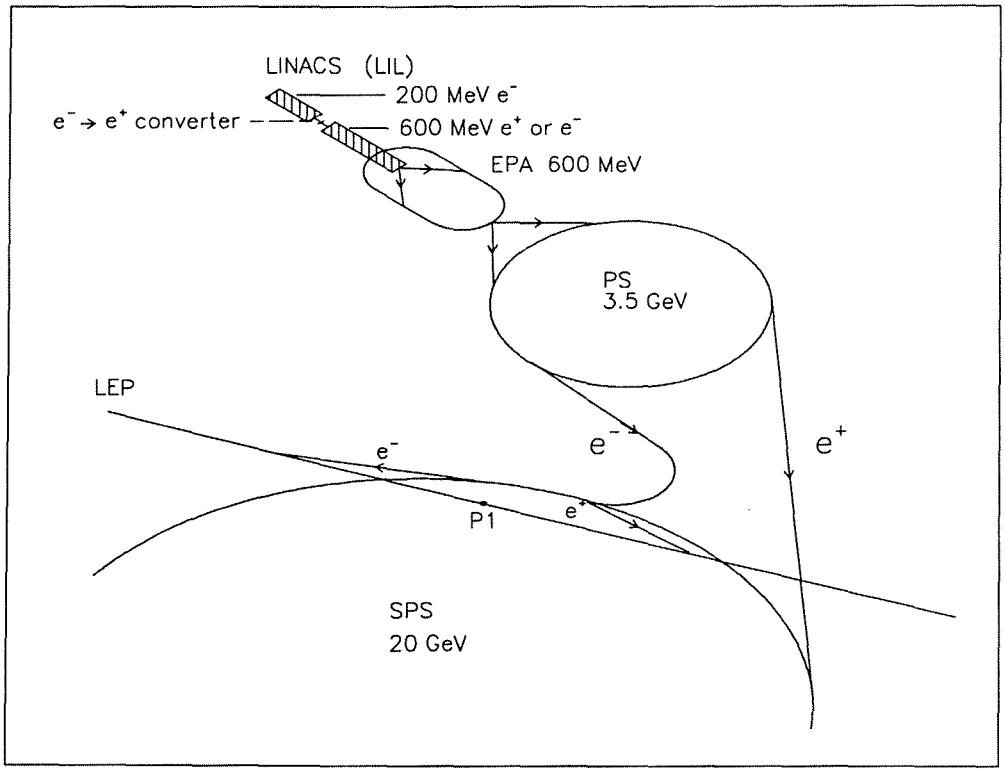

Figure 2.2: The LEP injection system.

2.1.1 The luminosity

Several parameters influence the quality of the physics results obtained with the LEP data. One of them is the rate at which particles collide. This rate is proportional to the luminosity L, given by :

$$L = \frac{n_e n_p k f}{4\pi\sigma_x\sigma_y} cm^{-2}s^{-1} \tag{2.1}$$

where n_e, n_p are the numbers of electrons or positrons in a bunch (4.10^{11} particles), k is the number of bunches in the LEP ring (i.e. $k = 4$ and then 8), f is the revolution frequency and σ_x and σ_y the horizontal and vertical r.m.s beam spread at the collision point. In order to optimise the luminosity in LEP (nominal value of $L \simeq 10^{31} cm^{-2}s^{-1}$), the values of σ_x and σ_y

have to be reduced as much as possible. This is achieved by tightly squeezing the bunches of each bunch to small dimensions at the interaction region at the centre of the particle detectors. This is the role of superconducting quadrupoles positioned at either side of each detector : they focus the beams in the interaction point to a size of 300 μm in the x direction and 12 μm in the y direction.
In section 3.2.8 we will see how the luminosity is obtained with a better approximation than calculating the parameters appearing in equation 2.1, using a reference process of which the cross-section is theoretically well defined and does not depend on the parameters to be measured.
The event production rate is then given by :

$$N = L\,\sigma\,t$$

with σ the cross-section of the interaction of interest (here $e^+e^- \rightarrow Z^0 \rightarrow$ charged particles) and t the data taking time.
The integrated luminosity L_{int} defined as :

$$L_{int} = \int_0^t L\,dt$$

is a frequently used variable. The product of L_{int} and the cross-section (which is, at peak, about 40 nb[2] for Z^0 production) yields the total number of events produced during the time interval t. Figure 2.3 shows the time-evolution of L_{int} delivered by LEP between 1993 and 1996. For 1994, about 1.484.000 Z^0 decays were collected by the DELPHI detector.

[2] 1 barn= 10^{-24} cm^2

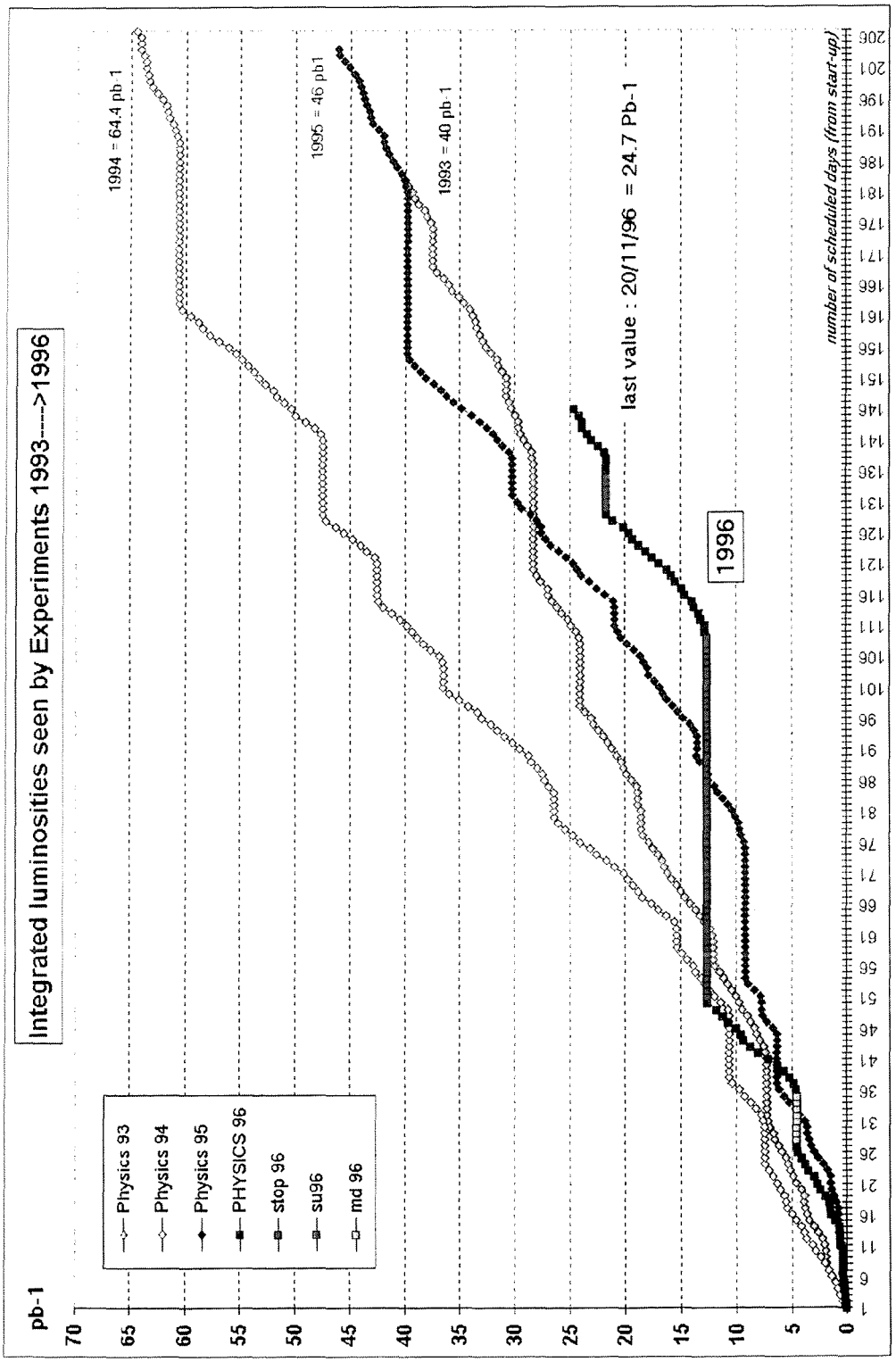

Figure 2.3: Integrated luminosity seen by LEP experiments from 1993 to 1996.

2.2 The DELPHI detector

2.2.1 Introduction

The most complex of the four LEP detectors is DELPHI [3], a **DE**tector with **L**epton, **P**hoton and **H**adron **I**dentification.

DELPHI has the conventional layout of an e^+e^- detector intercepted with more recent detection techniques. It combines a good 3-dimensional track localisation (see section 2.2.3) and a reasonable energy resolution with an powerful identification of leptons, photons and hadrons. In addition to the standard particle identification by dE/dx measurement, DELPHI is equipped with ring imaging Cherenkov detectors, its main distinction from the other LEP experiments.

Each of the various sub-detectors were constructed and are currently operated by over 500 physicists. These sub-detectors are accurately aligned within three detector elements.The main element is a 5 m radius, 10 m long cylinder, termed the barrel. The other two elements are located at each end of the barrel, and as such are named endcaps. The separate elements are fully mobile to enable easy access to the sub-detectors when LEP is not running. Altogether, DELPHI covers a solid angle as close as possible to 4 π steradians around the interaction point.

Figure 2.4 gives a cut-out view of the DELPHI detector showing its 21 subcomponents.

The cartesian reference system of DELPHI is a right-handed system with its origin at the interaction point, the x-axis pointing towards the centre of LEP, the y-axis pointing upwards and the z-axis being defined by the direction of the e^- beam. Figure 2.5 shows this coordinate system. θ and ϕ are respectively the polar and azimuthal angles. The barrel region having a revolution symmetry with its axis parallel to the e^+e^- beams, the location of a point in the barrel is defined in the cylindrical system (r, $r\phi$, z). The radial coordinate r is defined as $r = \sqrt{x^2 + y^2}$ and the coordinate $r\phi$ is the product of the radius r and the angle ϕ. $r\phi$ is thus the distance measured along the circular arc of radius r in the (x, y) plane. The choice of this coordinate $r\phi$ is aimed to improve the subdetector spatial resolution (depending on r and ϕ).

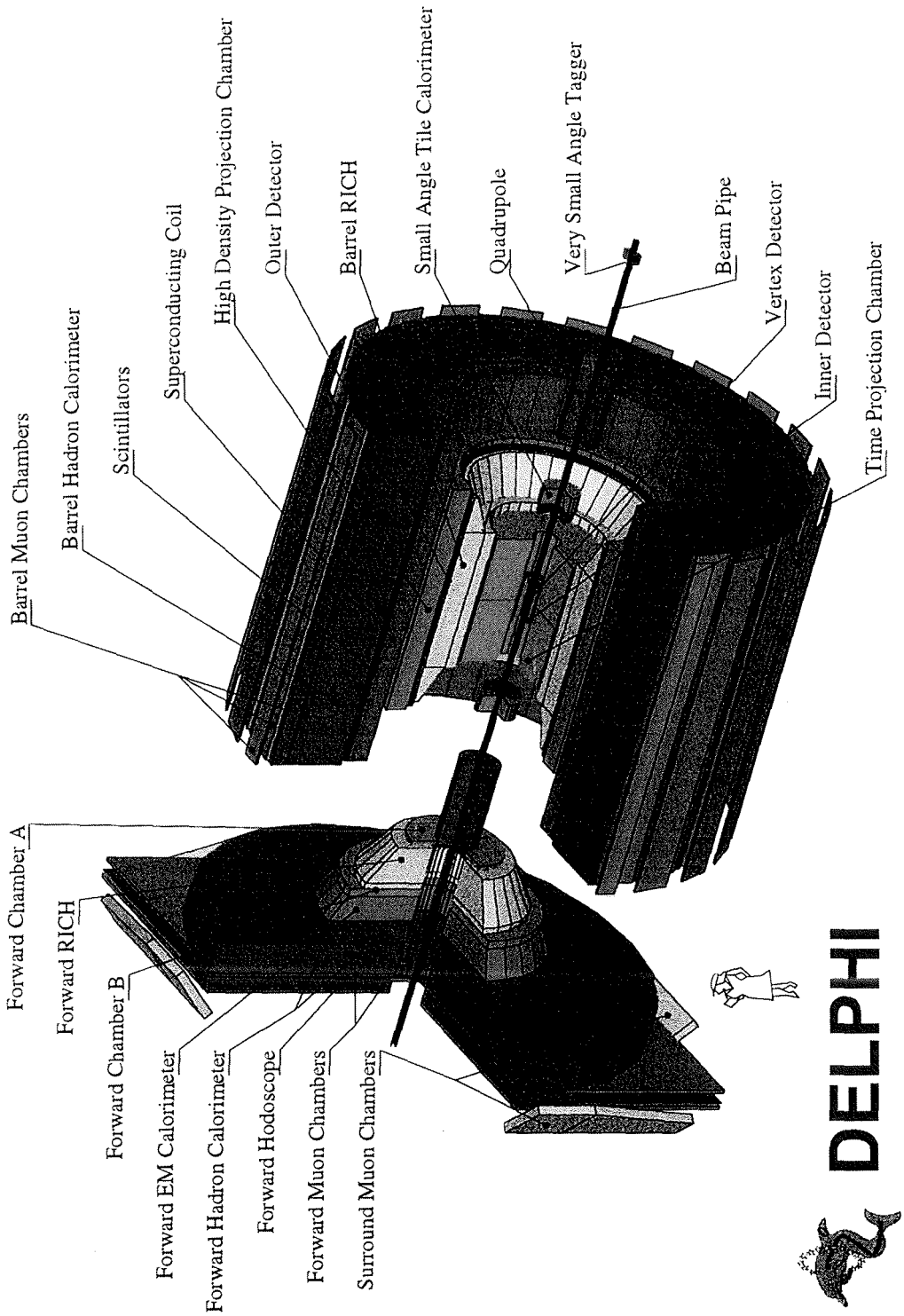

Figure 2.4: A cut-out view of the DELPHI detector.

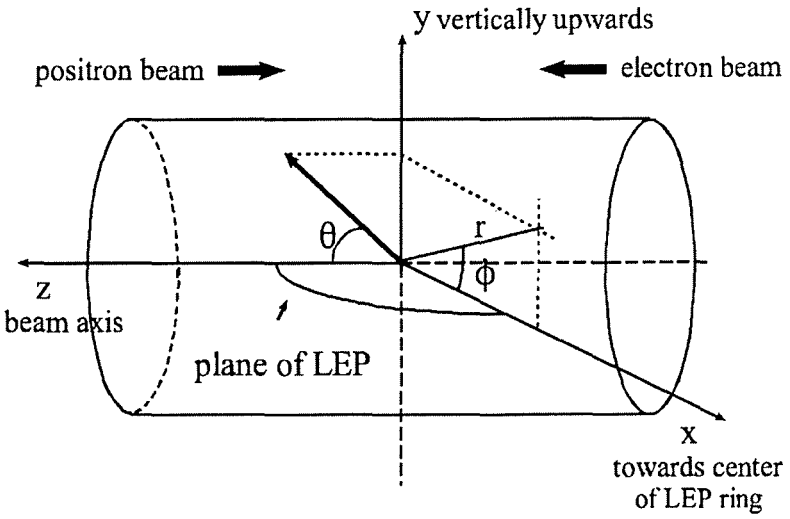

Figure 2.5: The reference system of the DELPHI detector.

DELPHI is operated since 1989. The subdetectors present in DELPHI in 1990 are described in detail in reference [2]. The aim of the following sections is to summarise developments since then and to review the performances achieved. A more complete description of the DELPHI detector together with a full review of its performances can be found in reference [3].

2.2.2 The solenoid

DELPHI operates in a magnetic field of 1.23 Tesla produced by a superconducting solenoid enabling high resolution momentum determination. The purpose of the solenoid is to provide DELPHI with a homogeneous longitudinal magnetic field parallel to the beam axis. As such, the paths of the incoming electrons and positrons at $\theta = 0°$ are unaffected. Charged particle final states traversing the field away from this value of θ are forced into helical motion with radius depending on the particle momentum and the direction of curvature depending on its charge. The curvature reconstructed from the information of the tracking detectors allows particle momentum and charge to be measured. In general, a track with a radius of curvature r, in a magnetic field B, has a value of transverse momentum p_t given by : $p_t = 0.3\ B\ r$, with p_t in GeV/c, B in Tesla and r in metres.

The superconducting solenoid is 7.5 m long and has a 5.2 m inner diameter. The 1.23 T field is made uniform in the tracking chambers of the barrel (so as not to disturb the electron drift), by two sets of compensation coil. At a radius of approximately 4 m, 20 layers of 5 cm thick iron, in the barrel and in the endcaps, form the magnet yoke for the containment of the solenoidal field.

2.2.3 The DELPHI tracking detectors

The utility of the tracking chambers is to reconstruct charged particle tracks and to measure their momenta.
The tracking system of DELPHI is segmented into a relatively large number of independent tracking devices. In the barrel region, four tracking detectors are installed : the micro Vertex Detector (VD) which provides tracking information for short lived particles from Z^0 decays, the Inner Detector (ID), the Time Projection Chamber (TPC) which provides from four to sixteen point measurements of a charged particle trajectory and finally, the Outer Detector (OD).
In the endcaps, at very low angles, Forward Chambers A and B (FCA and FCB) are combined to enable tracking in this region. The following sections outline these detectors individually, the last one gives an overview of their combined tracking ability.

◇ The barrel tracking chambers

The micro Vertex Detector At LEP energies, short lived particles (with a lifetime of the order of 10^{-13} to 10^{-12} s) from Z^0 decays such as taus and B hadrons, travel small distances (~few mm) before decaying. Such small distance decays, occurring within the beam pipe, can only be studied by placing a precise tracker as close as possible to the beam pipe. The detector, which covers an angular region from 44° to 136° , consists of three concentric shells, at radii of 6.3 cm, 9 cm and 11 cm. Each shell is segmented in ϕ in 24 modules with ~10% overlap to assist alignment. The closer and outer layers provide both $r\phi$ and z coordinates. The inner layer gives $r\phi$ points only. The strip width (which gives the space position of the ionization pulse) is 50 μm in the $r\phi$ direction whereas in z, the pitch varies between 50 and 150 μm. The $r\phi$ hit coordinate precision is better than 10 μm. The single hit precision of the z coordinate reaches a value of 9 μm.

The Inner Detector The purpose of the Inner Detector is threefold :

- to give good tracking at small radii for angles in the region 30° to 150° ;

- to provide trigger information in r and z with a granularity of about 1° ;
- to separate charged particles tracks in one jet with an accuracy of 1 mm in $r\phi$.

To fulfil these tasks, a detector consisting of two cylindrical position measuring chambers, was constructed.
The two concentric cylindrical chambers are :

- a drift jet chamber surrounded by a set of 5 coaxial multi-wire proportional chambers. The jet chamber (11.6 cm $\leq r \leq$ 23 cm) is a classical cylindrical drift chamber covering an angular region in between 17° and 163° and segmented in 24 ϕ modules. Up to 24 $r\phi$ positions, precise to 90 μm, are measured for a charged particle crossing a segment at uniform ϕ.

- the coaxial multi-wire proportional chambers (23 cm $\leq r \leq$ 28 cm) cover an angular region in θ between 30° and 150° . They provide up to 5 points, each with a precision $\sigma_z < 1$ mm. The short read-out time (t < 2.3 μs) of these proportional chambers enables the Inner Detector to be used in the first level trigger (see section 2.2.9).

The Time Projection chamber The TPC data are the starting point for track reconstruction in the θ angular region from 22° to 158° . In this region the TPC provides from four to sixteen point measurements on a charged particle trajectory. It is used for particle momentum determination and particle identification which is based on the measurement of the particle energy loss (dE/dx).
The TPC consists in a cylindrical drift chamber with an inner radius of 35 cm, an outer radius of 111 cm and is 300 cm long. Compared to the ALEPH TPC (radius = 180 cm, length = 460 cm), the DELPHI TPC is small. This is because particle identification in DELPHI is complemented by the Ring Imaging Cherenkov detectors (RICHes, see chapter 3). The smaller TPC leaves space for the RICH detectors whilst still providing tracking information of a sufficiently high standard. The sensitive volume of the TPC is divided into two identical symmetric halves at $z = 0$ m, each half being further divided into six sectors azimuthally (in ϕ). These sectors are filled with a mixture of argon/methane (80%/20%), at atmospheric pressure.
Electrons formed by an ionizing particle traversing the sensitive gas volume drift under the influence of a uniform electric field, parallel to the z axis, to one of the endcaps. There, they are detected by anode wires and cathode pads. The total drift length on each side of the central plane is 134 cm. Laser tracks are used to monitor the drift velocity continuously during data taking. The drift velocity is about 7 cm/μs at the nominal voltage. The relative precision of the drift speed measurement is better than 2×10^{-4}. Points on the

ionizing track are spatially reconstructed by measuring their projected image in the $r\phi$ plane on the endcap ($r\phi$ accuracy = 250 μm per point), using the cathode pads and anode wires, and by measuring their z coordinate from the drift times (z accuracy = 900 μm per point).

On top of three-dimensional track reconstruction, the TPC helps in charged particle identification by measuring the ionization loss rate (dE/dx) of charged particles over their track length. The sense wires of its proportional chambers provide up to 192 ionization measurements per track.

The Outer Detector The OD is designed to enable charged particle track position measurements with a good spatial resolution at 2-metre distance from the interaction point. The lever arm for track reconstruction is then increased and the momentum resolution for fast charged particles greatly improved. This is of crucial importance for the exploitation of the RICHes as it is explained in chapter 3.
The fast readout time enables it to be used in conjunction with the Inner Detector in the first level trigger (see section 2.2.9) to gate the TPC.
The OD also enables easier association of energy depositions in the barrel electromagnetic calorimeter with tracks from the TPC.
The Outer Detector sits between the barrel RICH and the barrel electromagnetic calorimeter at a radius of 197 cm to 206 cm. In z it is 486 cm long. In ϕ it covers the angular region from 42° to 138° . In θ, it is segmented into 24 identical overlapping modules. Each module consists of 5 layers of drift tubes operated in streamer mode with a mixture of argon, isobutane and isopropanol. Full azimuthal coverage is offered due to layers being staggered and overlapping. Each layer provides $r\phi$ information with an accuracy better than 110 μm per track, and in addition, the central three layers provide fast z information ($\sigma(z) = 3.5$ cm).

◇ The endcap tracking chambers

These two classical drift chambers (FCA and FCB) are designed to enable tracking, pattern recognition and triggering down to low angles. Combined they cover θ from 33° down to 11°.

The Forward Chamber A The FCA is mounted on each end of the TPC. It consists of 2 discs perpendicular to the beam axis which cover the angular region in θ between 11° and 32° and 148° and 169° , respectively. Each disc is divided into 2 modules (one at $y < 0$ and the other at $y > 0$).

The four modules cover the following area :

$$\begin{aligned} 155\ cm &\leq |z| \leq 165\ cm \\ 29\ cm &\leq r \leq 103\ cm \end{aligned}$$

Each module is made of 3 chambers, each with two staggered planes of 64 drift tubes. Neighbouring chambers are rotated through 120° relative to each other in the (x, y) plane to remove ambiguities.
The measured drift times give six position coordinates which form a track element. In normal conditions, where the direction of the particle is not known a priori, the reconstructed track elements have precisions of $\sigma(x) = 290\ \mu m$, $\sigma(y) = 240\ \mu m$, $\sigma(\theta) = 8.5$ mrad and $\sigma(\phi)$ averaged over θ is 24 mrad.

The Forward Chamber B The FCB is located between the forward RICH and the forward electromagnetic calorimeter, mounted perpendicular to the beam axis in the regions :

$$\begin{aligned} 267\ cm &\leq |z| \leq 283\ cm \\ 53\ cm &\leq r \leq 195\ cm \end{aligned}$$

It consists of four modules placed at $x > 0$ and $x < 0$ and covering the angular region in θ between 11° and 36° and 144° and 169° , respectively. Each module is made of 12 sense wire planes separated by 1.1 cm and rotated in pairs through 120° with respect to the others.
The precisions achieved on the parameters of the reconstructed track elements are $\sigma(x, y) = 150\ \mu m$, $\sigma(\theta) = 3.5$ mrad and $\sigma(\phi) = 4.0\ /\ sin\theta$ mrad.

◇ Combined Tracking

As it is explained in chapter 3, RICH counters are not stand-alone detectors : they rely on the tracking detectors for the track position inside the RICH and the momentum measurement. Moreover, asking signals in the tracking devices surrounding the RICHes in both the barrel and the endcap regions ensures that only well reconstructed tracks crossing the RICHes are used in the measurement.

Tracking in the barrel begins with the TPC track segments for the track fit. This is combined with the OD track segment to ensure high momentum resolution and the ID information which ensures good point resolution near

the interaction region, and aids the association of tracks with hits in the Vertex Detector.
Charged particles produced at small angles see less of the TPC, and it is here that FCA and FCB assist in the tracking. Down to 20° however, nine of the 24 ID jet points and three of the 16 pads from the TPC are still available to give decent momentum resolution when combined with the forward chambers. Charged particles below this value have poorer momentum resolution.
The momentum accuracy of the tracking system is given on figure 2.6 which shows the inverse momentum distribution for muon pairs at 45.6 GeV/c for :
-(a) The barrel region combining the information of VD, ID, TPC and OD.
-(b) The endcap regions combining the information from VD and FCB, at least.
Overall, the track momentum resolution in the barrel region ($45° < \theta < 135°$), with 45.6 GeV/c muon pairs, is given by :

$$\sigma(1/p) = 0.57 \times 10^{-3}(GeV/c)^{-1}$$

For the endcap regions ($20° < \theta < 35°$ and $145° < \theta < 160°$), this resolution is roughly worse by a factor of 2 :

$$\sigma(1/p) = 1.31 \times 10^{-3}(GeV/c)^{-1}$$

At other momenta, the track parameter precisions can be estimated by comparing simulated and reconstructed parameters in a sample of generated Z^0 hadronic events. Figure 2.7 shows σ_p/p, σ_θ and σ_ϕ as a function of the polar angle θ and the momentum p of the track. We can see that, for a given momentum, the precision (σ) remains constant over the barrel region but deteriorates in the forward regions of DELPHI.

2.2.4 The muon identification chambers

The muon chambers are designed to identify muons by recording at least two spatial points on a track that has crossed most of the iron of the hadron calorimeter. This iron acts as a filter which gives a first level of separation between muons and hadrons. Most hadrons are stopped by this material, whereas all muons of momenta above 2 GeV/c are expected to penetrate the MUon Chambers (MUC=MUB+MUF+MUS). They are simple drift chambers positioned in, and on the outside of, the iron yoke.
Until 1993 the muon detection system was divided into two parts : the Barrel MUon chambers (MUB) and the Forward MUon chambers (MUF). It did not offer full coverage : the low angle region ($\theta < 15°$) and the regions $45° <$

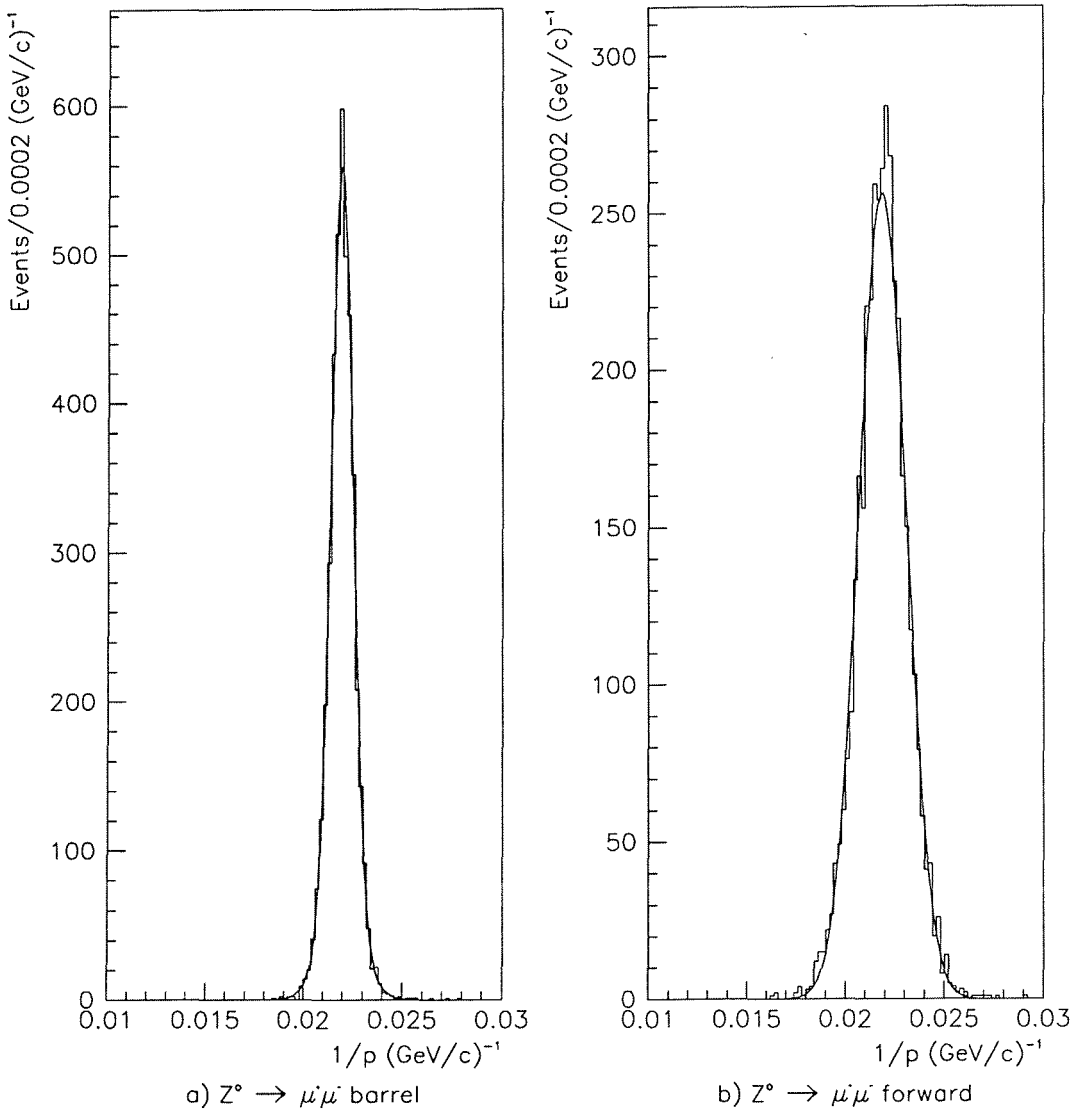

Figure 2.6: Inverse momentum distribution for collinear muons from $Z^0 \rightarrow \mu^+\mu^-$ decays : (a) tracks containing hits from VD, ID, TPC and OD, (b) tracks containing hits from VD and FCB at least.

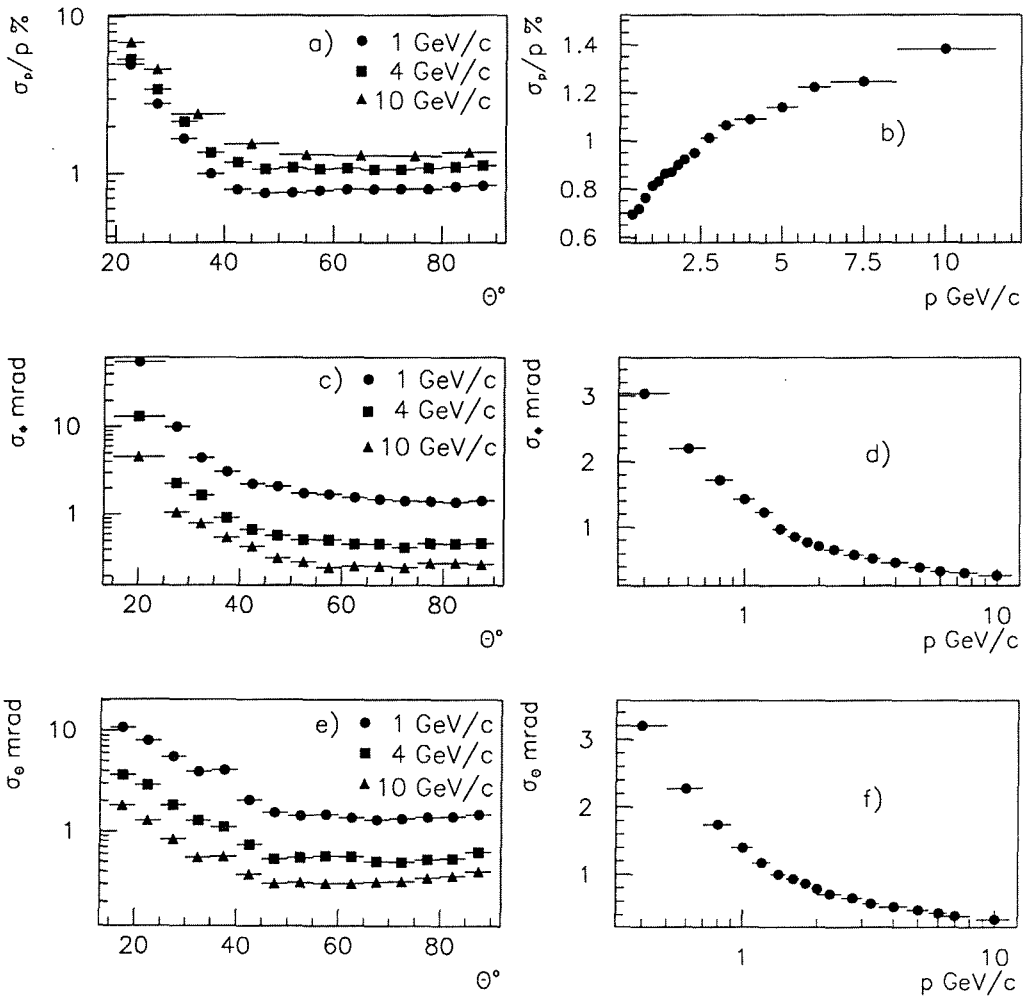

Figure 2.7: Track parameter precisions : (a) momentum precision as a function of the polar angle θ, (b) momentum precision as a function the momentum for barrel tracks, (c) azimuthal angle precision as a function of θ, (d) azimuthal angle precision as a function of the momentum for barrel tracks, (e) polar angle precision as a function of θ, (f) polar angle precision as a function of the momentum for barrel tracks.

$\theta < 53°$ and $127° < \theta < 135°$ were not covered. In order to cover these two $8°$ holes in θ, it was then decided to install a new set of muon chambers, the Surround MUon chambers (MUS, also called SMC).

The Barrel MUon chambers

The MUB consist of three layers of 4 m long drift chambers covering an angular region in θ between $53°$ and $127°$ and segmented in ϕ into 24 modules covering $15°$ each in azimuth. Each sector is made of two detection modules : one at $z < 0$ and one at $z > 0$.
The first layer to be crossed by a muon is called the inner layer, which is 104 cm wide and positioned 90 cm inside the iron yoke. This inner layer is made up of three staggered layers (to solve the left-right ambiguity) of drift tubes, two layers of which are used as read-out, the third one as a spare.
The drift tubes, which measure 20.8 cm by 2.6 cm, contain a single anode wire and as such have a maximum drift distance of $\sim$10 cm. They are operated in proportional mode with a gas mixture of argon (85.5%), carbon dioxide (6%) and isobutane (8.5%). The measured drift time gives the $r\phi$ information. z information is obtained by timing the signal delay on the anode. The resolution obtained on extrapolated tracks is $\sim$ 2 mm in $r\phi$ and $\sim$ 80 mm in z.
The next two layers are called the outer and the peripheral ; each is 8.3 cm wide and consists of two layers of drift tubes. The outer layer sits on the iron yoke, 20 cm away from the inner. The peripheral layer is located 50 cm outside the yoke and covers the dead spaces in ϕ not covered by the inner or outer layers.

The Forward MUon chambers

Both arms of the MUF consists of two layers of chambers covering the angular regions $20° < \theta < 42°$ and $138° < \theta < 160°$, one inside the yoke after 85 cm of iron, the second 30 cm away behind the forward scintillator (HOF).
Each layer is divided in four quadrants, each consisting of two orthogonal planes of 22 drift tubes that are 4.3 m long with a cross-section of 18.8 cm by 2 cm and that are operated in limited streamer mode with a gas mixture of argon (15%), carbon dioxide (70%) and isobutane (15%). The planes are positioned at $90°$ to each other in the (x, y) plane to resolve the left-right ambiguity. Position information is obtained from the drift time measurements combined with delay line measurements which are also used to resolve left-right ambiguities.
Muon tracks crossing the chambers planes should produce 4 hits (two sets of

(x, y) measurements per layer).
The resolution averaged over all the layers in one endcap gives $\sigma_{xy} \simeq 5$ mm.
The Forward Muon chambers have been built, tested and installed by the Belgian groups of the DELPHI collaboration.

The Surround MUon chambers

As explained above, the DELPHI muon system consists of barrel and forward parts, leaving a gap of 8° around 50° in θ. The MUS were proposed to cover this intermediate region ($0.6 \leq |cos\theta| \leq 0.74$). This recent addition of the MUS has improved the hermiticity of the DELPHI muon identification. In addition it provides space point measurements with high efficiency and with an accuracy of about 1 cm.

2.2.5 The DELPHI calorimetry

A calorimeter is a detector that measures the energy deposited by incoming particles. All or most of the incident particle energy is converted into "heat", hence the name calorimeter for this kind of detector. Of course, it is not the temperature that is measured but rather some characteristic interactions with matter that generate a detectable effect. The interaction process between the calorimeter constituents (which are high density materials lead or iron) and the particle depends on the energy and the nature of the particle. Hence particles of different nature leave different trails of energy in the calorimeters. Reconstruction of these energy trails and measurement of the deposited energy enable particle identification using suitable calibration.

Electrons, positrons and photons loose their energy through electromagnetic (EM) processes. Above ~10 MeV their absorption in the calorimeters is a multistep combination of bremsstrahlung and pair production. Their absorption occurs within a small volume and leads to an EM shower which is used in their identification.
Muons also loose their energy via EM processes. However, their energy loss is dominated by ionization and is only ~2 MeV/g cm^{-2}. Their minimum ionizing trail in the calorimeters assists in their identification.
Hadrons traversing the calorimeter interact with one of the constituent nuclei. Hadronic shower development begins at this point and is similar to EM shower development, but with more complicated particle production mechanisms. Hadronic and electromagnetic shower profiles are similar but differ immensely in scale. For example, total absorption (at the 95% level) of 100 GeV electrons or photons requires ~21 radiation lengths (X_0). Whereas pi-

ons with similar energy require $\sim$6 nuclear absorption lengths (λ_0). For a lead calorimeter X_0 = 0.56 cm, λ_0 = 18.5 cm. Thus the pion is stopped in $\sim$110 cm and the electrons in $\sim$ 12 cm. This fact assists in hadron identification, in particular in e/π separation.

An overview of the design and performances of the DELPHI calorimeters is now presented.

The electromagnetic calorimeters

The purpose of the electromagnetic calorimeters is the detection and the energy measurement of photons and electrons. Two types of electromagnetic calorimeters are installed in DELPHI : the barrel electromagnetic calorimeter, which is a High density Projection Chamber (HPC) and the Forward ElectroMagnetic Calorimeter (FEMC) which consists of a set of lead glass blocks. The EM calorimeter is placed immediately after the outermost tracking chambers and covers a θ region down to 10° . The techniques used for the barrel EM calorimeter (HPC) and the one located in the endcap regions (FEMC) are different. Supplementary photon taggers have been installed to cover the 6° holes which remained between the HPC and FEMC at θ = 40° and the 90° and ϕ cracks in the HPC coverage.
There are also two very forward calorimeters, the STIC and the VSAT mainly used for luminosity measurements (see section 2.2.8).

The High density Projection Chamber The HPC is the barrel electromagnetic calorimeter. It is one of the first large-scale applications of the time projection principle to calorimetry. Its length is of 505 cm, it has an inner radius of 208 cm and an outer radius of 260 cm.
It consists of 144 similar modules built with an accordion-like structure of lead wires. These modules are arranged in 6 rings along the beam axis (z direction) of 24 sectors each in covering the angular region $41.5° < \theta < 138.5°$. Each module is made of 41 layers of lead wires providing about 18 radiation lengths (X_0) and alternated with 8 mm gas gaps, filled with an Ar-CH_4 (80/20 %) mixture.
For fast triggering purposes, a layer of scintillators is placed into a sample gap after 5 radiations lengths.

Figure 2.8 shows the schematic layout of the HPC : an incoming particle interacts electromagnetically with the lead and produces an electromagnetic shower. By sampling the shower at very short intervals and measuring the deposited charge, the energy can be calculated.

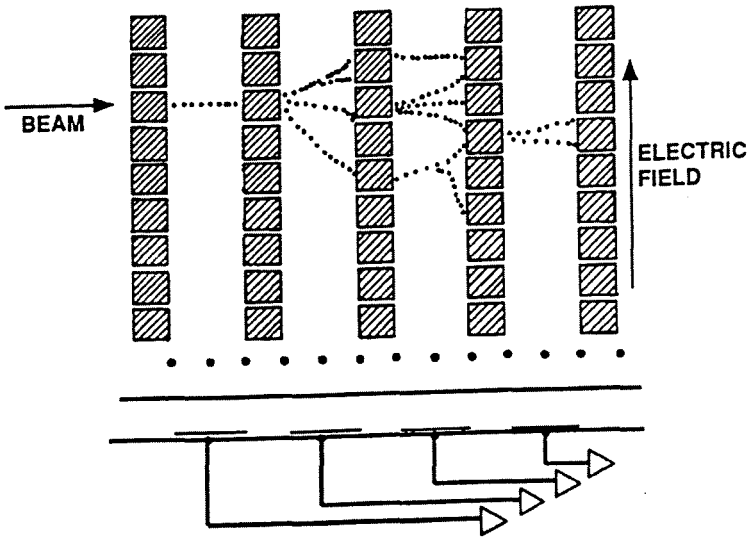

Figure 2.8: The HPC working principle

Ionization electrons from showers and tracks drift under the influence of the longitudinal electric field to the end plane of a module. This is the same technique as in the TPC, and again, detection at the end plane is via a proportional chamber and pad readout. The arrival position on the end plates gives $r\phi$ information and z is determined from the drift time. The relative precision on the measured energy can be parametrised as :[3]

$$\frac{\sigma_E}{E} = 0.043 \oplus \frac{0.32}{\sqrt{E}}(\%) \qquad [\mathrm{E} \rightarrow \mathrm{GeV}]$$

and the angular precisions for high energy photons are $\pm$ 1.7 mrad in ϕ and $\pm$ 1.0 mrad in θ.

The Forward ElectroMagnetic Calorimeter The principal aims of the FEMC are a good energy resolution and fine granularity.
The FEMC consists of two 5 m diameter disks each made up of 4532 lead glass scintillator blocks (20 X_0 deep) covering polar angles $10° < \theta < 36.5°$ and $143.5° < \theta < 170°$. The inner and outer radii are of 46 cm and 240 cm respectively. The blocks which have novel phototriode readout, are flat

[3] $\oplus$ denotes the square root of the sum of the squares

topped pyramids in shape which when arranged together point (-3°) towards the collision point. There is material present in front of the FEMC. Together this represents about 2 X_0 which degrades the energy and the shower position resolution of the FEMC. The resolutions are still good however and are as follows :

$$\begin{aligned} \frac{\sigma_E}{E} &= 0.03 \oplus (\frac{0.12}{\sqrt{E}}) \oplus (\frac{0.11}{E}) \ (\%) \qquad [\mathrm{E} \rightarrow \mathrm{GeV}] \\ \sigma_{x,y} &= 0.5 \qquad \mathrm{cm} \end{aligned}$$

The Hadron CALorimeter DELPHI is also equipped with a Hadron CALorimeter (HCAL) in both the barrel and the endcap regions. The HCAL (r_{in} = 320cm, r_{out} = 470 cm) detects neutral and charged particles and measures the total hadronic energy of an event. It essentially consists of 20 sandwich layers of 5 cm iron and 1.7 cm limited streamer mode detectors with a length of 760 cm. The detector consists of 24 modules in $r\phi$ and is incorporated in the return yoke of the magnetic field. The energy resolution in the barrel region was measured to be :

$$\frac{\sigma_E}{E} = 0.21 \oplus \frac{1.12}{\sqrt{E}} \qquad [\mathrm{E} \rightarrow \ \mathrm{GeV}]$$

The Forward Hadron Calorimeter It has the same function as the Barrel HCAL and covers polar angles between 11.2° and 48.5°, and 131.5° and 168.8°. It is made of 19 sandwiched layers of iron which are subdivided into 12 sectors equipped with detectors. It is located at $|z|$ = 340 cm and has a depth of about 150 cm.

2.2.6 The Ring Imaging CHerenkov detectors

As it has been mentioned, the DELPHI detector contains many novel subelements. However, it is the Ring Imaging Cherenkov detectors (RICHes) that makes DELPHI the most progressive of the four LEP detectors. The RICHes are based on the Cherenkov effect which occurs when a charged particle travels a material (called radiator) of refractive index n, with a velocity v greater than the light velocity in the same material :

$$v > \frac{c}{n}$$

where c/n is the velocity of light in the material.

The aim is hadron identification over a wide momentum range. This is

achieved by measuring the emission angle of the Cherenkov light with respect to the trajectory of the particle (θ_c) in both liquid and gas radiators ; the liquid radiator for particle identification in low momentum range (up to 8 GeV/c), the gas for particle of higher momentum (2 GeV/c $< p <$ 40 GeV/c). The velocity of the particle which has emitted Cherenkov radiation is determined from the measured angle θ_c by :

$$v = \frac{c}{n.\cos\theta_c}$$

Comparing v to the measured particle momentum enables its mass and hence its nature to be identified (see section 3.2).

The reader will find here only a short description of the RICHes. Actually, the physics analysis of this thesis is essentially based on the data recorded by the RICH counters of DELPHI between 1992 and 1994, the understanding of their working order and their performances is then a crucial point of our study. For this reason, chapter 3 is entirely devoted to the particles identification using the Cherenkov effect and gives a more detailed description of these detectors.

The Barrel RICH

The BRICH is shaped as a cylindrical shell (r_{in}=123 cm, r_{out}=197 cm) of 3.5 m in length. It covers the polar angle range $40° \leq \theta \leq 140°$.
It is designed to perform a pion, kaon and proton identification for particle momenta from 0.7 GeV/c up to 45 GeV/c (see section 3.2.2).

The Forward RICH

The FRICH is used for particle identification in the forward region. In the two endcaps, it covers an active area of ~ 8 m^2 between the polar angles $15° \leq \theta \leq 35°$ and $145° \leq \theta \leq 165°$. It works along the same principles as the BRICH combining liquid and gaseous radiators with a single photon detector (see section 3.2.3).

2.2.7 The scintillation counters

Scintillation counters have been used since the beginning of the century, making use of the property of certain chemical compounds to emit short light pulses after excitation by the passage of charged particles or by photons of high energy. In high energy physics experiments, scintillation counters

are used for timing (Time-Of-Flight counters : TOF, see below), for fast event selection (Trigger counters or groups of counters connected by fast logic into hodoscopes : HOF) or for measuring the energy of particles by total absorption in sampling calorimeters.

The Time of Flight detector

The TOF consists of scintillator counters surrounding the superconducting coil. It covers polar angles from 41° to 139° . Each of the 192 scintillators is equipped with a photomultiplier at both ends. It is used in the first level trigger of DELPHI and for elimination of cosmic events. The z-coordinate is measured with a precision of about 20 cm.

The Forward Hodoscope

The HOF also consists of scintillator detectors and is installed between the endcap yoke and the second layer of the muon chambers. It is subdivided into 4 quadrants with 28 counters each. It is used as a muon trigger in the forward region.

2.2.8 The luminosity detectors

The luminosity defines the rate of producing collisions between beams. One needs to know it to determine the number of expected events via any process in e^+e^- collisions. At e^+e^- colliders, the luminosity is measured by counting the number of events of a process with a clear experimental signature, with high statistics and with a cross-section which can be calculated theoretically with high precision. The process chosen is $e^+e^- \rightarrow e^+e^-$ elastic (Bhabha) scattering (the Feynman diagrams contributing to this process are given in figure 4.1) at small angles, which proceeds almost entirely through the exchange of a photon in the t-channel.

The integrated luminosity at each energy point E, $L_{int} = \int_0^t L dt$, is calculated as :

$$L_{int} = \frac{N_B}{\sigma_B(E)}$$

where N_B is the number of Bhabha events recorded during the time interval t in a θ interval at small angles and $\sigma_B(E)$ is the corresponding cross-section. The overall experimental precision of the luminosity measurement for 1994 data was 0.09% [3].

In DELPHI, before 1994, the absolute luminosity was measured using two detectors : the Small Angle Tagger (SAT) and the Very Small Angle Tagger (VSAT). In 1994, the SAT was replaced by a new calorimeter : the Small angle TIle Calorimeter (STIC).

The Small Angle Tagger

The SAT consists of two arms installed around the beam pipe at about 250 cm from the interaction point, at positive and negative z values (acceptance between 2.5° and 7.7° in θ). Each arm is composed of a tracking device and an electromagnetic calorimeter. The tracker provides 2 space points with a resolution of about 500 μm in radial direction. The calorimeter is 28 radiation lengths deep and has a relative energy resolution of about 4% for 45 GeV/c particles.

The Very Small Angle Tagger

The VSAT covers the very forward region from 0.29° to 0.40° in θ. It is 7.7 m away from the interaction point and consists of a 24 radiation lengths deep W/Si calorimeter with a relative energy resolution of about 5% for 45 GeV/c particles.

The Small angle TIle Calorimeter

The STIC replaces the SAT since 1994. It is a sampling lead-scintillator calorimeter formed by two cylindrical detectors placed on either side of the interaction region at a distance of 2.2 m and covers an angular region between 1.7° and 10.6° in θ (from 0.065 m to 0.4 m in radius). The blue light produced in the scintillator is read by wavelength shifting fibres placed perpendicularly to the scintillator planes. The total length of the detector is 27 radiation lengths.

At 45.6 GeV the energy resolution is given by $\frac{\sigma_E}{E} = 2.7\%$.

2.2.9 The Trigger system

The purpose of the trigger is to decide whether to accept an event for the Data Acquisition System (DAS) and to store it, or to veto it, in which case the DAS is made ready for the next event. The trigger system must be able to cope with a large luminosity and large background event rates.
Ideally the trigger would consist of a number of subtriggers that can independently pick out a signal from background with a high level redundancy and

efficiency. Also, the trigger decision should be made as quickly as possible to limit the dead time of the DAS.

At LEP, with an 8 bunch configuration, about every 11 μsec a Beam Cross Over (BCO) occurs which corresponds to a data taking rate of about 90 kHz. Long drift times, such as 20 μsec for the TPC, and time taken to process subdetector signals for event reconstruction, reduce the maximum data taking rate to a few Hz.
In order to reduce the taking of useless data and select Z^0 events a four level trigger of increasing selectivity was installed (T1, T2, T3, T4).
The first two trigger levels are synchronous with respect to the BCO signal (every 11 μsec). The T1 and the T2 trigger decisions are taken 3.5 μsec and 39 μsec after the BCO respectively. In the case T1 fires, the T2 trigger confirms or rejects the T1 trigger by analysing the information of slow detectors. T3 and T4 are software filters performed asynchronously with respect to the BCO. T3 confirms or rejects T2 decision on the basis of full reconstruction of the event. T4 runs after the data acquisition and flags events for physics analysis, reduces remaining background events and provides monitoring facilities in the form of online event viewing.
The global trigger efficiency for electron and muon pairs is consistent with 1 at the level of 10^{-4} for θ between 20° and 160°. Due to their high final state multiplicity, hadronic events ($e^+e^- \rightarrow Z \rightarrow$ hadrons) are triggered with an efficiency hardly distinguishable from 1 over nearly the full solid angle.

2.2.10 Data acquisition, Control and Monitoring

The DELPHI online system performs two basic tasks :

- Control, acquisition and monitoring of the detector data (Data Acquisition System (DAS) [4] and Quality Checking system (QC) [5]) ;
- Control, acquisition and monitoring of the detector technical parameters (Slow Controls system [6]) .

- The Data Acquisition System reads out digitised data from the detector, and stores them for subsequent analysis. Before 1995, the disk files were then copied locally onto IBM3480 cartridges. Now they are sent over the FDDI optical link network to a Central Data Recording facility at the CERN computing centre where they are copied onto high capacity tapes (10 GByte Digital Linear Tapes). From there, the offline data analysis centre of DELPHI performs the final event reconstruction.

- The Quality Checking system as such is a complete environment made of various software tools. The primary aim is to be able, at any time, to monitor the performance of the whole chain of data taking : i.e. performances of the DELPHI detector as well as of the Data Acquisition and Trigger system, writings to the database, calibration of the different subdetectors and reconstruction of tracks.

- The Slow Control system is an automated system for monitoring and controlling technical aspects of the experiment, and for reporting and acting on changes in the status of the detector or its environment. During data taking, significant changes in the parameters which are relevant to the subsequent data analysis (such as chamber pressures, temperatures, voltage values or the operation status of any subdetector) are recorded on the central database [7] by the 'Elementary Process'. This is achieved using a dedicated server process, which sends a copy of all updates to the offline data analysis centre where they can be exploited by the analysis program.
This system allows a single operator to oversee 12 609 detector monitoring and control channels. High voltages trips and many similar causes of data loss can usually be dealt with rapidly, often automatically.

2.3 The data analysis chain

The main components of the DELPHI analysis system are :

- **A Monte Carlo simulation program :** To verify the significance of the measurements, the different physics processes together with the apparatus component response to the different reactions have to be modelled by Monte Carlo studies. The **DEL**phi **SIM**ulation program (DELSIM) [8] was built to make comparisons between theory expected results and quantities measured by the DELPHI detector. This program first generates events (according to the Standard Model theory) and then performs the tracking of the particles through the whole detector and simulates the response of each crossed subdetector.

- **A data analysis program :** The **DEL**phi **ANA**lysis program (DELANA) [9] is necessary to convert raw data that the DELPHI detector produces into standard physics quantities such as vertex position of the event, particle momenta, particle type, etc.

- **An event viewing system :** This system gives the possibility to display the results of the DELPHI analysis software. It is used to check events selected in particular analysis or to understand how the detector works.

A short description of these programs is given in the following sections.

2.3.1 The DELPHI Monte Carlo simulation program

The simulation procedure presents two subsequent phases :

- Simulation of the kinematics and the dynamics of the physics process like $e^+e^- \rightarrow Z/\gamma \rightarrow f\bar{f}$ (f = lepton, quark), generated by dedicated programs, so-called, physics event generators. In this first phase, called *event generation* phase, no detector characteristics are used.

- Tracking of the final particles, which have been created in the physics process, through the detector magnetic field. The response of the detector subcomponents together with interaction between particles and the detector material and secondary particles production are also simulated. This phase is called the *detector simulation* phase. During this phase, the Monte Carlo program extracts information from a database which contains the full description of the geometry and material characteristics of the different subdetector together with their inefficiencies.

The event generation

Figure 2.9 shows a schematic view of the e^+e^- annihilation : electron and positron produce a fermion pair ($f\bar{f}$) via a real Z^0 or a γ particle in the s-channel. For quark final states, the event generator is based on the JETSET 7.3 program [10] which uses the Parton Shower (PS) model and the String Fragmentation model [11]. The fragmentation (also called hadronization) is the production of hadrons from the $q\bar{q}$ pair.

The simulation of the entire process can be divided into four steps :

- In the first step, the Z^0 boson produced by the annihilation of the incident electron and positron decays subsequently into the primary quark pair $q\bar{q}$ which may radiate real photons (= final state radiation). Up to this point,

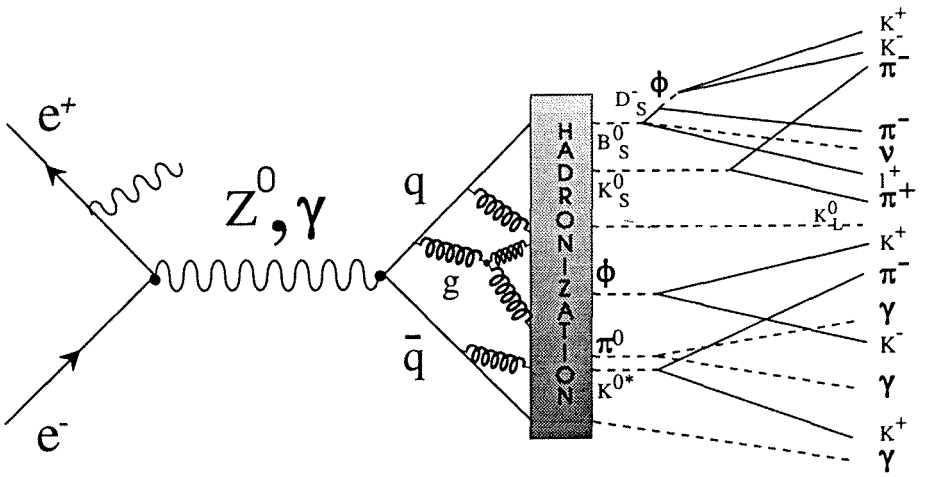

Figure 2.9: Schematic view of the generation of hadronic event.

the interaction is described by the Standard Model of electroweak interactions (Glashow-Weinberg-Salam model) discussed in chapter 1. The angular distribution $\frac{d\sigma}{d\cos\theta}$ of the resulting quarks can approximately be expressed as :

$$\frac{d\sigma}{d\cos\theta} \sim A + B\cos^2\theta + C\cos\theta \tag{2.2}$$

where θ is the angle between the quark and the electron beam axis in the centre-of-mass system. This leads to the forward-backward asymmetry, the subject of this thesis and fully defined in chapter 4.

• In the second step, the primary quarks can radiate gluons which decay into secondary $q\bar{q}$ pairs (collectively called partons). This can be calculated by perturbative QCD. It is usually described by the Lund Parton Shower (PS) model where partons interact following three basic reactions : $g \rightarrow gg$, $g \rightarrow q\bar{q}$ and $q \rightarrow qg$.

• The third step is called the fragmentation (or hadronization) phase in which coloured final state partons are combined into colour neutral final state hadrons. This phase can only be described by phenomenological models. One of these models in the Lund Monte-Carlo is the so-called "String Fragmentation" model. This model is based on the idea that the energy of a produced quark pair is stored in a colour flux tube (or string), whose potential energy increases with the distance between quarks. The potential energy can reach a level where the string breaks up : a new quark anti-quark pair is produced. This results in two smaller strings which in turn may break

up until only on-shell hadrons remain. The fragmentation process is implemented through a function $f(z)$ which determines the probability that a quark radiates a gluon with a fraction z of the original quark momentum. In the present analysis, the Lund Monte-Carlo model is used. In this model, the fragmentation function for light quarks (u, d and s) has the form :

$$f(z) \propto \frac{(1-z)^a}{z} \exp\left(-b\frac{m_T^2}{z}\right) \tag{2.3}$$

$f(z)$ is called the Lund symmetric function. The coefficients a and b are the so-called fragmentation parameters and m_T is the transverse mass of the created parton ($m_T^2 = m^2 + p_\perp^2$). For inclusive spectra good agreement between experimental data and Monte Carlo data can be obtained with $a = 0.5$, $b = 0.9$ GeV^{-2} [10].
Light quark fragmentation is rather well described by this function. For heavy quarks (b and c), the LEP data showed that their fragmentation is better described by the Peterson fragmentation function [12] :

$$f(z) \propto \frac{1}{z}(1 - \frac{1}{z} - \frac{\epsilon_q}{(1-z)})^{-2} \tag{2.4}$$

where ϵ_q is a quark flavour dependent parameter proportional to $1/m_q^2$ and which is determined experimentally. The production probability of a quark pair in the string fragmentation model is proportional to $\exp(\frac{-\pi m_T^2}{\kappa})$ where κ is the energy per string length, about 0.2 (GeV/c)^2. This leads to a suppression of the heavier strange pair production as compared to the other light quarks (u and d) which may be estimated as :

$$\gamma_u \ : \ \gamma_d \ : \ \gamma_s \ : \ \gamma_c : \ \gamma_b \ \simeq \ 1 \ : \ 1 \ : \ \frac{1}{3} \ : \ 10^{-11} \ : \ 10^{-100}$$

This means also that $c\bar{c}$ and $b\bar{b}$ pair production essentially never occur during a soft hadronization process (but only in the perturbative phase).
The hadronic event generator used for this analysis (and the most often used in the DELPHI experiment) is JETSET PS 7.3 [10]. This generator contains a parametrised model which is based on experimental data collected at various centre-of-mass energies. The purpose of the parametrisation is to reproduce the observed particle multiplicities and angular distributions in the generated samples. This parametrised model thus includes several input parameters which can be tuned in order to correspond to the centre-of-mass energy in question. A table listing these various input parameters, their standard values and the ranges in which they can vary can be found in Appendix B.

• After the fragmentation, we are left with hadrons. These created particles, if instable, decay into stable particles. Here the Monte Carlo program has to rely on measured quantities like masses, branching ratios, decay widths and quantum numbers.

The detector simulation

At the end of the event generation phase, we are left with particles and their four-momenta. These particles are then passed through the detector simulation which tracks these particles in the DELPHI magnetic field. This is the main feature of DELSIM.
The accuracy of this tracking is highly dependent on a very detailed and very good description of each subcomponent of the detector and the field map. This forms the so-called detector description database which is further used to simulate the response of the detector, generating the same signals as those in a real event.

2.3.2 The DELPHI data analysis program

The simulation data are processed with the same reconstruction program called DELANA, as the real event data. DELANA is thus the standard program of the DELPHI analysis chain. It relies on databases containing all the online information on the alignment, calibration, running conditions for each subdetector, LEP running conditions, etc. All these elements are needed to reconstruct a DELPHI event.

The program is divided into two pattern recognition stages. In the first stage of the processing, the event reconstruction is performed for each subdetector working independently. The raw data are decoded and calibrated and noise suppressed. The tracking chambers give space points (as the VD) and fully reconstructed track segments (as the TPC) and the calorimeters produce energy clusters and showers. These track elements provide the input to the global track search.
In the second stage of the processing, each subdetector performs pattern recognition but now using the other subcomponent informations. For example, a track is reconstructed by putting together the various track elements from each detector. In the global fit of the event, all the subdetectors are then combined. The complete tracks with their physics parameters, such as momentum, charge,... are reconstructed and clues on identification are added.

Particle identification

At this stage, a global identification processor tries to identify each particle which created tracks and showers. The DELPHI mass identification algorithm uses the information coming from :

- The TPC makes use of the dE/dx data to distinguish between e, π and K ;
- The RICHes : Ring reconstruction results to distinguish between π (e,μ), K, and protons ;
- The HPC and FEMC : shower data to distinguish between γ, e and hadrons ;
- The HCAL : shower data to distinguish between μ and hadrons ;
- The MUB, MUF and MUS : results from hits matching tracks to distinguish between μ and π.

The identification using the RICHes on which the present study is based is discussed in chapter 3.

DST format

When the whole DELPHI data analysis chain is at its end, the event information is written out in a DST (Data Summary Tape) format which is used for the physics analysis. For each event, a linear structure containing the essential physics quantities for a track (momentum components, track length, impact parameters, etc) is created.

The DELphi SIMulation program (DELSIM) produces data with the same structure as the online real data and the DELANA program treats the simulated data in the same way as the real events.

Bibliography

[1] LEP Design Report, CERN Report LEP/84-01 (1984).

[2] DELPHI Coll., P. Aarnio et al., *Nucl. Instr. and Meth.* **A303** (1991) 233.

[3] DELPHI Coll., P. Abreu et al., *Nucl. Instr. and Meth.* **A378** (1996) 57.

[4] DELPHI report 91-92 DAS 112;
DELPHI report 91-93 DAS 113;
DELPHI report 92-99 DAS 128.

[5] DELPHI report 95-32 DAS 165.

[6] T.J. Adye et al., *Nucl. Instr. and Meth.* **A349** (1994) 160; expanded in : The Design and Operation of the Slow Controls for the DELPHI Experiment at LEP, DELPHI report 94-14 DAS 151.

[7] DELPHI report 93-5 PROG 195;
DELPHI report 93-4 PROG 194.

[8] DELPHI report 89-67 PROG 142;
DELPHI report 89-68 PROG 143.

[9] DELPHI report 89-44 PROG 137.

[10] CERN report TH.7112/93.

[11] Andersson B. at al., *Physics Reports* **97** (1983) 31-145.

[12] C. Peterson, D. Schlatter, I. Schmitt, P. Zerwas, *Phys. Rev.* **D27** (1983) 105.

[13] P. Abreu et al., DELPHI Coll., *Z. Phys.* **C73** (1996) 11.

Chapter 3

The Cherenkov effect and its applications : The RICH detectors of DELPHI

This chapter is devoted to the understanding and the description of the Ring Imaging CHerenkov detectors of the DELPHI experiment as they play an important role in our analysis.
We first explain the Cherenkov effect on which the RICH detectors are based as well as some applications of this electromagnetic effect. We then give an overview of the technical characteristics of the RICH detectors installed at the DELPHI experiment.
We conclude by evaluating the identification power of the RICH detectors of DELPHI.

3.1 The Cherenkov effect and its applications

3.1.1 Introduction

The russian physicist P.A. Cherenkov [1] was the first scientist who studied the phenomenon of emission of bluish-white light from transparent substances in the neighbourhood of strong radioactive sources. Between 1934 and 1938 he performed an exhaustive series of experiments leading to the insight that the effect was different from fluorescence and other known forms of luminescence. His results were in excellent agreement with a theory proposed in 1937 by Frank and Tamm [2]. In 1958, the Nobel Prize for physics was awarded to Cherenkov, Frank and Tamm for their work on the effect that has been named after its discoverer.

This section starts with charged particle identification based on the Cherenkov effect. Three types of Cherenkov counters are briefly discussed before entering in the main application, as far as this work is concerned, of Cherenkov radiation in the RICH counters of the DELPHI detector at LEP.

3.1.2 The Cherenkov effect

The electromagnetic field produced by a charged particle in its neighbourhood polarises locally the molecules of the medium in which the particle is moving. The electromagnetic radiation subsequently emitted by depolarisation is called the Cherenkov radiation which is basically a shock-wave phenomenon.
The angle of emission (θ_{ch}) of the shock-wave with respect to the trajectory of the particle is straightforwardly obtained using Huygens' principle as illustrated in figure 3.1 :

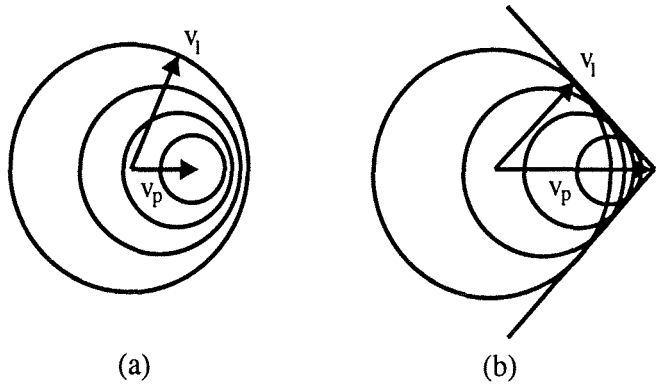

Figure 3.1: Emission principle of Cherenkov effect : (a) $v_p < v_l \rightarrow$ no emission of light, (b) $v_p > v_l \rightarrow$ Cherenkov light emission.

- If the velocity of the particle (v_p) is smaller than the velocity of the light (v_l) in the same medium, the waves emitted along the trajectory interfere destructively : there is no shock-wave formed and thus no emission of light.

- If v_p is greater than v_l, they interfere constructively : a shock-wave is formed according to Huygens' principle. The charged particles emit radiation in a well defined direction with respect to the line of flight of

the particle : in azimuth isotropically around the track of the particle. Therefore, we observe emitted photons in a cone having the trajectory of the particle as axis and the position of the particle as vertex.

The angle between the direction of the particle and the emitted radiation is called the Cherenkov angle θ_c and is given by :

$$\cos\theta_c = \frac{v_l}{v_p}$$

For a charged particle travelling in a transparent dielectric medium of refractive index n, the two velocities v_p and v_l can be expressed as :

$$v_p = \beta c$$

$$v_l = \frac{c}{n}$$

where c is the light velocity in the vacuum. The refractive index of the medium being thus defined by : $n = \frac{c}{v_l}$, we obtain :

$$\cos\theta_c = \frac{1}{\beta n} = \frac{1}{n\sqrt{1-\frac{1}{\gamma^2}}} \tag{3.1}$$

with $\beta = \frac{v_p}{c}$ and $\gamma = \frac{1}{\sqrt{1-\beta^2}}$ (Lorentz variable).

The Cherenkov angle depends on two parameters : the refractive index of the medium (n) and the particle velocity (β). Consequently, the measurement of the Cherenkov angle in a detector with fixed refractive index n gives information about the velocity of the particle which together with a measurement of its momentum p allows one to determine its mass m and thus to identify it. We have :

$$m = \frac{p}{\beta\gamma} = p\sqrt{n^2 cos^2\theta_c - 1}$$

This shows that a detector based on the Cherenkov effect is not a stand-alone detector but depends on the surrounding tracking detectors for the measurement of the momentum. The behaviour of θ_c for a certain radiator material as a function of the particle momentum and the particle mass is given in figure 3.2.

From the Cherenkov relation 3.1, we deduce that :

- for a medium of given refractive index n, there is a threshold velocity : $\beta_{min} = (1/n)$, below which no radiation is emitted. At this critical velocity the direction of radiation coincides with that of the particle.

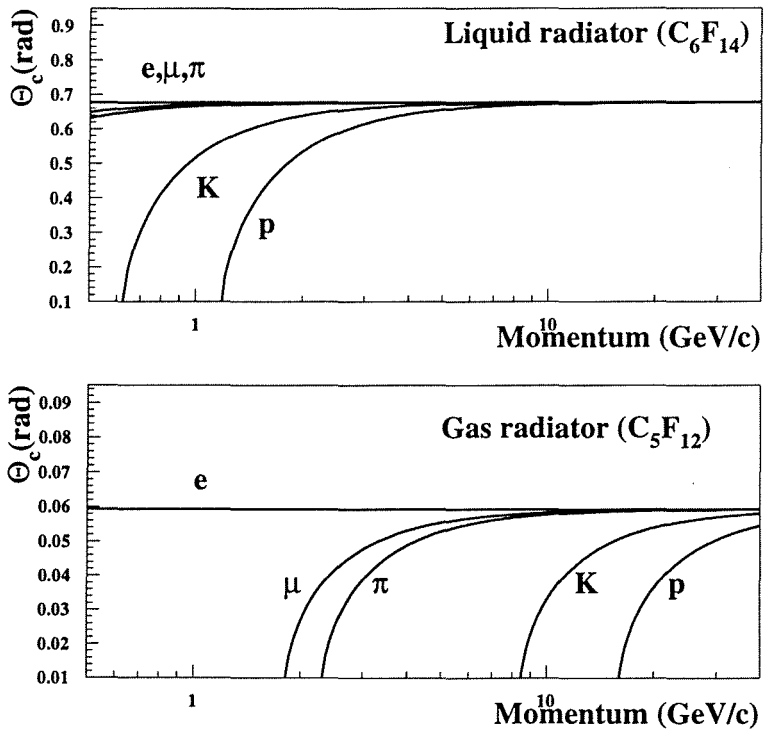

Figure 3.2: Expected Cherenkov angle versus particle momentum for e, μ, π, K and proton. (a) Liquid radiator, $n = 1.283$; (b) Gas radiator, $n = 1.00176$

- for an ultra-relativistic particle, for which $\beta \sim 1$, there is a maximum angle of emission, given by $\theta_{max} = arcos(1/n)$.

The number of photons produced per unit path length (dL) of a particle and per unit energy interval (dE) of the photons can be written as :

$$\frac{d^2N}{dE\ dL} = \frac{Q^2\alpha}{\hbar c}\sin^2\theta_c$$

where, Q is the charge of the particle in electron charge units. We note that, for fixed β, θ_c increases with the refractive index n and so, does the number of photons. But the radiated energy is not infinite because of the frequency dependence of the refractive index $n = n(\omega)$. The Cherenkov radiation is emitted only in those frequency bands for which $n(\omega) > 1/\beta$.

The number of detected photons in a given Cherenkov detector is deduced from [3] :

$$N_{detected} = N_0 \; L \; \sin^2 \theta_c$$

where N_0 is a 'quality parameter' of the counter (fully discussed in section 3.3), expressed in terms of an integral over the photon energy $\bar{h}\omega$ (in eV) of the photon detector efficiency function $\epsilon(\bar{h}\omega)$:

$$N_0 = 370 \; cm^{-1} \; eV^{-1} \int \epsilon(\bar{h}\omega) \; d(\bar{h}\omega)$$

The integral is taken over the wave length range in which the photons are detected. We shall see later that for the DELPHI RICHes this range goes from 160 nm to 220 nm (see figure 3.7), the first limit being set by the transparency cutoff of the quartz walls and the second by the quantum efficiency of the TMAE [1].

3.1.3 Applications of the Cherenkov effect

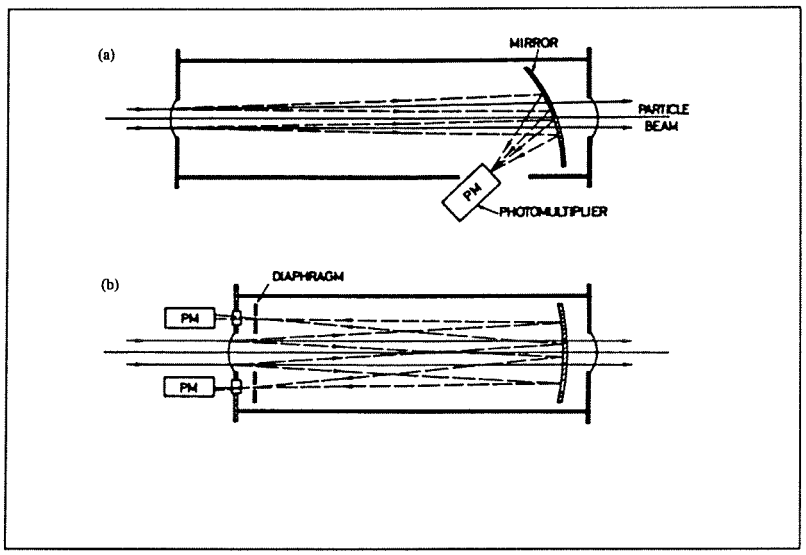

Figure 3.3: Layout of (a) a threshold Cherenkov counter and (b) a differential Cherenkov counter.

The threshold Cherenkov counter

The first application of the Cherenkov effect for identifying particles does not use explicitly the Cherenkov angle information. It detects particles that have

[1] TMAE ≡ Tetrakis diMethyl Amino Ethylene, photosensitive agent.

a velocity sufficiently high to produce Cherenkov light in its radiator and it is only based on the fact that it exists different momentum thresholds for different possible masses. As explained in the previous section, the threshold velocity β_{th} depends on the refractive index n of the medium : $\beta_{th} = 1/n$. Two particles that have the same momentum but different masses m_1 and m_2 ($m_2 > m_1$) can be discriminated by appropriate selection of the refractive index, such that particle m_1 will emit Cherenkov light whereas particle m_2 will not. Identification of more than two kinds of particles is possible by placing several threshold counters in series.
The layout of a threshold counter is shown in figure 3.3(a). The Cherenkov light is focused by a mirror onto a single photo-multiplier.

The differential Cherenkov counter

In a differential Cherenkov counter the emission angle of Cherenkov radiation is explicitly used. Since the Cherenkov light is emitted at a given angle , it appears to an observer to come from a circle positioned at infinity. Focusing optics can be used to concentrate this light onto a ring image of radius r in the focal plane of the system. The radius r is given by $r = f.\tan\theta_c$, where f is the focal length of the optics. The basic principle of the differential Cherenkov counter is to detect these ring images using diaphragms placed in front of photodetectors (see fig. 3.3(b)).

The ring imaging Cherenkov counter

The differential Cherenkov counters described in the previous section have several drawbacks. Figure 3.4 shows the principle of a Ring Imaging CHerenkov (RICH) counter.

This technique was proposed by J. Seguinot and T. Ypsilantis [4]. The Cherenkov radiation emitted by a crossing particle is focused by a spherical mirror of radius R surrounding the interaction region at its centre, on a detection surface of radius $\frac{R}{2}$. The radiating medium fills the area between $\frac{R}{2}$ and R. For particles originating from the optical centre of the mirror and for particles that are slightly off axis, the image is practically a ring.

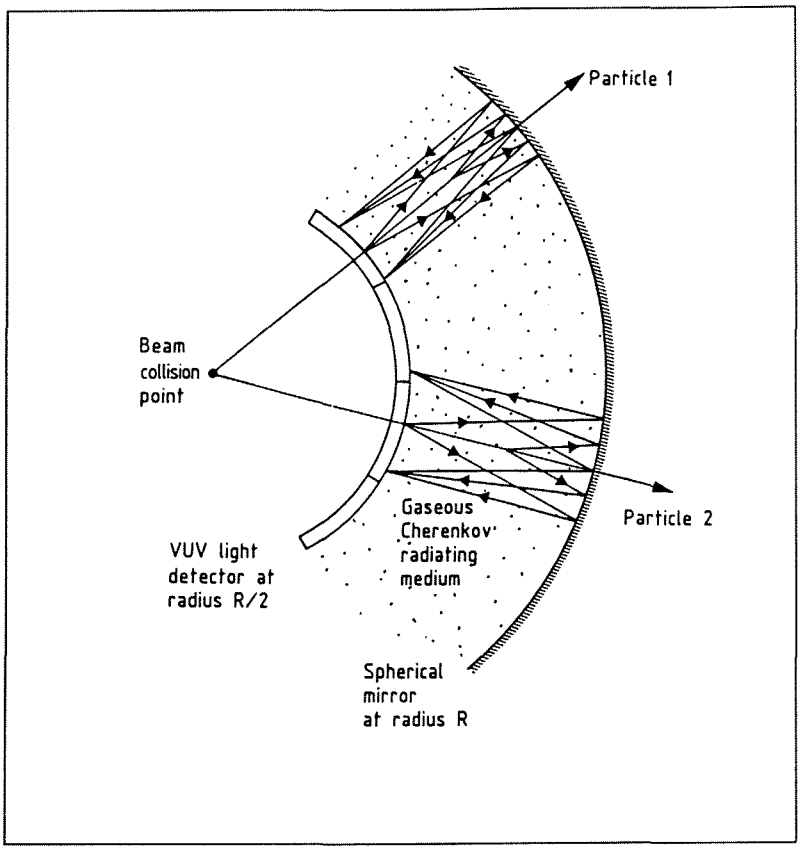

Figure 3.4: Principle of a large phase space acceptance ring imaging Cherenkov detector.

3.2 The RICH detectors of DELPHI

3.2.1 Introduction

At the time the DELPHI letter of intent was submitted (1982) the technique of Ring Imaging Cherenkov (RICH) counters was still in development. It was decided to build a prototype to study the feasibility and the performance of a big RICH system. The knowledge and experience gained in different works [5], combined with results from smaller and more specific setups led to the design of the final RICHes of the DELPHI detector.

The aim of the Cherenkov counters is to provide particle identification by the detection of the light emitted in UV transparent media. The Ring Imaging Cherenkov detector system in the DELPHI experiment is designed for hadron (π , K, p) identification in the momentum range from 2 GeV/c to

40 GeV/c. In order to cover most of the solid angle two detector systems have been built, the Barrel RICH [6] of cylindrical geometry which covers the barrel region and the Forward RICH [7] located in the endcap regions. Figure 2.1 shows their exact position inside the DELPHI assembly. Using cylindrical coordinates r, ϕ, z with the z-direction along the beam axis, the Barrel RICH covers the polar angles $40° < \theta < 140°$, the Forward RICH, $15° < \theta < 35°$ and $145° < \theta < 165°$.

Although different in geometry, they employ the same principle as schematically drawn on figure 3.5 :

- detection in a single array of photosensitive Time Projection Chambers (TPC) of the Cherenkov UV photons produced by the particle in the Cherenkov media;
- measurement of the three coordinates of each UV photon conversion point;
- reconstruction of the measured emission angle for each detected photon with respect to the particle trajectory;
- from the momentum, test of the mass hypotheses against the observed number of photons and the distribution of the Cherenkov angles of the individual photons.

The DELPHI RICH detectors are not stand-alone detectors. For the determination of the particle momentum and the impact point of the particle, they rely on the tracking detectors in the 1.23 T magnetic field. Therefore, they are placed between specialised tracking detectors.
The Barrel RICH is situated between the principal tracking device of DELPHI, the Time Projection Chamber and the Outer Detector. It was fully installed and operational by the end of 1991.
The Forward RICH sits between Chamber A at the end-plate of the Time Projection Chamber and Chamber B. It was a staged item, but is now fully installed and operational. It has been taking data since 1993 (one quarter took already data during 1992 LEP running).

Throughout the 1994 data taking period, 1.5 million events were recorded with a fully operational detector. In the previous years, the Barrel RICH has recorded 0.24 million events with both radiators (liquid and gaseous), and 0.73 million events with the gas radiator only.

A detailed description of these two RICH counters of is given in references [6]

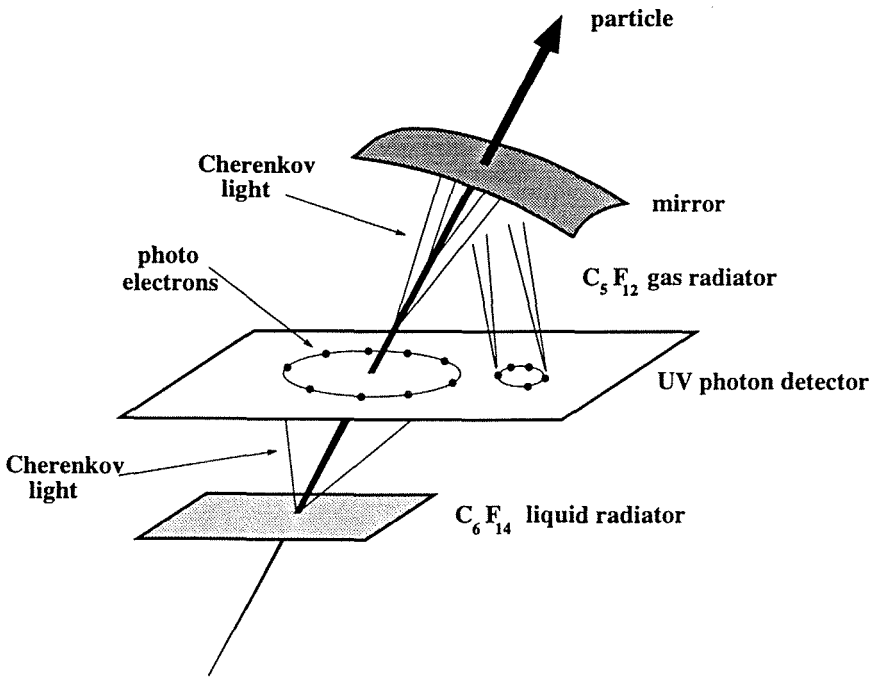

Figure 3.5: Schematic drawing of the DELPHI RICHes working principle [8].

and [7]. Only the main characteristics will be recalled in the following sections.

3.2.2 The Barrel RICH of DELPHI

The design of the Barrel RICH is shown in figure 3.6. It is a cylindrical detector, 3.5 m long, with an inner radius of 123 cm and an outer radius of 197 cm, divided into two halves by a central support wall, 6.5 cm thick. It covers the angular region in θ between 41.5° and 138.5° . These two identical halves, located at each side of the interaction point, are both segmented azimuthally in sections of 15° . Each section contains a liquid radiator (C_6F_{14}), a drift tube with a MWPC and 6 mirrors. The rest of the volume is filled with gas (C_5F_{12}). The Cherenkov photons from the liquid radiator and the gaseous radiator hit the same drift tube from bottom and top respectively. The gas inside the drift tube is a mixture of CH_4 and C_2H_6 with TMAE as photosensitive agent.
The reason for using two types of radiators is to extend the momentum region over which particles can be identified. Some important properties of those radiators can be found in table 3.1. The liquid radiator is used for particle identification in the momentum range from 0.7 to 8 GeV/c. The gaseous radiator is used from 2.5 GeV/c to 25 GeV/c.

Radiator material	*refr. index n at 7eV, 1atm.*	*boiling point*	$\Delta n/(n-1)$ $6.5-7.5eV$	$p_{th}(GeV/c)$			$p_{max}(GeV/c)$		
				π	K	p	π	K	p
C_6F_{14}	1.2834	57°C	3.0%	0.17	0.61	1.17	1.2	4.3	7.8
C_5F_{12}	1.00176	28°C	2.9%	2.35	8.32	15.8	7.8	25.0	47.0

Table 3.1: Some important properties of the radiator materials of the BRICH. p_{th} is the threshold momentum for the particles. p_{max} is the practical upper limit of momentum above which the particles cannot be distinguished from each other, taking into account the current definition of σ.

The operation of the Barrel RICH has imposed the following design constraints :

- The drift tube is made entirely of UV transparent quartz plates in order to match the spectral quantum efficiency of the TMAE.

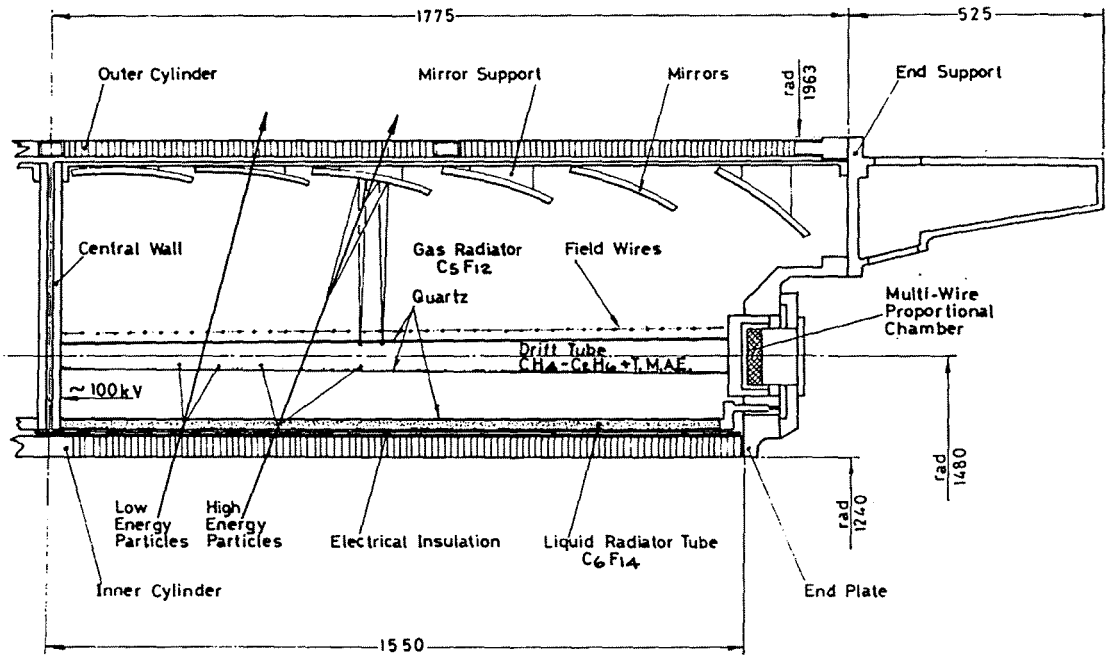

Figure 3.6: Longitudinal view of a quarter of the Barrel RICH.

- The operating temperature of the detector is 40° since the radiator gas condenses at room temperature (28°) and the vapour pressure of TMAE allows a sufficiently high concentration in that temperature range only.
- The drift field - up to 1kV/cm - ensures drifting without distortions and is obtained applying Very High Voltage (VHV) of up to 80 kV on the mid-wall. This requires good electrical insulation and demands great care in designing the electrostatics to avoid any corona and field deformation.
- The Barrel RICH is operated at 1030 mbar so that the gas refractive index is high enough to overlap the identification range of the gaseous radiator with the one of the liquid radiator.

In the following sections the main components of the Barrel RICH are described.

The Vessel

The Barrel RICH detector is enclosed in the space between two cylinders, the inner and the outer cylinders, closed at each end by an endflange. The cylinders are made of aluminium honeycomb sandwiches. All vessel components are equipped with heating facilities in order to maintain the temperature of 40° .
The inner cylinder together with several other parts of the Barrel RICH plays a role in the formation of the electric field. The mid-wall is connected to the drift Very High Voltage which is degraded along the length of the inner cylinder in a controlled way down to zero at the endflanges.
The outer flanges constitute the mechanical reference for the Barrel RICH on which are fixed the mirror cages, the drift tubes with the MWPC's and the liquid radiator tubes.

The Liquid Radiator

The 48 liquid radiator containers (length=150 cm, width=34 cm, internal height=1cm) consist of trays made from composite material closed by 4 mm thick UV transparent quartz windows. Two containers are glued together and form one mechanical unit. The radiating medium is a 1 cm thick layer of liquid C_6F_{14} with an index of refraction of $n = 1.2834$ (at 7 eV and 1 atm). The Cherenkov photons produced by tracks with normal incidence onto the photon detector are distributed homogeneously around the track in a circular

pattern. For tracks incident at an angle they are distributed in a conic-section pattern. They are usually called 'rings'.

The Gas Radiator

Contrary to the liquid radiator the gas radiator is not 'thin'. The C_5F_{12} gas fills the entire space left between all the other elements of the BRICH ($\sim$ 24 m^3 of C_5F_{12}). The UV radiation produced along the particle path after the drift tube is reflected by parabolic mirrors and focused onto the drift tube. The UV photons form together a ring-like image in the focal plane of the mirrors which is located just inside the drift tube.
In order to maintain a good UV-transparency, the radiator gas is continuously circulated through filters in order to remove the main polluting agent : H_2O and O_2 .

The Mirrors

Every 15° section of the Barrel RICH contains 6 parabolic mirrors (288 in total) which are associated with each single drift tube. They are coated with 50 nm thick layer of Al and 60 nm thick protective layer of MgF_2. The reflectivity is better than 90% in the relevant wavelength range of 165 - 230 nm. Cherenkov photons produced in the outer gas volume are reflected by these mirrors and focused into ring images in the drift tubes.

The Mid-Wall Mirror

The mid-wall mirrors are mounted on the central wall, between the liquid radiator boxes and the drift tubes. They reflect liquid radiator photons from tracks close to $\theta = 90°$ back to the drift tube. Without these mirrors the photons would be absorbed by the mid-wall.

The Photon Detector

The photon detector is an important component of the BRICH. It consists of a TPC-like drift volume with a Multi Wire Proportional Chamber (MWPC) at the front end. The drift volume is entirely enclosed by UV transparent quartz walls in order to admit the Cherenkov light from both radiators. It is filled with a mixture of 75% CH_4, 25% C_2H_6 and TMAE. Inside the drift

volume, the Cherenkov photons liberate electrons by ionization of the photosensitive vapour TMAE. This vapour is added to the drift gas in small quantities. Photons with energies higher than 5.5 eV can ionize TMAE.
The transmission curves of the different elements used in the Barrel RICH and the quantum efficiency curve of the TMAE are shown in figure 3.7. The cutoff energy of the quartz transmission being about 7.5 eV, the photon detection window is about 2.0 eV wide. In order to separate as much as pos-

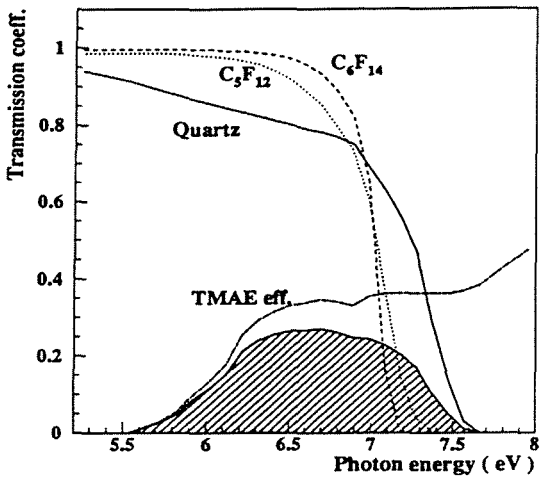

Figure 3.7: Quantum efficiency of TMAE and transmission curves of quartz and radiator materials. The curves are for a TMAE temperature of 35°C, 1 cm quartz, 1 cm C_6F_{14}, 100 cm of C_5F_{12}. The shaded area gives the convolution of the TMAE efficiency and the quartz transmission.

sible the signals from the two radiators in the relatively thin photon detector, the TMAE concentration is adjusted such that photons are absorbed with a mean free path of about 1.0-1.5 cm. Thus photoelectrons created by the liquid radiator are mainly found at the liquid radiator side of the drift tube while gas radiator photoelectrons are found mainly at the mirror side.

The photoelectrons drift in an homogeneous, (anti-)parallel magnetic and electric field towards the MWPC at the end of the drift tube where they are gas amplified by a factor of about 2.10^5. The amplified chamber signals are read from anode wires and cathode strips and thus provide the x-y coordinate of the photoelectron. This readout of the three coordinates allows a spatial reconstruction of the photon conversion point. Using the extrapolated track,

the Cherenkov angle can be reconstructed.

The Barrel RICH contains in total 48 (2 x 24) drift tubes. As shown in figure 3.8 two drift tubes are combined with one endflange and a support structure to form a so-called bitube.

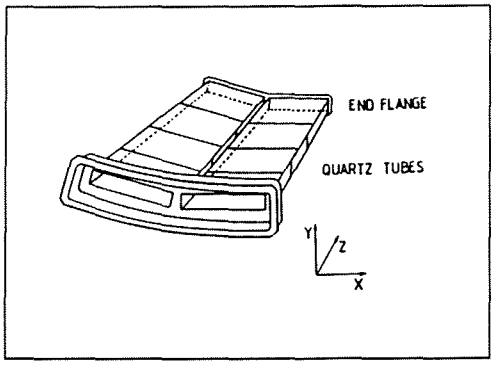

Figure 3.8: Schematic drawing of a bitube.

The Calibration System

A calibration system is used to measure the drift velocity of the photoelectrons in the drift gas and to observe any distortions of the electric field lines mainly due to the presence of space charges. The system is also able to follow time dependent changes in the drift velocity due to changes in the temperature, pressure and gas composition.
The calibration system consists of a matrix of 5x9 well defined UV light spots projected via quartz fibres from a central lamp onto each drift structure. The central lamp is triggered only when an exclusive forward trigger is present in the whole DELPHI detector (Forward-Bhabha trigger with in particular no tracks in the barrel region). This avoids mixing of 'good' photoelectrons and those coming from the calibration system.

The accuracy obtained on the drift velocity is better than 0.07% (V_d = 5.3 cm/μs).

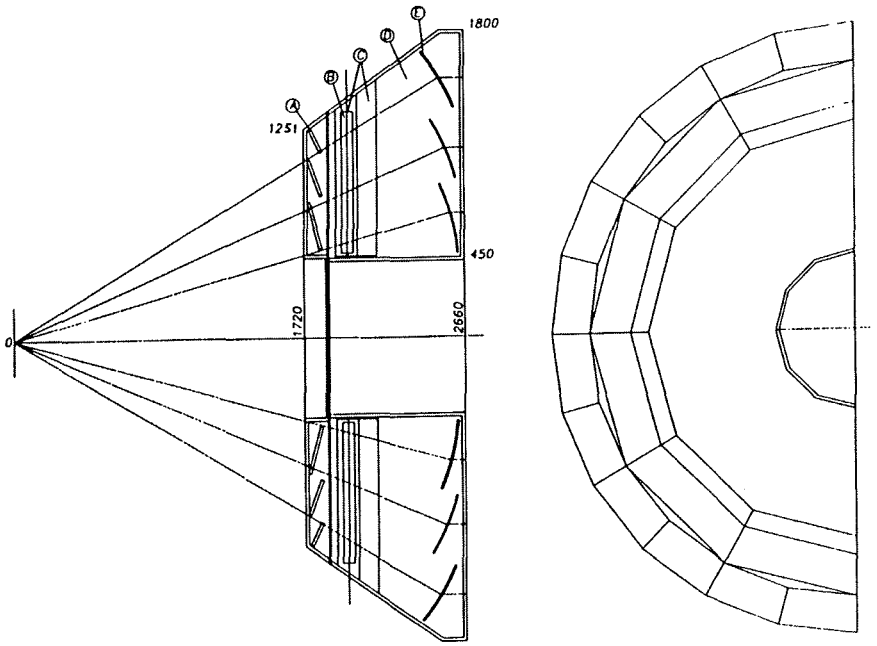

Figure 3.9: Layout of half an end-cap of the DELPHI Forward RICH : A = liquid radiators, B = driftbox, C = MWPC, D = gas radiator volume, E = mirrors.

3.2.3 The Forward RICH of DELPHI

The design of the Forward RICH is shown in figure 3.9. It is located in the two endcaps of the DELPHI detector and covers an active area of $\sim 8\ m^2$ in the polar angle range $15° < \theta < 35°$ and $145° < \theta < 165°$.
As the BRICH, the Forward RICH (FRICH) combine liquid and gaseous radiators with a single photon detector.
However, the construction of the FRICH is different from that of the BRICH because of the geometry and the crossed $E - B$ fields in the photon detectors : the Forward RICH photoelectron drift occurs in a plane perpendicular to the 1.23 Tesla magnetic field of DELPHI.

Each endcap consists of two truncated half-cones and is divided in azimuth

into 12 modular sectors. Each such sector contains 1 drift tube, 2 MWPC's, 3 liquid radiator containers and 5 mirrors (see fig. 3.10). One FRICH detector is housed in two vessels of 180° in azimuth, each closed by a lid structure carrying the liquid radiator containers.
The FRICH provides a coverage of momenta up to 40 GeV/c.

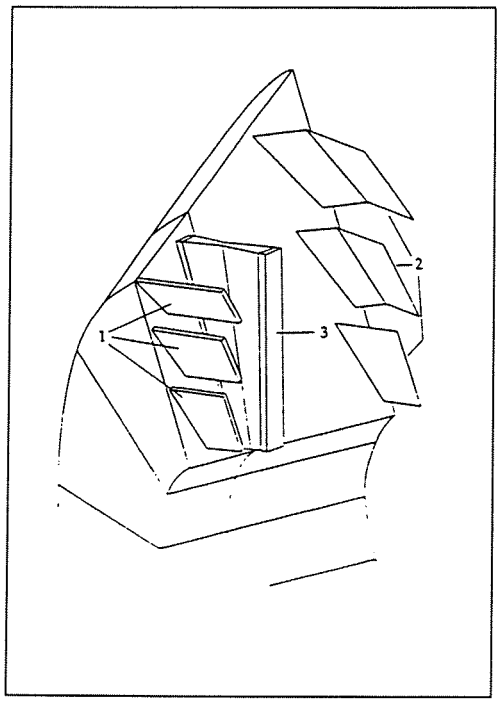

Figure 3.10: Cut-view of the Forward RICH : -1- the 3 liquid radiators, -2- the 5 mirrors and -3- the driftbox.

The Liquid Radiator

The liquid radiator plane consists of 36 discrete containers of 1.0 cm depth filled with C_6F_{14}.
The containers of a 180° segment are arranged as three concentric annuli of 6 containers each. A 30° azimuthal section is thus covered by a triplet of containers.
The Cherenkov photons are directly detected by the photon detector.

The Gas Radiator

The C_4F_{10} (n=1.00155) radiator gas fills all the available space inside the vessel. The number of photons emitted per unit length in the gas radiator is smaller than in the liquid and a longer path inside the gas radiator is therefore necessary.
The average track length inside the gas radiator is about 60 cm.

Spherical mirrors reflect and focus the Cherenkov photons back onto the photon detector.

The Mirrors

The spherical mirrors cover the polar intervals $12° < \theta < 35°$ and $145° < \theta < 168°$ with full coverage in azimuth, except for two 0.1° slices occupied by the side walls of the vessels. They are arranged in three annuli, each with equal polar coverage of 7.67°. In the inner annulus, each mirror covers 30° in azimuth, in the two outer annuli the coverage per mirror is 15°. This gives a total of 120 mirrors for both endcaps.

All mirrors have the same radius of curvature, 120 cm, with the axis pointing towards the intersection point.

The Photon Detector

The photon detection plane is subdivided into trapezoidally shaped TPC units spanning about 30° in azimuth (fig. 3.11). Each drift volume is electrically divided into two symmetrical halves, each read out by a MWPC. The depth of the driftbox is about 5 cm on average. Cherenkov photons arriving at the photon detector convert to photoelectrons in the driftgas C_2H_6 doped with TMAE. Photoelectrons start drifting under the combined action of the orthogonal electric drift field (E_d = 1 kV/cm) and the DELPHI magnetic field (B = 1.23 T), towards the read-out chambers. The direction of motion forms a Lorentz angle with respect to the electric drift field which is about 50°.
The photon conversion length ($\sim$ 2 cm) and the depth of the drift tube are such that a good separation between the photons coming from the liquid radiator and those coming from the gas radiator is possible as they enter into the photon detector from different sides.

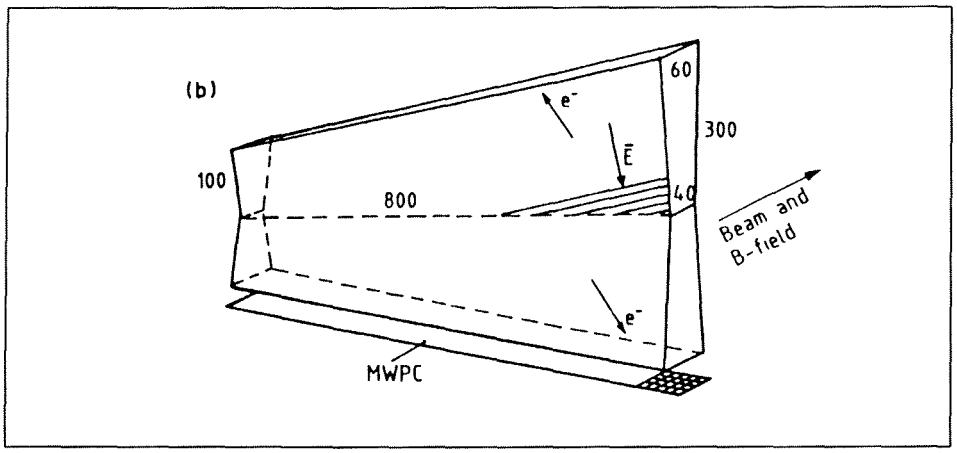

Figure 3.11: Driftbox covering a 30° sector.

The Calibration System

The calibration of the detector is performed by means of UV light from a lamp, distributed by quartz fibres which project light at well defined spots onto the photon detector. This allows the determination of the drift velocity (V_d = 5.1 cm/μs) and Lorentz angle ($\sim$ 50°) which are parameterised as a function of the pressure and temperature of the detector.

3.2.4 Alignment

The identification separation capability of the RICH counters depends crucially on the Cherenkov angle resolution and on the number of detected photoelectrons. In order to obtain the best accuracy, the positions of the different detector elements, the refractive indices of each radiator medium and the photon conversion points have to be precisely determined.
The alignment of the detector elements is based on an offline adjustment of component positions and refractive indices. The RICH software package [9] called ERA performs the alignment of the different subcomponents such as liquid radiator boxes, drift tubes and mirrors following a fit sequence. Selected $Z^0 \rightarrow \mu^+\mu^-$ events (45 GeV/c back to back muons) are used to make this alignment because of their saturated rings in both liquid and gas radiators , the isolation and cleanness of the tracks. The program minimises the difference between the observed (θ_c^{meas}) and calculated (θ_c^{exp}) Cherenkov

angles by varying the relative position of each subcomponent :

$$\chi^2 = \sum_1^N \frac{(\theta_c^{exp} - \theta_c^{meas})^2}{\sigma^2} \tag{3.2}$$

with σ, the expected error and N the number of photoelectrons used in the fit. For each sector of the detector, several parameters are fitted in order to minimise χ^2 for both radiator signals simultaneously.

Finally, the results of the alignment are used to update the positions of the detector elements in the geometry database.

3.3 Performance of the RICH detectors of DELPHI

The DELPHI RICH counters are very powerful in identifying particles, in particular in separating pion (or electron or muon) [2], kaon and proton over a large momentum range.
The momentum range from 0.7 GeV/c to 45 GeV/c is covered by use of gas and liquid radiators (see section 3.2.2).
As an example, figure 3.12 gives the average Cherenkov angle as a function of the particle momentum from real data taken by the Barrel RICH. in 1994. The bands corresponding to pions, kaons and protons in the liquid (a) and in the gas (b) radiators are clearly visible which demonstrates the identification capabilities of the Barrel RICH counter.

The performance and the resolution of the RICHes have been studied and are illustrated by the average Cherenkov angle per saturated ring from $Z^0 \rightarrow \mu^+\mu^-$ events from the 1994 running period. These events provide a clean and well-known sample of muons having a momentum of 45 GeV/c, a saturated Cherenkov angle (of about 60 mrad in the gas radiator of the Barrel RICH) and a maximal number of Cherenkov photons.

The photoelectron Cherenkov angle distributions for $Z^0 \rightarrow \mu^+\mu^-$ events are shown on figure 3.13 for both radiators of the Barrel and the Forward RICH. Fitting these distributions to a Gaussian function gives the Cherenkov angle resolution per photoelectron. Table 3.3 summarises the results [12]. The

[2] pions and muons are practically not separable because their masses are too close. Electrons can only be separated from pions or muons when the Cherenkov angle of the latter is significantly not saturated.

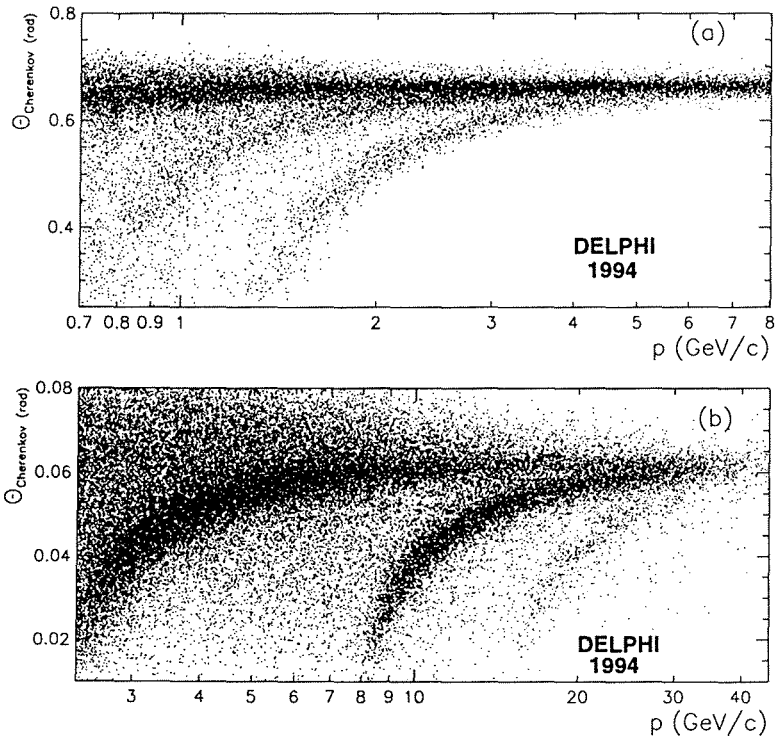

Figure 3.12: Average Cherenkov angle versus particle momentum for 1994 real data for liquid and gas radiators of the Barrel RICH.

procedure to extract the average Cherenkov angle from the RICH 'raw' signals will be discussed in chapter 5 which focuses on the identification of the kaons. The detailed particle identification algorithms are described in [10].

The number of observed photoelectrons (N_{photon}) per track is given by [3] :

$$N_{photon} = N_0 \; L \; \sin^2 \theta_c \tag{3.3}$$

where L is the particle path in the radiator medium in cm, θ_c is the measured Cherenkov angle and N_0 is the so-called *factor of merit* of the detector which is defined by [11] :

$$N_0 = 370 \int \eta(E) \; Q(E) \; R(E) \; T(E) \; dE \; (cm^{-1}) \tag{3.4}$$

	B. liquid	B. gas	F. liquid	F. gas
Cherenkov angle, mrad	666	62.3	675	55.0
Cherenkov angle precision per photoelectron, mrad	13.3	4.3	11.4	2.5
Cherenkov angle precision per track, mrad	5.2	1.5	5.0	1.2

Table 3.2: Cherenkov angles and precisions (in mrad) obtained in dimuon events, for the Barrel (B) and the Forward (F) RICH.

$\eta(E)$, $Q(E)$, $R(E)$ and $T(E)$ are the electron detection efficiency, the absolute quantum efficiency for photon conversion, the reflectivity of the mirror and the transmission of the different detector components (radiator gas, quartz windows, drift gas, etc...) respectively.
Table 3.3 presents the results of the *factor of merit* for the DELPHI Barrel and Forward RICH detectors when only the the detector element characteristics are considered. The electron detection efficiency was set to 1 and the velocity of the charged particle is $\beta \approx 1$. In practice, factors like dead

	Barrel RICH		Forward RICH	
	gas	*liquid*	*gas*	*liquid*
N_0	81.6	70.0	89.6	70.0
N_{photon}	11.1	27.5	15.6	27.5
N_{meas}	8	14	8	7

Table 3.3: Factor of merit (N_0), number of observed photoelectrons per track (N_{photon}) and measured number of photoelectrons per track (N_{meas})

space, efficiency of the MWPC, Lorentz angle, reconstruction efficiency of Cherenkov photoelectrons, have to be taken into account. All these factors lead to a loss in the measured number of photoelectrons per track (N_{meas}), see table 3.3.

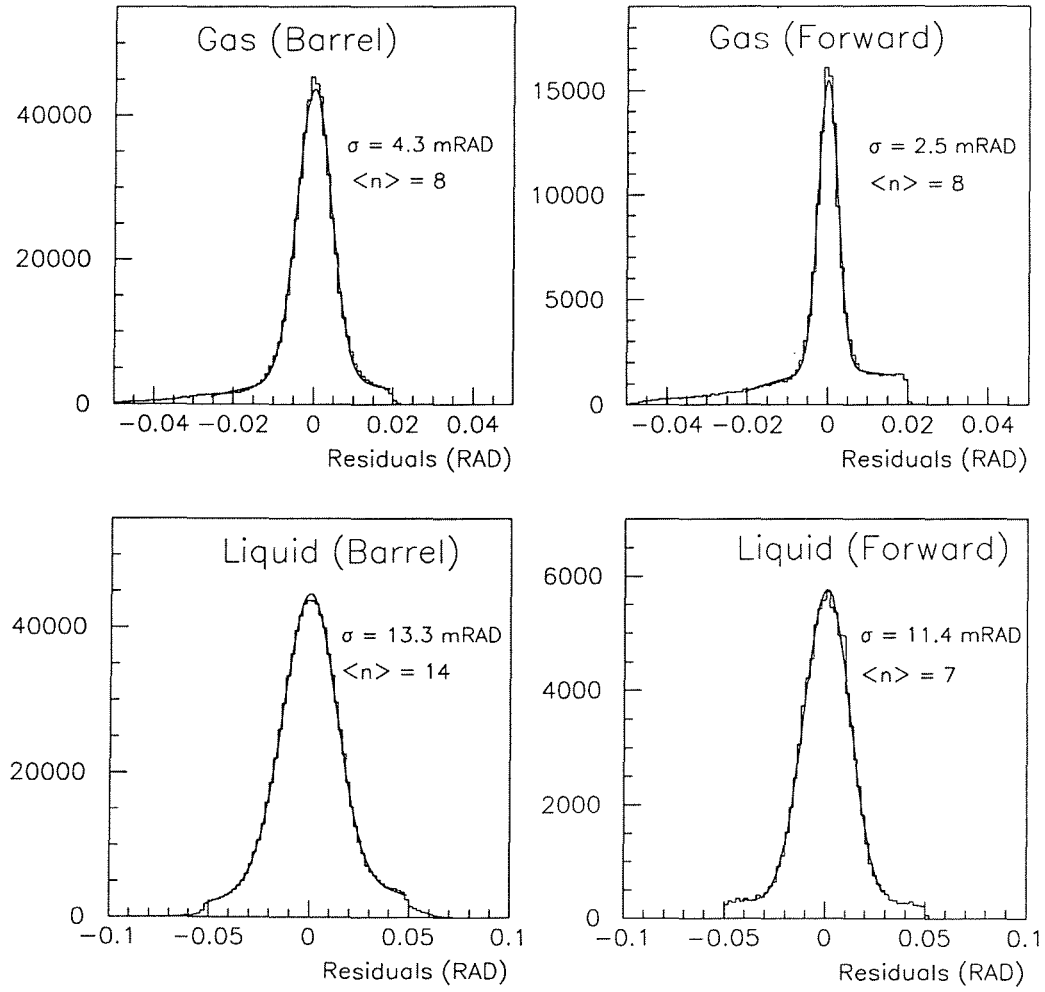

Figure 3.13: Distributions of the photoelecton Cherenkov angles for dimuon events. The average numbers of photoelectrons and the Cherenkov angle measurements precisions for single photons are given for both radiator types, gas and liquid, in both the Barrel and the Forward RICH.

Bibliography

[1] P.A. Cherenkov, *Phys. Rev.* **52** (1937) 378.
P.A. Cherenkov, *Nucl. Instr. and Meth.* **A248** (1986) 1.

[2] I. Frank and I. Tamm, *DOkl. Akad. Nauk SSSR*, **14** (1938) 107.

[3] T. Ekelof, "The experimental method of Ring-Imaging Cherenkov (RICH) counters", DELPHI report 85-11 RICH 5.

[4] J. Seguinot and T. Ypsilantis, *Nucl. Instr. and Meth.* **142** (1977) 377.

[5] R. Arnold et al., *Nucl. Instr. and Meth.* **A270** (1988) 255.

[6] E.G Anassontzis et al., *Nucl. Instr. and Meth.* **A323** (1992) 351.

[7] W. Adam et al., *Nucl. Instr. and Meth.* **A338** (1994) 284 and reference therein.

[8] S. Haider thesis *B_s^0 mixing at the Z^0 resonance determined with the RICH technique.*, Univ. of Leiden (1995).

[9] DELPHI report 89-81 PROG146.

[10] DELPHI report 96-133 RICH 90

[11] DELPHI report 93-112 RICH 58

[12] P. Abreu et al., DELPHI Coll., *Nucl. Instr. and Meth.* **A378** (1996) 57.

Chapter 4

$e^+e^- \rightarrow s\bar{s}$

In this chapter, we make a presentation of the theoretical formalism used to describe the annihilation of electron-positron into a pair of matter fermions, with particular emphasis on cross-section and asymmetry for the process $e^+e^- \rightarrow s\bar{s}$ calculated at tree-level. We show how these experimentally measurable quantities depend on the fundamental parameters of the Standard Model.

4.1 Parameters of the Standard Model

The Standard Model has three independent parameters (not taking into account the Higgs boson mass (M_{Higgs}), the fermions masses and the quark mixing parameters) which are not predicted by the Model but can be experimentally measured with great precision. A particular useful set of parameters is [1]:

- The fine structure constant :

$$\alpha = e^2/4\pi = 1/137.0359895(61)$$

- The Fermi constant :

$$G_F = 1.16639(2) \times 10^{-5}\ \text{GeV}^{-2}$$

  determined from the precise measurement of the muon lifetime.

- The electroweak mixing angle θ_w given by :

$$\sin^2\theta_w = 0.2315(4)$$

  as determined from the Z mass and other Z-pole observables, the W mass, and neutral-current processes.

At lowest order (on-shell scheme), the Z^0 and $W^{\pm}$ masses are predicted in the Model as functions of these measured parameters. We have :

$$M_{W^{\pm}}^2 = \frac{\pi\alpha}{\sqrt{2}G_F \sin^2\theta_w}$$

$$M_{Z^0}^2 = \frac{M_{W^{\pm}}^2}{\cos^2\theta_w} = \frac{\pi\alpha}{\sqrt{2}G_F \sin^2\theta_w \cos^2\theta_w}$$

4.2 General form of the cross-section

In chapter 1, we have defined the different basic parameters contained in the Standard Model of the electroweak interactions through the Lagrangian formalism. We have seen that the interaction between matter fields ψ_i is described by the interaction Lagrangian which adds to the free Lagrangian density :

$$\mathcal{L} = \mathcal{L}_{free} + \mathcal{L}_{int}$$

Corresponding to this, the complete Hamiltonian H of the system is split into the free-field Hamiltonian (H_{free}) and the interaction Hamiltonian (H_{int}) :

$$H = H_{free} + H_{int}$$

The Hamiltonian density $\mathcal{H}(x)$ ($H = \int \mathcal{H}(x)d^3x$) can be found from the Lagrangian density :

$$\mathcal{H} = (\frac{\partial\mathcal{L}}{\partial\dot{\psi}})\dot{\psi} - \mathcal{L}$$

For the case that $\mathcal{L}_{int}$ does not include any time derivatives, then :

$$\mathcal{H}_{int} = -\mathcal{L}_{int}$$

A short description of the general procedure to obtain the expression of the cross-section is developed here (for more details, see [2] and [3]).

Let us first consider the general case of a scattering process in which two fermions, with four-momenta $p_i = (E_i, \vec{p}_i)$, $i = 1, 2$ collide and produce N final state particles with momenta $p'_f = (E'_f, \vec{p'}_f)$, $f = 1, ..., N$. Initial and final particles are assumed to be in definite polarisation states.

From the equation of motion[1] :

$$i\frac{d}{dt} \mid \psi(t) >= H_{int}(t) \mid \psi(t) >$$

with initial condition : $\mid i >$ at time t_0, replacing $\mid \psi(t) >$ by $U(t,t_0) \mid i >$, we get :

$$i\frac{d}{dt}U(t,t_0) = H_{int}(t)U(t,t_0)$$

in which $U(t,t_0)$ is the evolution operator.

The solution of this equation can be written as (Neumann-Liouville development) :

$$U(t,t_0) = 1 + \sum_{n=1}^{\infty} \frac{(-i)^n}{n!} \int_{t_1} dt_1 \int_{t_2} dt_2 \ ... \ \int_{t_n} dt_n \ T\{H_{int}(t_1)H_{int}(t_2) \ ... \ H_{int}(t_n)\} \tag{4.1}$$

where $T\{...\}$ is the so-called time-ordered product or T-product. [2]

The probability amplitude for a transition from the initial state $\mid i >$ (at time $t_0 = -\infty$) to the final state $\mid f >$ (at time $t = +\infty$) ($\mid i >$ and $\mid f >$ being eigenstates of H_{free}) is given by the element S_{fi} of the diffusion matrix :

$$S_{fi} =< f \mid S \mid i >$$

with S defined as :

$$S = \lim_{t_0 \to -\infty, t \to +\infty} U(t,t_0)$$

[1] From now, we will work in natural units, hence $\hbar = c = 1$. In such natural units, all quantities have the dimensions of a power of the mass. The masses being frequently interpreted as an energy and measured in MeV, we have the conservation factors : $\hbar = 6.68 \times 10^{-22}$ $MeV.sec$ and $\hbar c = 1.973 \times 10^{-11}$ $MeV.cm$

[2] The T-product is defined by :

$$T\{\phi(x)\phi(x')\} = \theta(t-t')\phi(x)\phi(x') \ + \ \theta(t'-t)\phi(x')\phi(x)$$

using the step-function :

$$\theta(t) = \begin{cases} 1 & \text{if } t > 0, \\ 0 & \text{if } t < 0. \end{cases}$$

Writing 4.1 in terms of the interaction Hamiltonian density $\mathcal{H}_{int}(x)$, we obtain the so-called Dyson expansion of the S-matrix :

$$S = 1 + \sum_{n=1}^{\infty} \frac{(-i)^n}{n!} \int ... \int d^4x_1 ... d^4x_n T\{\mathcal{H}_{int}(x_1) ... \mathcal{H}_{int}(x_n)\} \tag{4.2}$$

each integration being over all space-time.

The Hamiltonian density $\mathcal{H}_{int}(x)$ involves interacting fields, each linear in creation and absorption operators. In the prospect of using expansion 4.2 to determine the cross-section relative to a given process, calculations are greatly simplified by writing each term of the S-matrix expansion as a sum of normal products[3] (Wick Theorem) and taking into account that in the resulting sum, only one normal product corresponds to the desired process : the one which contains just the right absorption operators to destroy the particles present in $\mid i >$, and which contains the right creation operators to emit the particles present in $\mid f >$. In fact, the expansion 4.2 can be used to describe a large number of different processes, each term of order n of the expansion corresponding to processes represented by Feynman diagrams[4] of order n (n interaction vertices) with creation and absorption of particles which are only present in intermediate states and are so-called virtual particles.

To obtain from the S-matrix expansion 4.2 the transition amplitude $S_{fi} =< f \mid S \mid i >$, which contributes to the determination of the cross-section of the process under study, is a complex problem. This goes out of the frame of our thesis. The reader will find the complete treatment of the problem in [2].

Let us show now how to derive from S_{fi} the experimentally observable quantity, i.e. the cross-section.

For the transition $\mid i > \rightarrow \mid f >$ where the initial and final states are specified by the momenta (and spin and polarisation variables) of the particles

[3] in which all annihilation operators appear to the right of the creation operators.

[4] Feynman diagrams are pictorial representations of interactions between quantized fields.

present, the S-matrix element can be written as :

$$\begin{aligned} S_{fi} =& \delta_{fi} + (2\pi)^4 \, \delta^4(p'_f - p_i) \prod_i \left(\frac{1}{2VE_i}\right)^{1/2} \\ & \times \prod_f \left(\frac{1}{2VE'_f}\right)^{1/2} \prod_l (2m_l)^{1/2} \, \mathcal{M}_{fi} \end{aligned} \tag{4.3}$$

- δ_{fi} describes the absence of interaction ($f = i$).
- $\delta^4(p'_f - p_i)$ is the Dirac delta function[5] which states for the conservation of energy and momentum.
- m_l stands for the mass of the leptons.
- $\mathcal{M}_{fi}$ is the element of the so-called Feynman amplitude matrix :

$$\mathcal{M}_{fi} = \sum_n \text{n}^{th}\text{-order terms}$$

  the sum going over the successive nth-order Feynman graph (for n vertices).

- E_i and E_f are energies.
- V is an arbitrary finite volume in which the whole system is supposed to be enclosed.

The cross-section is, by definition, the transition probability per unit time and per unit incident flux.

This transition probability per unit time is given by :

$$\Gamma = \frac{\mid S_{fi} \mid^2}{T}$$

And the corresponding elementary cross-section is then :

$$d\sigma = \frac{d\Gamma}{F} \tag{4.4}$$

[5]defined by the property that for any function G :

$$\int_a^b \delta(x-c)G(x)dx = \begin{cases} 0 & \text{if } c \notin [a,b], \\ G(c) & \text{if } c \in [a,b]. \end{cases}$$

where $d\Gamma$ is the experimental probability rate and F is the incident flux density :

$$\begin{aligned} F &= \text{Number of incident particles per unit volume} \\ &\quad \times \text{relative velocity of the colliding particles} \\ &= \frac{1}{V} \times v_{12} \end{aligned} \tag{4.5}$$

with $v_{12} = \mid \vec{v_1} - \vec{v_2} \mid$.

Combining these results we obtain the expression of the elementary cross-section :

$$\begin{aligned} d\sigma &= \Gamma \frac{V}{v_{12}} \prod_f \left(V \frac{d^3\vec{p_f'}}{(2\pi)^3} \right) \\ &= (2\pi)^4 \, \delta^4(p_f' - p_i) \, \frac{1}{4E_1E_2v_{12}} \left(\prod_l (2m_l) \right) \left(\prod_f \frac{d^3\vec{p_f'}}{(2\pi)^3 2E_f'} \right) \mid \mathcal{M}_{fi} \mid^2 \end{aligned} \tag{4.6}$$

Let us notice that because of the relativistic invariance of the expression $\{\sigma v_{12} E_1 E_2\}$ and of the phase space element $\{\delta^4(p_f' - p_i) \frac{d^3p_1'}{E_1} \ldots \frac{d^3p_N'}{E_N}\}$ for any four-vector $p' = (E', \vec{p'})$, the Feynman amplitude matrix $\mathcal{M}_{fi}$ is also a relativistic invariant.

In the centre-of-mass system ($\vec{p_1} = -\vec{p_2}$), the relative velocity v_{12} is given by the expression :

$$v_{12} = \frac{\mid \vec{p_1} \mid}{E_1} + \frac{\mid \vec{p_2} \mid}{E_2} = \mid \vec{p_1} \mid \frac{E_1 + E_2}{E_1 E_2} \tag{4.7}$$

with $E_1 + E_2 = \sqrt{s}$, the available energy in the centre-of-mass.
The final-state momenta are constrained by the conservation of energy and momentum. In order to obtain a differential cross-section in the independent variables appropriate to a given situation, we integrate equation 4.6 by making use of δ^4.

We can illustrate this for the frequently occurring case (our case) of a process leading to a two-body final state ($N = 2$). Equation 4.6 becomes :

$$d\sigma = f(p_1', p_2') \, \delta^4(p_1' + p_2' - p_1 - p_2) \, d^3\vec{p_1'} \, d^3\vec{p_2'} \tag{4.8}$$

where

$$f(p_1', p_2') \equiv \frac{1}{64\pi^2 v_{12} E_1 E_2 E_1' E_2'} \left(\prod_l (2m_l) \right) \mid \mathcal{M} \mid^2$$

For simplicity, we drop the indices fi in $\mid \mathcal{M}_{fi} \mid^2$.

Integration of equation 4.8 with respect to $\vec{p_2'}$ and $\mid \vec{p_1'} \mid$ gives the differential cross-section in the centre- of-mass system :

$$\left(\frac{d\sigma}{d\Omega_1'}\right) = \frac{1}{64\pi^2 s} \frac{\mid \vec{p_1'} \mid}{\mid \vec{p_1} \mid} \left(\prod_l (2m_l)\right) \mid \mathcal{M} \mid^2 \tag{4.9}$$

$d\Omega$ being the corresponding element of the solid angle.

We see that the differential cross-section can always be expressed in terms of the Feynman amplitude matrix $\mid \mathcal{M} \mid$. In the following section we will see how to write $\mid \mathcal{M} \mid$ for the particular case of the interaction $e^+e^- \rightarrow s\bar{s}$ and therefore obtain the corresponding cross-section.

4.3 Cross-section calculation for $e^+e^- \rightarrow s\bar{s}$

We are now ready to calculate the differential cross-section for the process which we are interested in : $e^+e^- \rightarrow s\bar{s}$ at LEP energies. In the calculation, we will neglect the masses of the initial and final state particles. This is allowed when the centre-of-mass energy of the annihilation is much bigger than the masses of the particles by one or more order of magnitude. This is the case for light quarks u, d and s. Thus we are allowed to use (see equation 4.9) :

$$\frac{d\sigma}{d\Omega} = \frac{\mid \mathcal{M} \mid^2}{64\pi^2 s} \tag{4.10}$$

where $\mathcal{M}$ is the so-called Feynman amplitude, $\sqrt{s}$ is the available energy in the centre-of-mass and $d\Omega$ is an element of solid angle in the centre-of-mass system.

The process under study in this thesis is :

$$e^+(\vec{p_1},\ r_1) \ + \ e^-(\vec{p_2},\ r_2) \longrightarrow \bar{s}(\vec{p_1'},\ s_1') \ + \ s(\vec{p_2'},\ s_2') \tag{4.11}$$

where r_j and s_j' specify the spin of the particle j in initial and final states respectively. The Feynman diagram at tree level ($n = 2$ in 4.2) corresponding to this process is given in figure 4.1.
The Feynman amplitude for this process can be symbolically written as :

$$\mathcal{M} = \mathcal{M}_\gamma + \mathcal{M}_Z$$

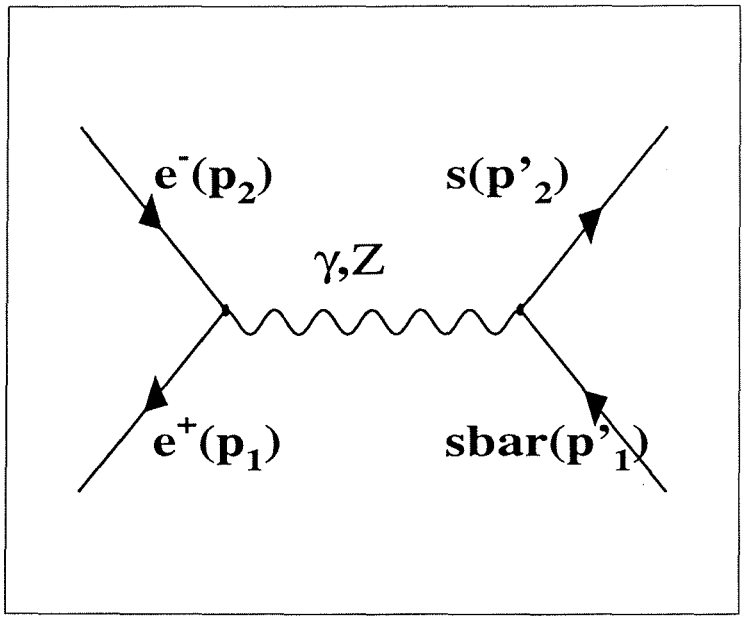

Figure 4.1: The lowest order diagrams for the reaction $e^+e^- \rightarrow s\bar{s}$ via γ and Z^0 exchange.

where $\mathcal{M}_\gamma$ and $\mathcal{M}_Z$ correspond to the processes shown in figure 4.1 through which the reaction 4.11 can occur at lowest order. The Higgs exchange can be neglected because of the small Yukawa coupling to the electron (see section 1.4.3).
Thus $\mid \mathcal{M} \mid^2$ is composed of the following terms :

$$\mid \mathcal{M} \mid^2 = \mid \mathcal{M}_\gamma \mid^2 + \mid \mathcal{M}_Z \mid^2 + 2\ Re(\mathcal{M}_\gamma \mathcal{M}_Z^*) \qquad (4.12)$$

In this process, the spin of the incoming particles (e^+ and e^-) and outgoing particles ($\bar{s}$–quark and s–quark) are not detected.
To obtain the corresponding unpolarised cross-section from equation 4.10, we must average $\mid \mathcal{M} \mid^2$ over all initial spin states, and we must sum it over all final spin states.

Symbolically, the unpolarised cross-section for the process 4.11 is propor-

tional to :

$$X \equiv \frac{1}{4} \sum_{r_1} \sum_{r_2} \sum_{s_1'} \sum_{s_2'} \mid \mathcal{M} \mid^2$$
$$\equiv \frac{1}{4} \sum_{r_1} \sum_{r_2} \sum_{s_1'} \sum_{s_2'} \{\mid \mathcal{M}_\gamma \mid^2 + \mid \mathcal{M}_Z \mid^2 + 2\ Re(\mathcal{M}_\gamma \mathcal{M}_Z^*)\} \quad (4.13)$$

And the differential cross-section 4.10 becomes :

$$\frac{d\sigma}{d\Omega} = \frac{1}{64\pi^2 s} \frac{1}{4} \sum_{spins} \{\mid \mathcal{M}_\gamma \mid^2 + \mid \mathcal{M}_Z \mid^2 + 2\ Re(\mathcal{M}_\gamma \mathcal{M}_Z^*)\}$$

The expressions for the invariant amplitudes $\mathcal{M}_\gamma$ and $\mathcal{M}_Z$ can be written down directly using the Feynman rules [2] with explicit account of the Lagrangian term describing the coupling between matter fields and gauge fields. These will be specified in the following sections.

4.3.1 Invariant Amplitude for the weak interaction

The rules introduced by Feynman to write automatically the amplitude matrix elements ($\mathcal{M}_{fi}$) for the interaction diagram 4.1 corresponding to the weak neutral current (see table 4.1) are :

- for each vertex the factor of the neutral weak current interaction can be written in the form :

$$-i \frac{e}{2 \sin\theta_w \cos\theta_w} \gamma^\mu (v_f - \gamma^5 a_f) \quad (4.14)$$

  with v_f and a_f the vector and axial vector couplings defined in section (1.4.3).

- the massiveness of the mediators (intermediate vector bosons) of weak interactions leads to the following propagator :

$$\frac{-i(g_{\mu\nu} - \frac{q_\mu}{q_\nu})}{q^2 - M^2 + i\Gamma M} \quad (4.15)$$

  where Γ is the resonance width ($\Gamma = \Gamma_{Z^0}$), i.e. the decay constant of the weak boson with mass M ($M = M_{Z^0}$) and q_μ the four-momentum operator.

And the invariant amplitude for the exchange of the Z^0 boson can be consequently written as :

$$\mathcal{M}_Z = \frac{i\ e^2}{4\sin^2\theta_w \cos^2\theta_w}\ (\bar{v}\gamma^\mu(v_f - a_f\gamma^5)u)\frac{1}{s - M_Z^2 + i\Gamma M_Z}(\bar{u}\gamma^\mu(v_f - a_f\gamma^5)v) \tag{4.16}$$

The spinors u and v stand for :

$$u \equiv u_{r_2}(\vec{p_2}) \qquad \bar{u} \equiv \bar{u}_{s_2'}(\vec{p_2'}) \tag{4.17}$$

$$v \equiv v_{s'1}(\vec{p_1'}) \qquad \bar{v} \equiv \bar{v}_{r_1}(\vec{p_1'}) \tag{4.18}$$

which specify completely the momenta and spins of the particles in the initial and final states.

Incoming spin $\frac{1}{2}$ fermion (e^-) and Incoming spin $\frac{1}{2}$ anti-fermion (e^+)		$u_{r_2}(\vec{p_2})$ and $\bar{v}_{r_1}(\vec{p_1'})$
Outgoing spin $\frac{1}{2}$ fermion (s-quark) and Outgoing spin $\frac{1}{2}$ anti-fermion ($\bar{s}$-quark)		$\bar{u}_{s_2'}(\vec{p_2'})$ and $v_{s'1}(\vec{p_1'})$
Z^0 propagator between couplings		$\frac{-i(g_{\mu\nu} - \frac{q_\mu}{q_\nu})}{q^2 - M^2 + i\Gamma M}$
Spin $\frac{1}{2}$ fermion coupling to the Z^0		$-i\ \frac{e}{2\sin\theta_w\cos\theta_w}\ \gamma^\mu(v_f - \gamma^5 a_f)$

Table 4.1 : Feynman rules for the Z^0 diagram of the process $e^+e^- \to s\bar{s}$.

4.3.2 Invariant Amplitude for QED

Following the Feynman rules given in table 4.2, we can directly give the expression of the invariant matrix amplitude for the electromagnetic interaction :

$$\mathcal{M}_\gamma = i\ e^2\ (\bar{v}\gamma^\mu Q\ u)\frac{1}{s}(\bar{u}\gamma^\mu Q\ v) \tag{4.19}$$

where Q is the particle charge in units of e ($Q_e = -1$ and $Q_s = -1/3$).

Photon (γ) propagator between couplings		$\frac{-ig_{\mu\nu}}{q^2}$
Spin $\frac{1}{2}$ fermion coupling to the photon (γ)		$-i\ e\ \gamma^\mu Q$

Table 4.2 : Feynman rules for the photon exchange in the process $e^+e^- \to s\bar{s}$.

4.3.3 From the Cross-Section to the Asymmetry

Summing over the final spin states and averaging over the initial spin states leads to calculate expression 4.13 in the form of a trace and to replace the spinors by appropriate projection operators. The cross-section for the process $e^+e^- \to s\bar{s}$ can now be written down. A long but straightforward calculation gives the differential cross-section for the collision of unpolarised incident beams as a function of the angle θ :

$$\frac{d\sigma}{d\Omega} = C_1(s)(1+\cos^2\theta) \ + \ C_2(s)\cos\theta \tag{4.20}$$

In this equation, θ is defined as the angle between the incoming e^- and the outgoing s–quark directions (centre-of-mass system).
The functions $C_1(s)$ and $C_2(s)$ are given by :

$$\begin{aligned} C_1(s) =& \frac{\alpha^2}{4s}\{Q_f^2 + v_e v_f Q_f \frac{M_Z^2}{s-M_Z^2}\left(\frac{sG}{\alpha}\right) \\ &+ \frac{(v_e^2+a_e^2)(v_f^2+a_f^2)}{8\pi^2}\left(\frac{M_Z^2}{s-M_Z^2}\right)^2\left(\frac{sG}{\alpha}\right)^2\} \end{aligned} \tag{4.21}$$

$$\begin{aligned} C_2(s) =& \frac{\alpha^2}{4s}\{\frac{\sqrt{2}}{\pi}a_e a_f Q_f \frac{M_Z^2}{s-M_Z^2}\left(\frac{sG}{\alpha}\right) \\ &+ \frac{(a_e v_e)(a_f v_f)}{\pi^2}\left(\frac{M_Z^2}{s-M_Z^2}\right)^2\left(\frac{sG}{\alpha}\right)^2\} \end{aligned} \tag{4.22}$$

where f stands for the fermion type in $e^+e^- \to f\bar{f}$ which is a s–quark in our case, G is the Fermi coupling constant and α the fine structure constant.

At relatively low energy ($s \ll M_Z^2$ and thus $\frac{sG}{\alpha} \ll 1$), the terms in equation 4.20 arising from $\mathcal{M}_Z$ can be neglected and the pure electromagnetic cross-section dominates :

$$\frac{d\sigma}{d\Omega} = \frac{\alpha^2}{16E^2}(1 + \cos^2\theta)$$

This is, of course, symmetric in $\cos\theta$.
For intermediate energies, there is a small, but measurable, effect from the electromagnetic-weak interference term $Re(\mathcal{M}_\gamma \mathcal{M}_Z^*)$.
At the Z^0 pole ($\sqrt{s} = M_Z$), the cross-section 4.20 for $e^+e^- \to Z^0 \to s\bar{s}$ becomes large and contains a term in $\cos\theta$ (see expression 4.23) which displays the so-called forward-backward asymmetry : matter and anti-matter do not behave in a spatially symmetric way.

4.4 The forward-backward Asymmetry

The forward-backward asymmetry A_{FB} in $e^+e^- \to f\bar{f}$ (where f is a fermion : the s-quark here) is one of the most important observable quantities since it is sensitive to the weak mixing angle (θ_w) which is a prediction of the minimal model after M_Z is known.

A_{FB} can be determined by studying the angular dependence of the differential cross-section for the production of a fermion pair $f\bar{f}$ (f = lepton, quark), which in the Born approximation is given by :

$$\frac{d\sigma}{d\cos\theta} = \sigma^{tot}\{\frac{3}{8}(1 + \cos^2\theta) + A_{FB}(s)\cos\theta\} \tag{4.23}$$

The forward-backward asymmetry is defined by [4]:

$$A_{FB} = \frac{\sigma_F - \sigma_B}{\sigma_F + \sigma_B} \tag{4.24}$$

where $\sigma_{F(B)}$ are the cross-sections in the forward (F) and backward (B) regions respectively :

$$\sigma_{F(B)} = \int_{F(B)} \frac{d\sigma}{d\Omega} d\Omega$$

The forward and backward regions being defined by :

$$F = \{\Omega = (\phi, \theta\}) \mid \theta \in [0°, 90°]\}$$
$$B = \{\Omega = (\phi, \theta\}) \mid \theta \in [90°, 180°]\}$$

At the Z^0 peak ($s = M_Z^2$), for light fermions ($m_f/M_Z \ll 1$), the asymmetry for the process $e^+e^- \to s\bar{s}$ at lowest order simplifies to :

$$A_{FB}^0(M_Z^2) = \frac{3}{4}\mathcal{A}_e\mathcal{A}_s \tag{4.25}$$

with :

$$\begin{aligned} \mathcal{A}_s &= \frac{2v_s a_s}{v_s^2 + a_s^2} = \frac{2(1 - 4 \mid Q_s \mid \sin^2\theta_w)}{1 + (1 - 4 \mid Q_s \mid \sin^2\theta_w)^2} \\ \mathcal{A}_e &= \mathcal{A}_s(s \to e) \end{aligned} \tag{4.26}$$

From this expression, we can see that the forward-backward asymmetry is a direct measurement of the parity violation in the coupling of the electrons and the quarks to the massive Z^0 boson.
Let us remember that the mixing angle is always to be understood as :

$$\sin^2\theta_w = 1 - \frac{M_W^2}{M_Z^2}$$

It is interesting to notice that the correction to the asymmetry 4.25 in the case of massive fermions is, for the case of the b-quark of the order of $\mathcal{O}(10^{-4})$, and lower for the other fermions [4].

Expression 4.26 shows that the forward-backward asymmetry can be expressed with the unmixed original quantum numbers, the charge and the third component of the weak isospin. The asymmetry stays dependent only on the quantum numbers, the mixing parameter, the mass and the width of the Z^0 boson and the centre-of-mass energy. Figure 4.2 shows the behaviour of A_{FB} as a function the weak mixing parameter $\sin^2\theta_w$ and the centre-of-mass energy $\sqrt{s}$. The distributions are calculated with $M_Z = 91.1863 \pm 0.0020$ GeV and $\Gamma_Z = 2.4946 \pm 0.0027$ GeV [1].

Taking into account higher order contributions, the forward-backward asymmetry has to be written as :

$$A_{FB} = A_{FB}^0 + \Delta A_{FB}^{RC} \tag{4.27}$$

where the radiative correction term ΔA_{FB}^{RC} is generated by the loop diagrams contributing to the elastic cross-section and the real photon bremsstrahlung emission as an inclusive inelastic process. ΔA_{FB}^{RC} depends on all parameters of the model.

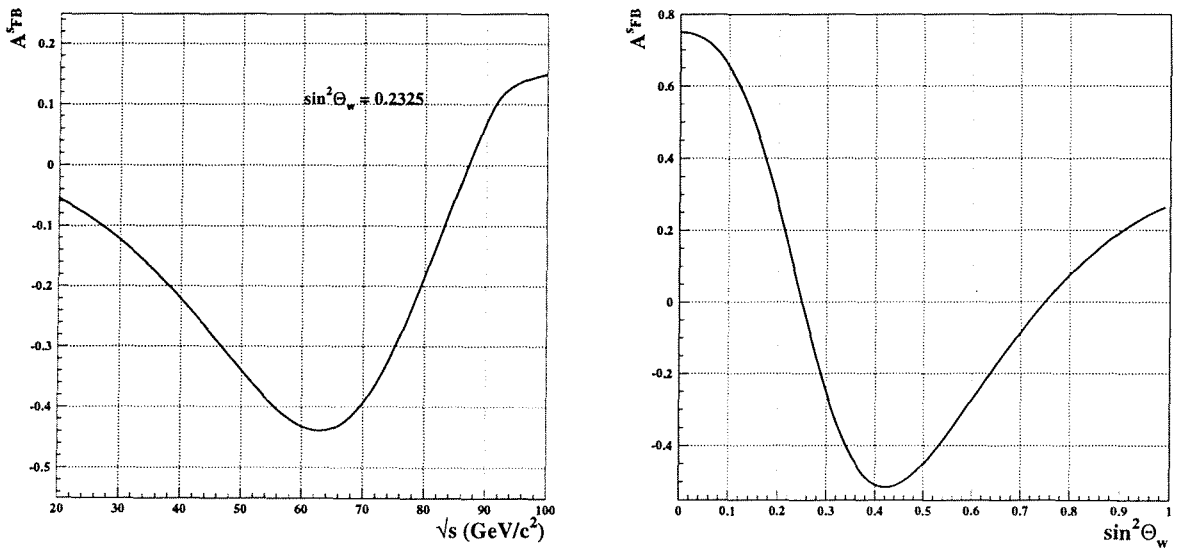

Figure 4.2: Distributions of the forward-backward asymmetry of the s-quark (a) as a function of the centre-of-mass energy $\sqrt{s}$ (with $\sin^2\theta_w$ set to 0.2325) and (b) as a function of weak mixing parameter $\sin^2\theta_w$ (with $\sqrt{s}$ set to $M_Z = 91.187$ GeV).

In the improved Born approximation, the higher order radiative corrections can be taken into account by substituting in equations 4.26 the effective couplings $\bar{v}_f$ and $\bar{a}_f$. In this way, an effective Weinberg mixing angle θ^f_{eff} is defined as :

$$\sin^2\theta^f_{eff} = \frac{1}{4 \mid Q_f \mid}\left(1 - \frac{\bar{v}_f}{\bar{a}_f}\right) \tag{4.28}$$

where Q_f is the fermion electric charge.
Therefore the measurement of the forward-backward asymmetry of fermions allows a measurement of $\sin^2\theta^f_{eff}$ and an accurate test of the Standard Model. From equations 4.25 and 4.28, we can deduce that the down-type quarks are the most sensitive to $\sin\theta^f_{eff}$ variations ($\mid \Delta \sin\theta^f_{eff}/\Delta A^{d-type}_{FB} \mid \simeq 1/6$). Moreover, the difference $A^{b\bar{b}}_{FB} - As\bar{s}_{FB}$ is of the order of $\mathcal{O}(10^{-4})$ which is (as we will see) beyond the present experimental accuracy. Thus the measurement of the $s\bar{s}$ asymmetry can be considered as a test of the universality of the couplings.

Bibliography

[1] Theory Review of Particles Physics, *Phys. Rev.* **D 54** (1996) 1.

[2] F. Mandl : *Quantum Field Theory*, ed. J. Wiley, 1993.

[3] P. Renton : *Electroweak Interactions*, ed. Cambridge University Press, 1990.

[4] CERN yellow Report : *Z physics at LEP*, CERN 89-08 (Vol. 1), 1989.

[5] CERN Report : CERN-PPE/96-183, 1996.

[6] DELPHI Collaboration, *Phys. Lett.* **B276** (1992) 536.

[7] DELPHI report : DELPHI 95-87 PHYS 522. and references therein.

[8] P.Abreu et al.: *Z. Phys.* **C 67** (1995) 1-13.

Chapter 5

Experimental procedures relevant for the analysis

In this chapter, we start on the description of the experimental techniques that we have exploited to measure the forward-backward asymmetry of the strange quark. In the first section, we explain how the Brown and Frank algorithm is applied in DELPHI to separate light quark events from events coming from the decay of b-quarks. In the second section, we discuss the identification of the charged particles using the Cherenkov detectors, charged particles which are used to tag strange flavour events.
Let us notice that these procedures were settled by people who are the experts in the fields. We have checked with satisfaction the consistency of their results and we propose to give here a concise overview of the methods. For more details we send the reader to the corresponding references.

5.1 Selection and rejection of heavy quark events

The main difficulties in the experimental determination of the strange quark asymmetry are, like for other quark asymmetries, a reliable identification of the jet flavour. A specific difficulty in the case of the s-quark as compared to the b-quark comes from the fact that the strange particles which are used to tag $s\bar{s}$ events result also from the hadronization of b-quarks. To separate heavy quarks from other flavours, Brown and Frank [1] proposed an algorithm which is based on the following principle : hadrons containing bottom quarks have relatively long lifetimes, of the order of 1.55 ps, and large masses, implying that their decay is characterised by many (5 or 6) decay products with large positive impact parameters with respect to the primary vertex

(coming from well separated secondary vertices).
By using the Vertex Detector (see section 2.2.3) of DELPHI, a precise measurement of the impact parameters of the outgoing tracks of the event with respect to the primary vertex (position in space of the primary Z decay) can be performed.
The complete description of the application of the Brown and Frank algorithm in DELPHI can be found in [2]. It gives the possibility of constructing one tagging variable from all impact parameter values observed in the event.

5.1.1 Definitions

Before treating the problem of the primary vertex reconstruction and the impact parameter determination, quantities which will be frequently used in the following sections must be clearly defined.

• The trajectory of a charged particle in a uniform magnetic field is a helix with its axis parallel to the direction of the magnetic field (the z axis in the DELPHI reference frame given in figure 2.5. To describe this trajectory (and thus to reconstruct the track), different sets of parameters can be used. The parameters used here are the parameters of the perigee P (the point of the track located at the shortest distance from the origin O of the reference frame.)
The parameters are :

- The vector $\vec{d}$, the distance between P and O.

- The vector $\vec{t}$, the tangent to the track trajectory in P. (θ is the polar angle between O_z and $\vec{t}$ and ϕ the azimuthal angle of $\vec{t}$.)

- The track curvature radius : ρ.

Figure 5.1 shows these parameters in the xy plane.

• The hadronization process of quarks and gluons produced in hard collisions (see figure 2.9) leads to secondary particles clustered in the direction of the quark or the gluon. These clusters are called *jets*. The construction of jets in an event is based on a "jet finding algorithm".
The Brown and Frank algorithm applied in DELPHI uses the jet reconstruction algorithm called JADE [3], from the name of the collaboration which adopted it for the first time. The algorithm is an iterative procedure which works as follows : In each hadronic event, the observables

$$y_{ij} = \frac{2E_iE_j\ (1-\cos\theta_{ij})}{E_{vis}^2} \tag{5.1}$$

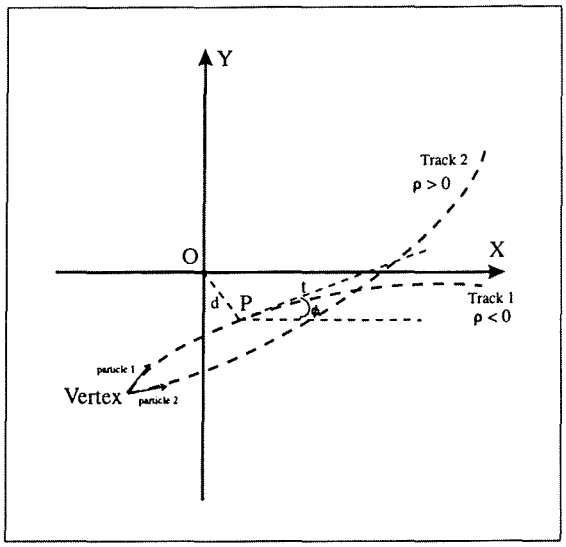

Figure 5.1: Characteristic parameters of the perigee in the plane xy.
Distributions of the number of photoelectrons for the gas radiator

are calculated for all pairs of particles i and j where E_i and E_j are the energies of the particles, θ_{ij} is the angle between the particles and E^2_{vis} is the total visible energy of the event (charged particles being assumed to be pions and neutral particles to be photons). The two particles i and j with the smallest value of y_{ij} are replaced by a pseudo-particle or "cluster" with four-momentum $(p_i + p_j)$. This procedure is repeated until the pair masses of all particles or pseudo-particle pair-combinations exceed a certain threshold value called y_{cut}, and the resulting clusters are called *jets*. For LEP applications, the usual value of y_{cut} is 0.01.

• Another frequently used quantity which measures the "jettyness" of an event is the so-called *thrust* quantity which is defined by :

$$T = \max_{|\vec{n}|=1} \frac{\sum_i \mid \vec{n} \cdot \vec{p_i} \mid}{\sum_i \mid \vec{p_i} \mid} \tag{5.2}$$

$\vec{p_i}$ being the momentum of the i-th particle. The thrust axis is given by the $\vec{n}$ vector for which the maximum is attained. The allowed range is $1/2 \leq T \leq 1$, with 2-jet event corresponding to $T \approx 1$ and an isotropic event to $T \approx 1/2$. Consequently, the thrust axis gives an estimator of the original direction of the primary quark before emission of gluons and is used like that in our analysis.

5.1.2 Primary vertex reconstruction

For every hadronic event, the primary vertex is reconstructed using the *beam spot* position as a constraint in a least squares fit procedure. The *beam spot* is defined as the position of the interaction point of the electron and positron beams. The beam spot position can vary in time and is averaged for every 200 hadronic events. For these events, a vertex, origin common to all tracks of an event which have at least 2 hits in the Vertex Detector (to ensure a good tracking reconstruction), is calculated.
The principle of the least squares procedure is to find the vertex as close as possible to the tracks while being in the interaction region and the χ^2 function is [4] :

$$\chi^2(V_i) = \sum_j \frac{d_j^2}{\sigma_j^2} + \sum_{i=x,y,z} \frac{(b_i - V_i)^2}{(\sigma_i^b)^2} \tag{5.3}$$

where d_j is the distance of the track j to the reconstructed vertex, σ_j is the corresponding error, V_i is the position of the primary vertex and b_i,σ_i^b, are the beam spot position and size[1].
The minimisation procedure is carried out iteratively, excluding after each iteration the track with the largest χ^2 contribution $\Delta\chi^2 = \chi^2(N_{track}) - \chi^2(N_{track} - 1)$ if it exceeds a maximum value $\Delta\chi^2_{max}$. This procedure is repeated until no change above threshold occurs.
Since the beam-spot is used as a starting reference point, all tracks can in principle be rejected from the fit. The fraction of such events is around 1% and for these events, the position and dimension of the beam-spot are taken as the determination of the primary vertex and the error on it.
The main advantage of this method of fitting is the quadratic dependence of the χ^2 function (5.3) on the fitted values. It gives the possibility of analytical and straightforward determination of the vertex position V_i. Figure 5.2 shows the difference between the reconstructed and generated vertex position in a simulated DELPHI event sample in the x and z direction for light quark events and for bottom quark events. The resolution is about 22 μm in the x and z directions for light quark events and 35 μm for bottom quark events. The distributions for bottom quark events show non-Gaussian tails due to tracks coming from secondary vertices (decay of B hadrons) and not from the primary vertex.

[1]The width of the beam spot is of 100 to 120 μm along the x coordinate and 8-10 μm along y. The typical uncertainties on the x and y positions are of about 9 μm and 4 μm respectively. The precision on the beam spot position determination and its small dimensions improve the accuracy of the event by event primary vertex position reconstruction.

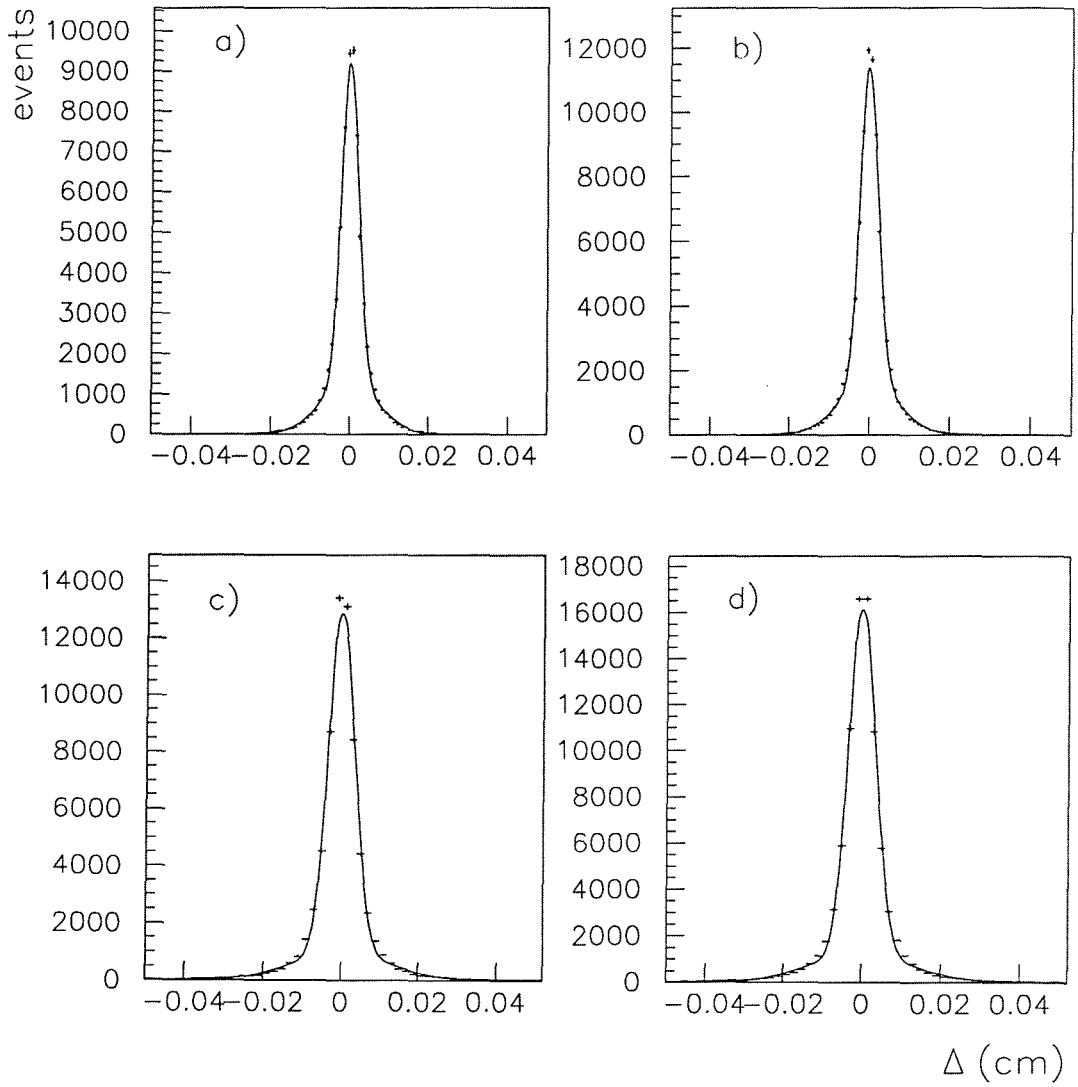

Figure 5.2: Difference (Δ) between the reconstructed and generated vertex position in a simulated event sample (a) x-coordinate for light quarks, (c) x-coordinate for b quarks, (b) z-coordinate for light quarks and (d) z-coordinate for b quarks. The full line show the fits to the data with a sum of two Gaussians.

5.1.3 Impact parameter precision

In the Brown and Frank algorithm, the quantity effectively used is the so-called *significance* of a track. It is defined as the ratio of the track impact parameter with respect to the primary vertex (δ) to the impact parameter error (function of $\sigma_{r\phi}$ and σ_z).
The impact parameter of a track is defined as the minimum distance between the track trajectory and the reconstructed primary vertex. The sign of this impact parameter is defined with respect to the direction of the jet to which the track belongs : it is **positive** if the vector joining the primary vertex to the point of closest approach of the track makes an angle **less than 90°** with the direction of the jet (see figure 5.3).
With such a definition, tracks from the decays of B hadrons have positive

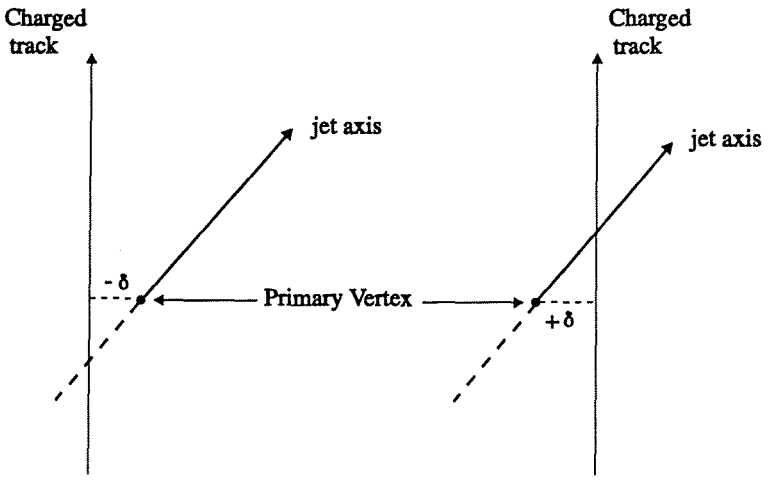

Figure 5.3: Definition of the sign of the impact parameter δ.

impact parameters, whereas non-zero impact parameters arising from inaccurate reconstruction of particle trajectories are equally likely to be positive or negative.
The impact parameter and its error are due to the track extrapolation error on the point of closest approach and the error on the primary vertex. The measurement contribution to the track extrapolation error at the interaction point can be estimated from the apparent distance between the reconstructed tracks from $Z \rightarrow \mu^+\mu^-$ decays (assuming their energy to be the energy of the beams), where multiple scattering and vertex contributions are negligible. As it can be deduced from the 28 μm width of the distribution of this distance projected onto the $r\phi$ plane (see figure 5.4, upper), the track extrapolation measurement error in the plane $r\phi$ is $\sigma_{r\phi} = 20$ μm. In the rz

plane, this error which is a function of the angle θ (see figure 5.4, lower), is $\sigma_z = 34$ μm for tracks perpendicular to the Vertex Detector. For tracks with

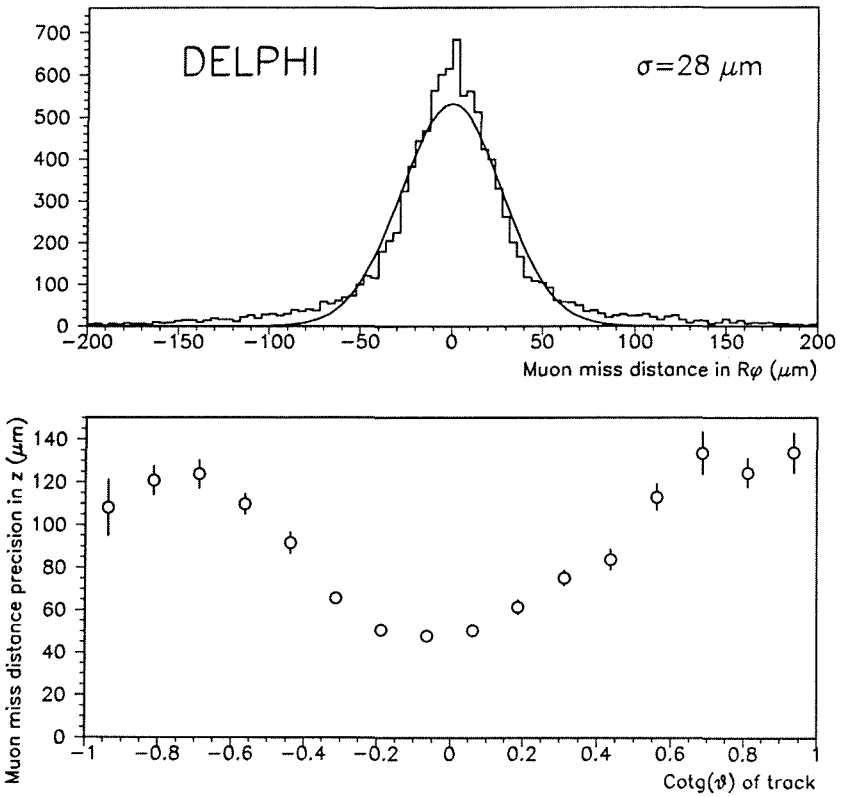

Figure 5.4: Upper plot : miss distance between two muons in the $r\phi$ plane for $Z \rightarrow \mu^+\mu^-$ events. The non-Gaussian tails are due to variations in the VD hit precision. Lower plot : miss distance in the rz plane for $Z \rightarrow \mu^+\mu^-$ events, as a function of the polar angle.

lower momentum, the track extrapolation precision can be estimated from the impact parameter distribution of tracks from a sample enriched in light quark events (selected by the Brown and Frank algorithm explained in the next section). In order to avoid biases coming from a residual contribution of heavy quarks, only tracks having a negative impact parameter are used. The

extrapolation errors in the $r\phi$ and rz planes have been parametrised as [1] :

$$\begin{aligned} \sigma^2_{r\phi} &= \left(\frac{\sigma_{MS}}{p\ \sin^{3/2}\theta}\right)^2 + (\sigma_{0,r\phi})^2 \\ \sigma^2_{z} &= \left(\frac{\sigma'_{MS}}{p\ \sin^{5/2}\theta}\right)^2 + (\sigma_{0,z})^2 \end{aligned} \tag{5.4}$$

The first terms describe the contribution of the multiple scattering with material, depending on $1/\sin\theta$ (where θ is the track polar angle) and on the track momentum p. σ_{MS} (σ'_{MS}) is a multiple scattering coefficient (in μm.Gev/c). The second terms take into account the error due to the intrinsic resolution of the tracking system.
Using the impact parameter with negative sign and parametrising the extrapolation uncertainly as above, the following values are obtained : $\sigma_{MS} =$ 65 μm.GeV/c, $\sigma_{0,r\phi} = 20$ μm. The value obtained for the multiple scattering coefficient σ'_{MS} is 71 μm.GeV/c, the measurement error varying from 39 to 96 μm per track for the angle going from 90° to 45°.
An important contribution to the improvement on the impact parameter resolution in the rz plane is the use of the Vertex Detector in this plane : comparing the impact parameter in rz for tracks in the polar angle region $70° \leq \theta \leq 110°$ and with momentum above 6 GeV/c, without and with the z information of the Vertex Detector, an improvement by a factor 20 (from 884 μm to 47 μm) in the rz impact parameter precision, is obtained.

5.1.4 The Brown and Frank algorithm

This algorithm is used to reject bottom and charm quarks and thus to improve the s-quark purity of our sample.
As explain above, it is based on reconstructing as precisely as possible the primary vertex and the impact parameters of the outgoing tracks with respect to that vertex.
Figure 5.5 shows the distribution of the absolute value of the significance (S), defined as the ratio of the impact parameter (δ) and its error (σ_δ), in the $r\phi$ and rz planes for tracks from real data measured in the Vertex Detector with negative (dashed line) and positive (solid line) impact parameters with respect to the primary vertex.
The excess of tracks in the non-Gaussian tail of the distribution of the positive significance is due to tracks coming from the decay of B hadrons. The negative significance distribution is mainly affected by the detector resolution effects and not by secondary decays.

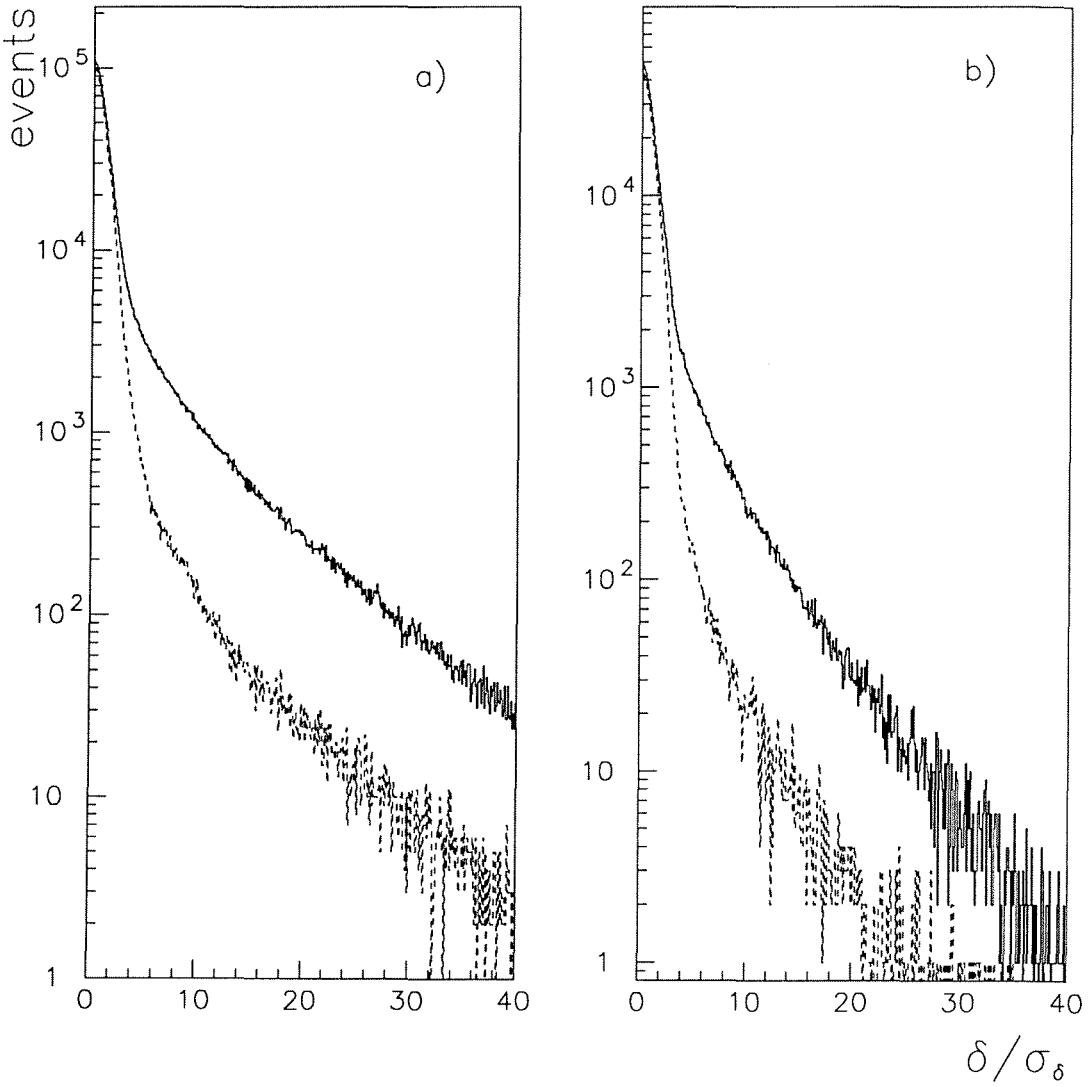

Figure 5.5: Distribution of the absolute value of the significance $S = \delta/\sigma_\delta$ in $r\phi$ (left) and rz (right) for tracks from real data measured in the Vertex Detector with negative (dashed line) and positive (solid line) impact parameters.

The discriminant variable used to reject events coming from the decay of heavy quarks is the probability P_E^+ computed on an event by event basis for all tracks of the event for which the measured significance is positive.
In a general way, the probability that the N tracks of the event come from the primary vertex (P_N) is built using the significance probability density $f(S)$. This function $f(S)$ is obtained from the distribution of tracks with negative impact parameters in a sample of events with reduced B hadron content, mirroring the negative significance S distribution for positive S. P_N is defined as :

$$P_N \equiv \prod \sum_{j=0}^{N-1} (-\log \Pi)^j / j! \text{ , where } \Pi \equiv \prod_{i=1}^{N} P(S_i) \tag{5.5}$$

where i runs on the number of tracks considered, the probability that a single track with $S > S_0$ ($P(S_0)$) comes from the primary vertex being defined by :

$$P(S_0) = \int_{S>S_0} f(S)\, dS \tag{5.6}$$

This probability P_0 defined for each track in the event is thus used to build the probability P_N for a group of N tracks to come from the primary vertex : The group of tracks may be all the tracks of the total event (P_E), or tracks from one hemisphere (defined by the plane perpendicular to the thrust axis) or from one or several reconstructed jets. The proof that the variable P_E^+ behaves as a probability is given in [1]. By construction, the distribution of this probability should be flat for events with all tracks coming from the primary vertex and would be peaked at O for events with if the group of N tracks including tracks coming from secondary vertices (decay vertices of long-lived particles like bottom and charm hadrons, K_s^0, Λ, ...)(see figure 5.6). The positive significance event probability distribution (P_E^+) shows a peak at low values due mainly to the heavy quark contribution and is the only variable used to separate $Z \rightarrow b\bar{b}$ events from light quark events.
On figure 5.7, we show the flavour composition of a sample of hadronic events as a function of P_E^+ (the positive significance event probability). We see that asking the probability P_E^+ to be greater than some well determined value gives an efficient method to reject heavy flavour events. This value will have to be chosen as a good compromise between decreasing as much as possible the bottom and charm contamination and keeping the s-quark tagging efficiency above 80%.

5.2 Identification with the RICHes

Chapter 3 is fully devoted to the description and the technical understanding of the working principles of the Ring Imaging Cherenkov detectors (Barrel and Forward RICH). In this section we discuss concisely how the informations given by the RICH detectors are treated and used to identify charged particles (and in particular, charged kaons).
As described in chapter 2, the DELPHI experiment is equipped with an other detector to identify charged particles : the TPC based on the principle of the energy loss by ionization dE/dx.
In the momentum range useful for our analysis (p greater than 10 GeV/c), this technique is less efficient than the RICH technique and the dE/dx technique is thus not applied. In fact, the π-K separation achieved with the DELPHI TPC at the moment is not greater than 1 or 1.5 standard deviations, with an efficiency lower than 20%, which is not sufficient for a good kaon identification with high purity essential for the kind of measurement done in our analysis (see chapter 6). The major problem is the typical track multiplicity of the event topology which makes difficult a correct calibration of the distribution of the dE/dx by the simulation for the different tracks and consequently a correct determination of the contamination (kaons wrongly identified as pions).

5.2.1 Cherenkov angle reconstruction

Depending on the particle momentum (p), two identification procedures can be distinguished :

- below the Cherenkov threshold ($\beta = 1/n$), we speak about VETO identification. In this case, a particle is identified by the fact that it does not radiate Cherenkov light in the medium of refractive index n.
- above a specific value of p (threshold), Cherenkov radiation is emitted : we speak about RING identification. The charged particle is identified by the specific reconstruction of the Cherenkov ring.

This can be easily understood by looking at figure 3.2 (in chapter 3) : a charged particle having a momentum of 6 GeV/c and which emits photoelectrons in the gas radiator of the Barrel RICH can only be a pion, kaons and protons giving no light in this medium below ~9 GeV/c and ~18 GeV/c, respectively.

Our sample being enriched in $s\bar{s}$ events by using high momentum ($p >$ 10

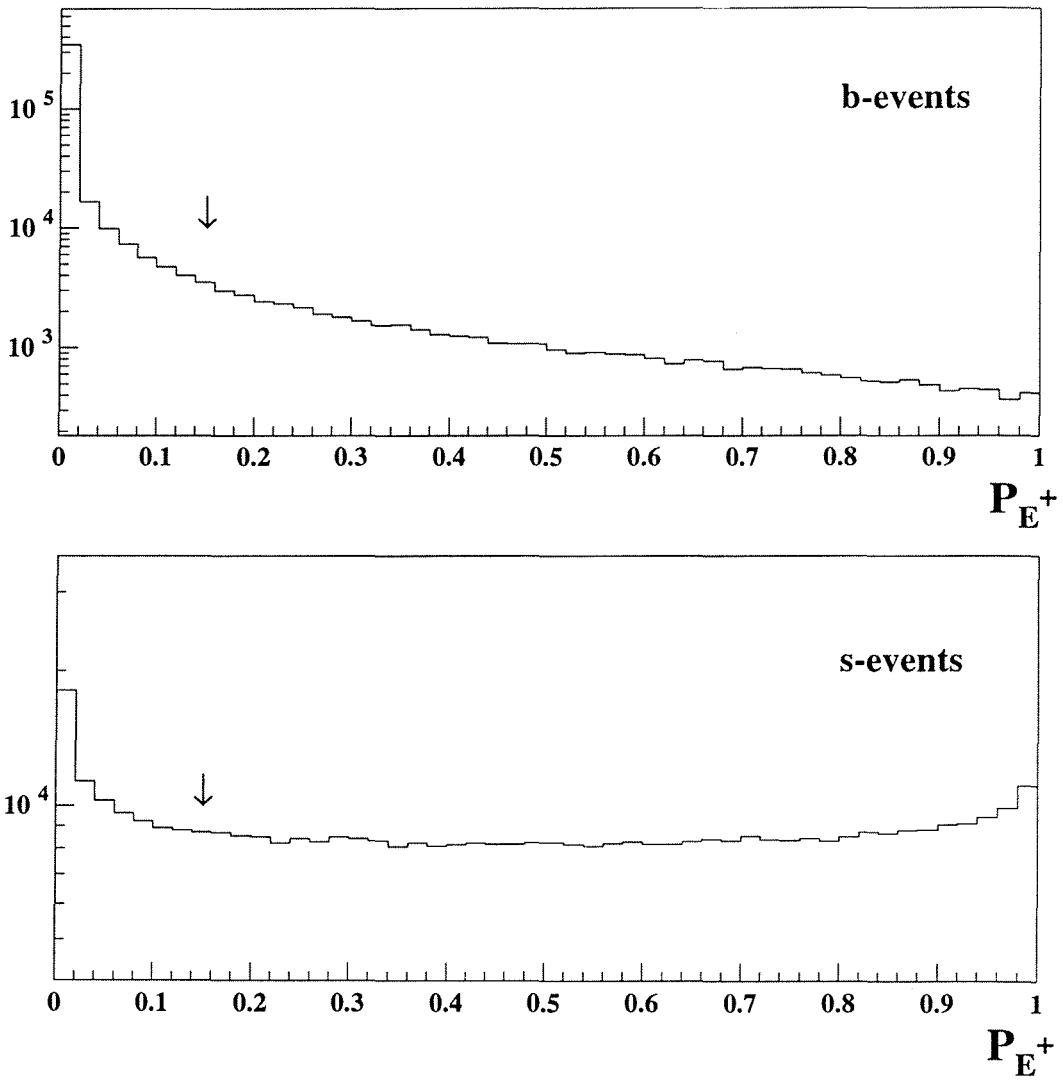

Figure 5.6: Positive Event Probability (as defined in section 5.1.4) for bottom events (top) and strange events (bottom). The arrows show the applied cut.

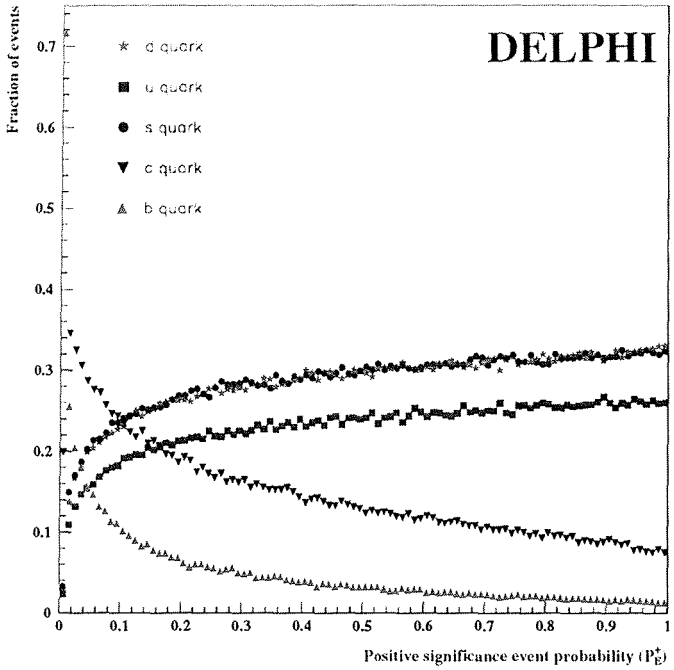

Figure 5.7: Flavour composition of hadronic events as a function of P_E^+ positive significance event probability.

GeV/c) charged kaons, only signals coming from the **gas radiators** of the RICHes have been exploited and the **RING identification** method applied.

The RING identification method is based on two quantities : the measured Cherenkov angle (θ_c) and the observed number of photoelectrons ($N_{p.e}$). According to their definitions :

$$\cos\theta_c = \frac{1}{\beta n}$$

$$N_{p.e} = N_0 \; L \; \sin^2\theta_c$$

(which are fully described in sections 3.1.2 and 3.3, respectively), and knowing the particle momentum, they give information on the particle mass.

Different techniques [5] have been developed to combine the information of the detected Cherenkov photons in order to identify particles.

The one used for our analysis (conventionally referred to as the "RIBMEAN" approach) relies on a weighting and clustering procedure to estimate the number of photoelectrons and to reconstruct the average Cherenkov angle for a given track. It is described in details in [6].
The advantage of this method which is based on the reconstruction of the average Cherenkov angle is that it allows detailed checks of the RICHes. The distributions of the Cherenkov angle and the number of photons for identified particles can be studied and compared to expectations and Monte Carlo simulations. The average Cherenkov angle (and related quantities) has proven to be useful for understanding the RICH response and for adjusting the detector simulation. Moreover, this method has proven to give a high identification purity which is important for our analysis.

It should be noted that a very precise and very detailed technical knowledge of the functioning of the Cherenkov detectors is needed to develop such a method which provides the basic information (a measured Cherenkov angle, its error and the number of detected photoelectrons) allowing the identification of the particles from the raw data provided by the experimental setup. The details of the full procedure are left to experts and go out of the frame our work. In the following we just summarise the different steps of the method which delivered the basic data involved in the physics analysis :

• The starting point of the clustering method is a set of detected single photoelectrons i (which come from the conversion of the Cherenkov photons produced by the track crossing the radiator medium). They are characterised by :

- a Cherenkov angle θ_i, knowing the position of the photoelectron and the crossing point of the track inside the photon detector;

- the error on this Cherenkov angle σ_{θ_i}, which is the quadratic sum over several error sources (like the chromatic aberration, i.e. the variation of the refractive index with the photon energy, the position resolution of the photon detector, the particle trajectory curvature in the magnetic field of DELPHI.);

• First, a weight (w_i) is given to each photoelectron i according to the signal to background ratio. This weight is related to the probability that a photoelectron really comes from the conversion of a Cherenkov photon. This procedure is applied to suppress background photoelectrons : the background in the RICHes is higher for the so-called ambiguous (assigned to more than

one ring) photoelectrons than for non-ambiguous ones, and higher for photoelectrons that have a low conversion probability (determined on the basis of the conversion point inside the drift tube) than for photoelectrons with high conversion probability. Photoelectrons which are isolated have a lower background than the non-isolated ones. The main sources of background are feedback photoelectrons (created during avalanche developed around the anode wires), cross-talk (one signal hits 2 strips), ionization (caused by other tracks crossing the photon detector), overlapping rings. The ambiguous photoelectrons are given a typical weight of 0.5 which is brought to 1 after ambiguities are solved. Figure 5.8 shows the effect of applying weights on the single photoelectron Cherenkov angle distributions : the signal to background ratio is improved.

• In the second step, the photoelectrons are grouped to form clusters, these clusters being ordered iteratively with respect to the five mass hypotheses : electron, muon, pion, kaon and proton, each characterised by an expected Cherenkov angle $\theta_c^{hypo,exp}$. For a given hypothesis, the first cluster is started from the photoelectron which has a Cherenkov angle closest of the expected Cherenkov angle (closest can be more than 2.5 standard deviations ($\sigma_{\theta_c^{hypo,exp}}$)) and any photoelectron which is within a window of 2.5 standard deviations (σ_{θ_c}) around the average angle (θ_c) (this one being recalculated at each step) is grouped with the first one. If no more photoelectron can be added to the first cluster, a second clustering is tried and so on. When all the photoelectrons have been grouped, a second set of clusters is built around the following hypothesis and so on.
This gives five sets of clusters corresponding to the five mass hypotheses.
Among them, the selected set (i.e. the selected hypothesis) is the one which has the largest weighted number of photoelectrons (N_w) in the largest cluster (i.e. which contains the highest number of photoelectrons N), N_w being defined as :

$$N_w = \sum_{i=1,N} w_i$$

For this chosen set of clusters, the measured average Cherenkov angle :

$$\theta_{ring}^{meas} = \frac{1}{N_w} \sum_{i=1,N} w_i \theta_i \tag{5.7}$$

the weighted number of photoelectrons N_w and the expected error per photon :

$$\sigma_{p.e} = \frac{1}{N_w} \sum_{i=1,N} w_i \sigma_{\theta_i} \tag{5.8}$$

are calculated for each cluster.
The cluster with the highest sum of weights is kept and outliers are removed by applying a probability cut of 5%.
We are thus left with a track, its measured average Cherenkov angle, its number of photoelectrons and the expected error per photoelectron. It is in the next stage that ambiguities are treated.

• An ambiguous photoelectron is a photoelectron which could have been associated to several tracks (see figure 5.9). Different cases are possible (figure 5.10) :

(a) The photoelectron is associated to only one selected cluster and thus the ambiguity is directly resolved.

(b) The photoelectron is associated to two or more selected clusters. Then two situations can be distinguished :

- the photoelectron is associated to two (or more) rings formed by tracks producing Cherenkov light in the same radiator medium (conventionally called gas-gas or liquid-liquid ambiguities);

- the photoelectron is associated to two (or more) rings formed by tracks producing Cherenkov light in different radiator media (conventionally called gas-liquid ambiguities).

The latter one is easy to sort out using the conversion depth ("liquid" photoelectrons are absorbed at one side and "gas" photoelectrons at the opposite side of the photon detector). The first one is resolved using the χ^2 contribution of the photoelectron to each track.

• After solving the ambiguous photoelectrons the clustering is redone.

At the end of the procedure described above, for each track, the information available for any physics analysis and which are delivered to us together with the data are thus :

- a measured Cherenkov angle θ_{ring}^{meas};

- a number of photoelectrons N;

- the expected error on this Cherenkov angle σ_{ring}, function of the track momentum (p), the observed number of photons (N) and the error per photon ($\sigma_{p.e}$). This error is parametrised for hadronic events using the complete simulation of the apparatus [6] :

$$\sigma_{ring}^{Barrel} = \sigma_{p.e}(1 + \frac{0.8}{2+p})\sqrt{\frac{1}{N}} \text{ for Barrel gas radiator}$$

$$\sigma_{ring}^{Forward} = \sigma_{p.e}\ 0.85\ (1 + \frac{0.8}{2+p})\sqrt{\frac{1}{N} + \frac{1}{12}} \text{ for Forward gas radiator}$$

where $\sigma_{p.e}$ is given by equation 5.8.

Of course, we don't take this procedure on trust. Lots of checks have been made in order to verify the good treatment of the data and the reliability of these informations. Figures 5.11 and 5.12 show the good agreement between real data (dots) and simulated data (histograms) for the observed number of photoelectrons per ring (or track), the expected error on the Cherenkov angle per track or ring (σ_{ring}), the difference between the measured Cherenkov angle and the expected one in the pion hypothesis ($\theta_{ring}^{meas} - \theta_c^{\pi}$) and the *pull* distribution ($(\theta_{ring}^{meas} - \theta_c^{\pi})/\sigma_{ring}$), in the gas radiators of the Barrel RICH and the Forward RICH, respectively.

5.2.2 Identification algorithms

Various particle identification algorithms based on these informations have been developed [7], depending on the requirements of the different physics analyses. Some physics analyses (like the analysis treated in our work) need an individual track identification, while others measure statistically the content of a given sample, without associating a mass to each track.

• For statistical analyses, one needs a continuous estimator of the observed Cherenkov angle, independent of any mass hypothesis, such that the average number of particles of a given type can be determined. This approach was used for the first measurement of the s-quark forward-backward asymmetry [8] by exploiting as continuous estimator not directly the Cherenkov angle (θ_c) but the corresponding mass squared (m^2) distribution using the relation :

$$m^2 = p^2(n^2 \cos^2 \theta_c - 1) \tag{5.9}$$

where p is the track momentum and n the refractive index of the medium.

For a given type of particle with a momentum (p), the m^2 distribution resulting from the measurement of θ_c is Gaussian. Considering the momentum distribution to be exponential and integrating the m^2 distribution over the selected momentum range, the resulting distribution is in first approximation a Breit-Wigner like distribution. A fit to the m^2 distribution (see figure 5.13) with the sum of two Breit-Wigner curves, one for the saturated Cherenkov rings (e, μ and π) and one for kaons, allows one to evaluate the average number of particles corresponding to each mass hypothesis.

• For track-by-track tagging, the observed signal is compared with that expected for the various particle types, namely e, μ, π, $K^{\pm}$ and protons, at the measured momentum. Depending on the analysis one wants to perform, the priority may be either high rejection[2] or high identification efficiency. The requirements also depend on whether only pion rejection or proton/kaon separation are required.

This approach is the most used approach and the one applied in our analysis. It exploits the distance between the measured Cherenkov angle (θ_{ring}^{meas}) and the theoretical expectation of the Cherenkov angle for a given mass hypothesis (θ_c^h), in terms of the expected error per ring (σ_{ring}, see section 5.2.1), commonly called *pull* :

$$p_h = \frac{\mid \theta_{ring}^{meas} - \theta_c^h \mid}{\sigma_{ring}} \tag{5.10}$$

[2]The rejection is defined as the ratio of the : $\frac{\varepsilon_{X'}^{X'}}{\varepsilon_{X}^{X'}}$ with $\mathcal{E}$ the efficiencies as defined by relation 5.13.

Let us notice that the expected Cherenkov angle (θ_c^h) is calculated from the refractive index. After the fixing of the RICH detectors has been done, the refractive index for data and simulation is fixed to one constant value ($n_{Barrel\ gas} = 1.0019407$ and $n_{Forward\ gas} = 1.0015118$ for 1994 data).
A detailed description of this identification algorithm is given in [9]. For each mass hypothesis, it is optimised with respect to different momentum windows corresponding to the various possible combinations of the information coming from the liquid and the gas radiators of the RICHes, signal or veto information.
Four different levels of identification (very loose, loose, standard or tight) are possible corresponding to the following basic criteria :

- one verifies whether the measured Cherenkov angle (θ_{ring}^{meas}) of the track one wants to identify is compatible within 2.5 standard deviations (σ_{ring}) with the given hypothesis h :

$$p_h < 2.5 \tag{5.11}$$

- one checks the separation with other hypothesis h' :

$$p_{h'} > 0,\ 1,\ 2,\ 3\ h' \neq h \tag{5.12}$$

This last selection gives the choice between the four levels of identification according to the strictness required in the analysis. So, for example, a given track is identified as a 'standard' kaon if its measured Cherenkov angle (θ_{ring}^{meas}) is compatible with the kaon hypothesis (θ_c^K) within 2.5 standard deviations (σ_{ring}) and if it is further than 2 standard deviations from the π hypothesis : $p_K < 2.5$ and $p_\pi > 2$. This is illustrated on figure 5.14 for a track (with momentum $p = 18$ GeV/c) selected in a real event and emitting Cherenkov light in both radiators of the Barrel RICH. In the liquid radiator, the reconstructed Cherenkov angle is saturated but in the gas radiator the kaon mass hypothesis is clearly selected.
In order to show the performances of this identification algorithm, The efficiency $\mathcal{E}$ and purity $\mathcal{P}$ matrices have been computed from simulated data. The matrix elements are defined by :

$$\mathcal{E}_X^{X'} = \frac{\text{Numb. of simulated } X \text{ particles tagged as } X'}{\text{Total numb. of simulated } X \text{ particles}} \tag{5.13}$$

$$\mathcal{P}_X^{X'} = \frac{\text{Numb. of simulated } X \text{ particles tagged as } X'}{\text{Total numb. of tagged as } X' \text{ particles}} \tag{5.14}$$

where "tagged" means identified by the identification algorithm.

These matrices are shown on figures 5.15 and 5.16 for the 'standard' identification level corresponding to $p_{h'} \geq 2$ as function of the particle momentum. The criteria that we have applied are given and argued in the next chapter.

5.3 Comparison data-simulation

To be sure that the results obtained on simulation are reliable and reproduce in a consistent way the real data, extensive checks have been made. One of them has been already shown on figures 5.11 and 5.12 which give the comparison between real data and simulation for the fundamental quantities measured by the RICH detectors.
Another distribution relevant for the control of the consistency between data and simulation is the mass squared distribution (see relation 5.9) for charged particles with high momentum. On this distribution reproduced on figure 5.17 for the barrel RICH and on figure 5.18 for the forward RICH, we see the good agreement obtained between real data and simulation in the region corresponding to the kaon peak.
These checks confirm that the signals produce by the charged kaons in the RICHes are well understood and correctly reproduced by the simulated data, allowing the evaluation of the kaon identification efficiency on the simulation.
However, we can observe a residual discrepancy between real data and simulation in the distributions of the mass squared 5.17 and 5.18 under the peak corresponding to the saturated Cherenkov angles (e, μ and π). This discrepancy comes from the fact that the background photoelectrons produced in the drift tubes of the RICHes are not very well reproduced by the simulation : the simulation under estimate this background which leads to a signal cleaner than it is in reality. Consequently, the misidentification efficiency (defined as the efficiency for a particle X to be identified as X', $X \neq X'$) for saturated Cherenkov angles is under estimated and the kaon identification purity evaluated on simulation is thus artificially increased.
This problem is well understood and was taken into account in our study (see section 6.5.2).

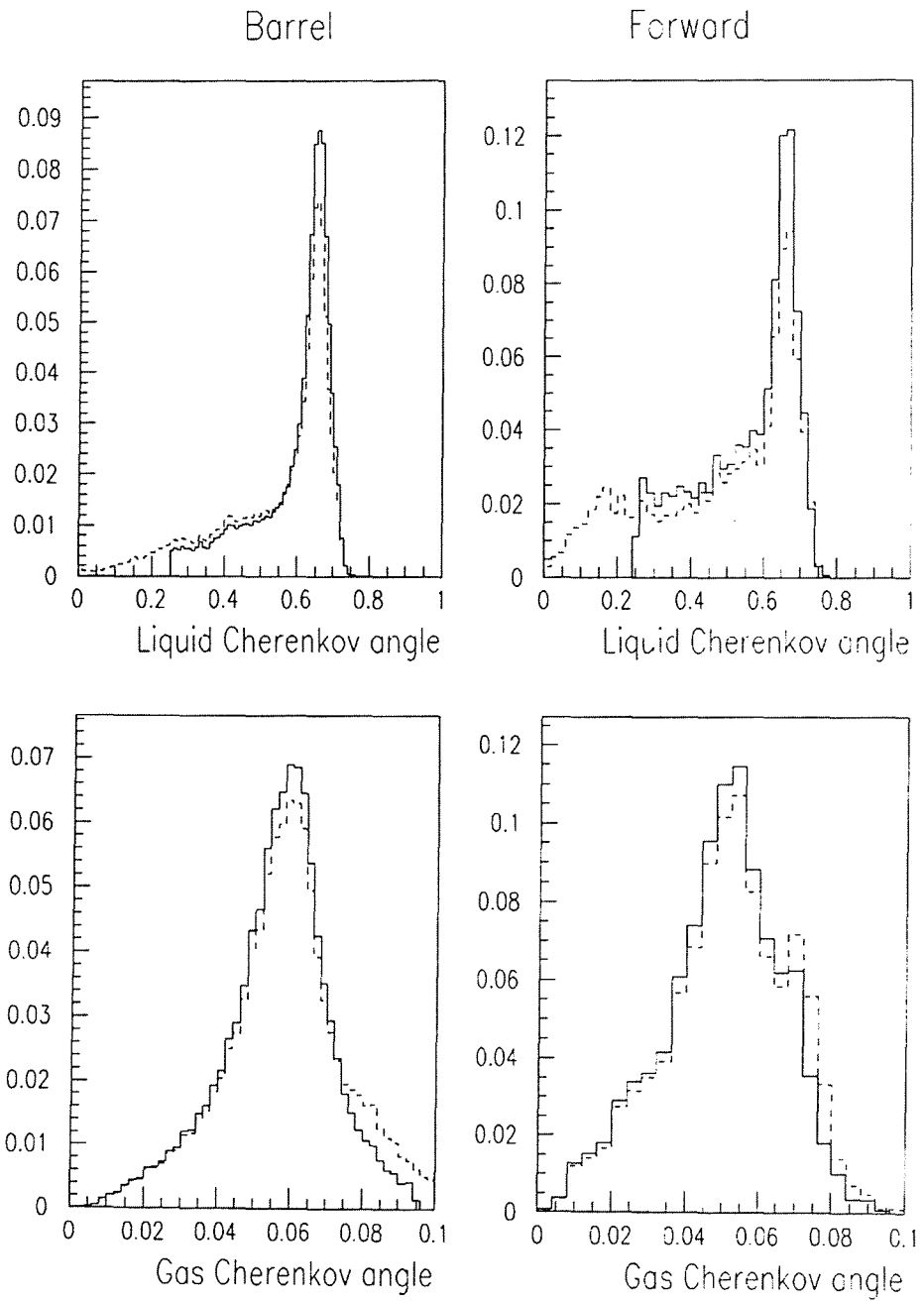

Figure 5.8: Single photoelectron distributions for simulated pions in the liquid (gas) radiator for the barrel (forward) RICH before (dashed line) and after (solid line) applying weights.

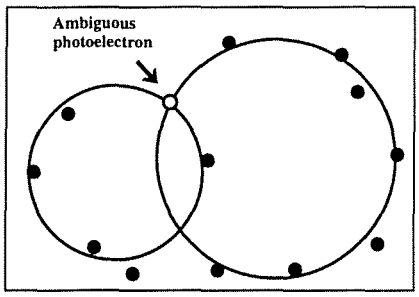

Figure 5.9: Illustration of an ambiguous photoelectron. The dots represent the photoelectrons and the circles, the reconstructed rings.

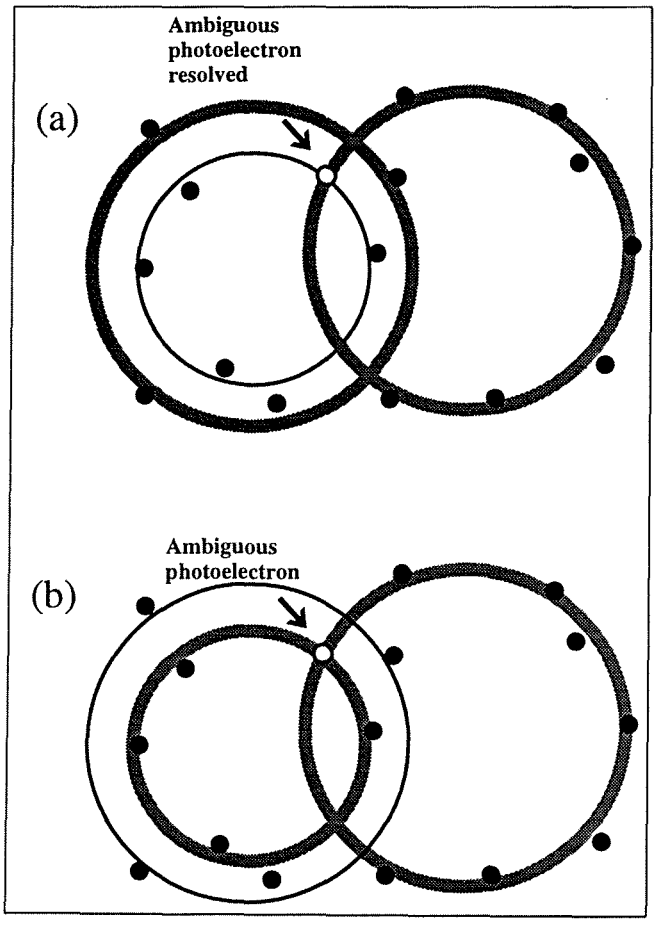

Figure 5.10: The two situations of ambiguous photoelectron. The dots represent the photoelectrons, the thick grey circles are the selected rings. (a) The photoelectron is associated to only one selected cluster, (b) The photoelectron is associated to two selected clusters.

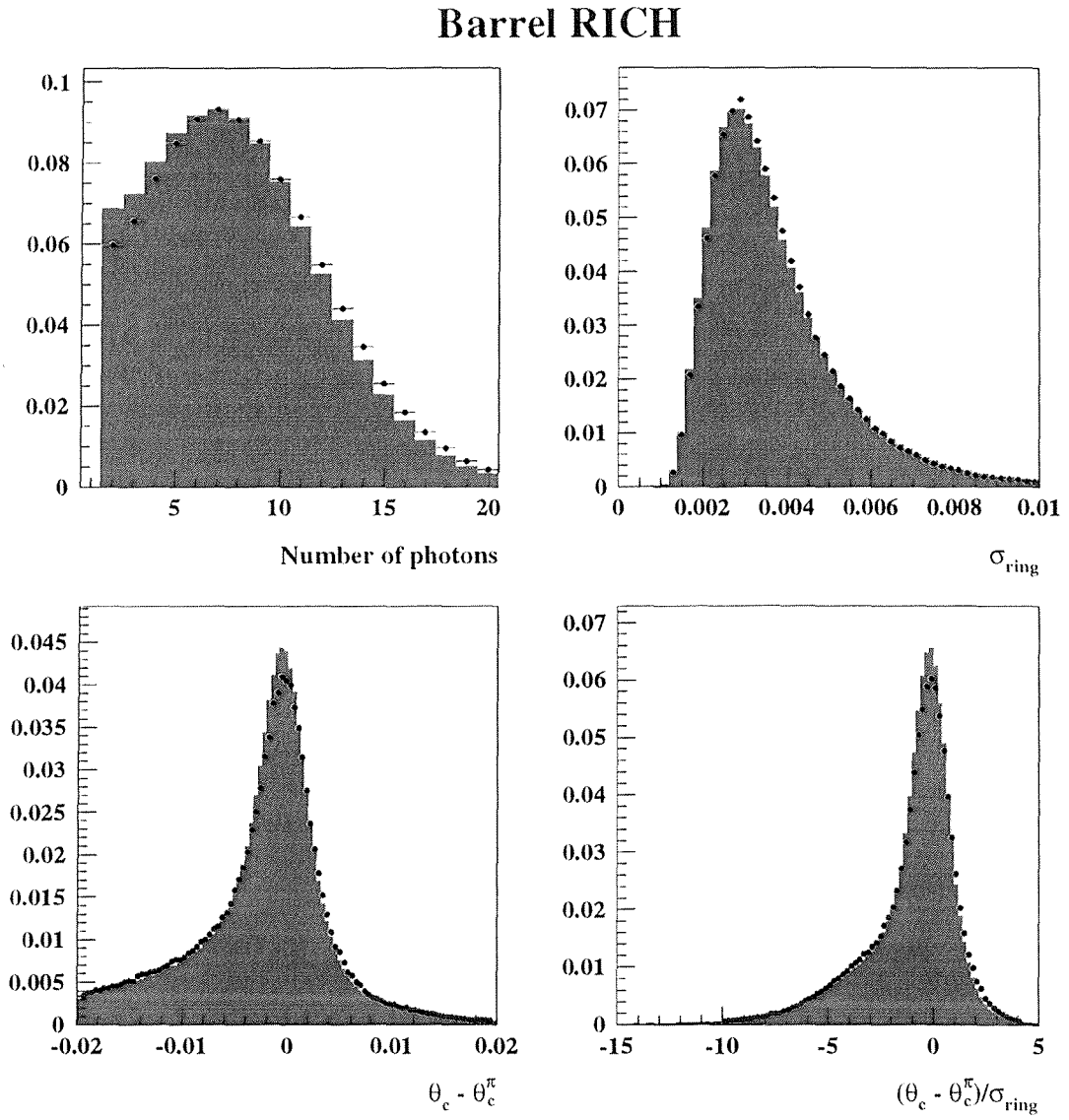

Figure 5.11: Distribution for charged particles (with momentum between 10 GeV/c and 24 GeV/c) in the gas radiator of the Barrel RICH for real data (dots) and simulation (histograms) for the observed number of photoelectrons per ring (or track), the expected error on the Cherenkov angle per ring, the difference between the measured Cherenkov angle and the expected one in the pion hypothesis and the *pull* distribution for the pion hypothesis.

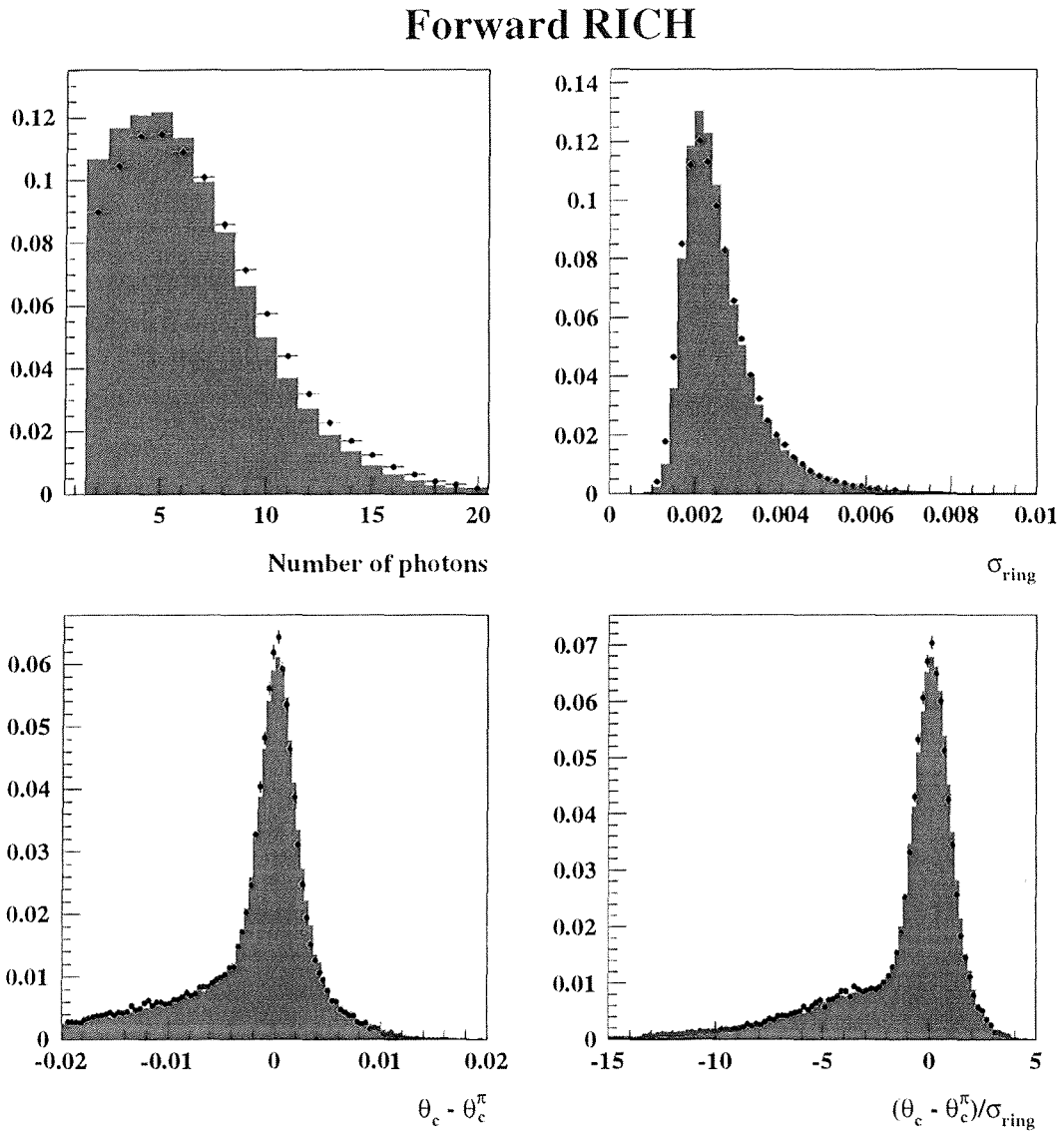

Figure 5.12: Distribution for charged particles (with momentum between 10 GeV/c and 24 GeV/c) in the gas radiator of the Forward RICH for real data (dots) and simulation (histograms) for the observed number of photoelectrons per ring (or track), the expected error on the Cherenkov angle per ring, the difference between the measured Cherenkov angle and the expected one in the pion hypothesis and the *pull* distribution for the pion hypothesis.

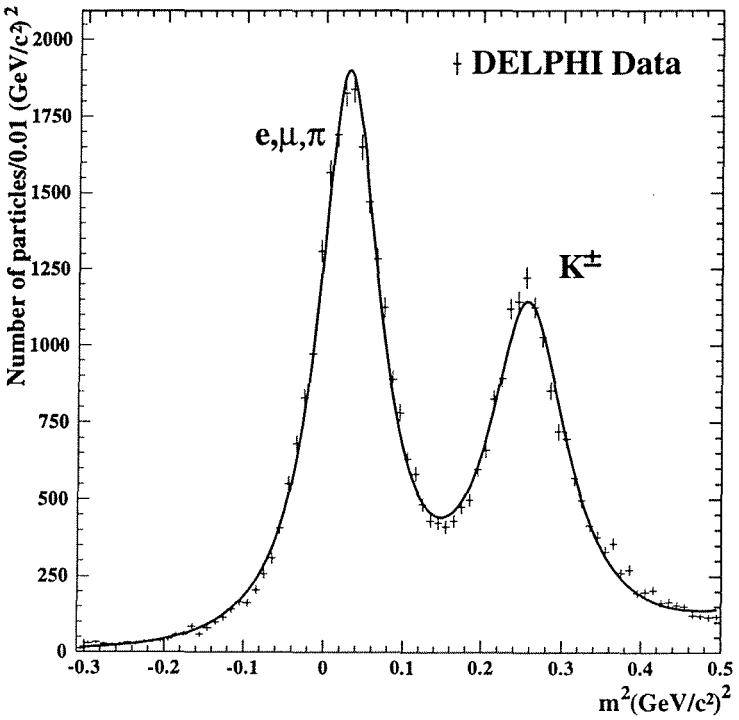

Figure 5.13: Mass squared distribution using the RICH detector for all charged particles with momentum between 10 GeV/c and 18 GeV/c.

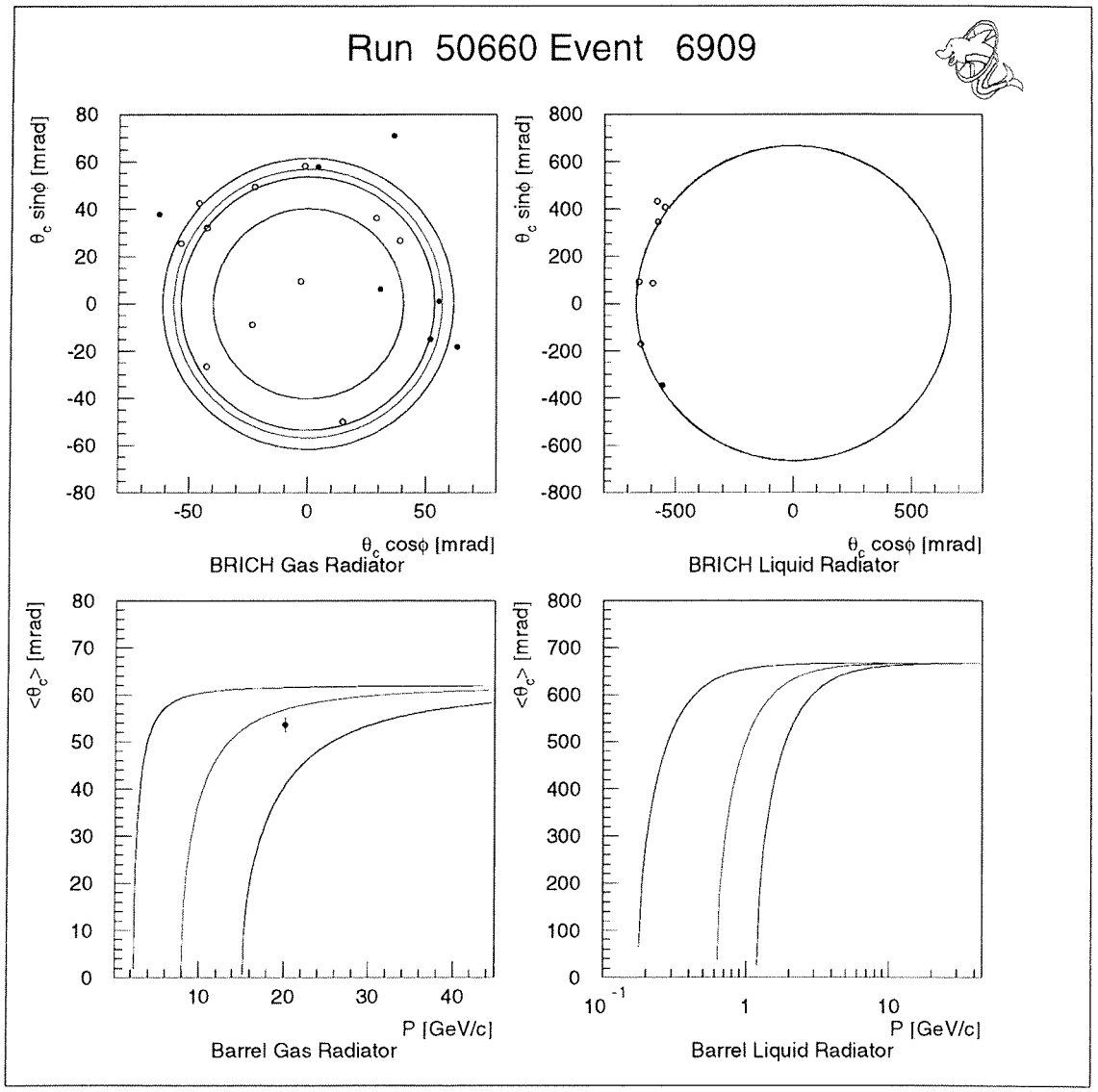

Figure 5.14: Upper plots : Reconstructed Cherenkov rings (black rings) for a track emitting Cherenkov photons in the gas radiator (left) and the liquid radiator (right) of the barrel RICH compared to the expected rings for the three mass hypotheses pion (blue), kaon (green) and proton (red) (the photoelectrons for which the reconstruction of the ring is the most reliable are represented with black dots). Lower plots : these reconstructed Cherenkov angles are compared to the expectations. The kaon mass hypothesis is clearly selected.

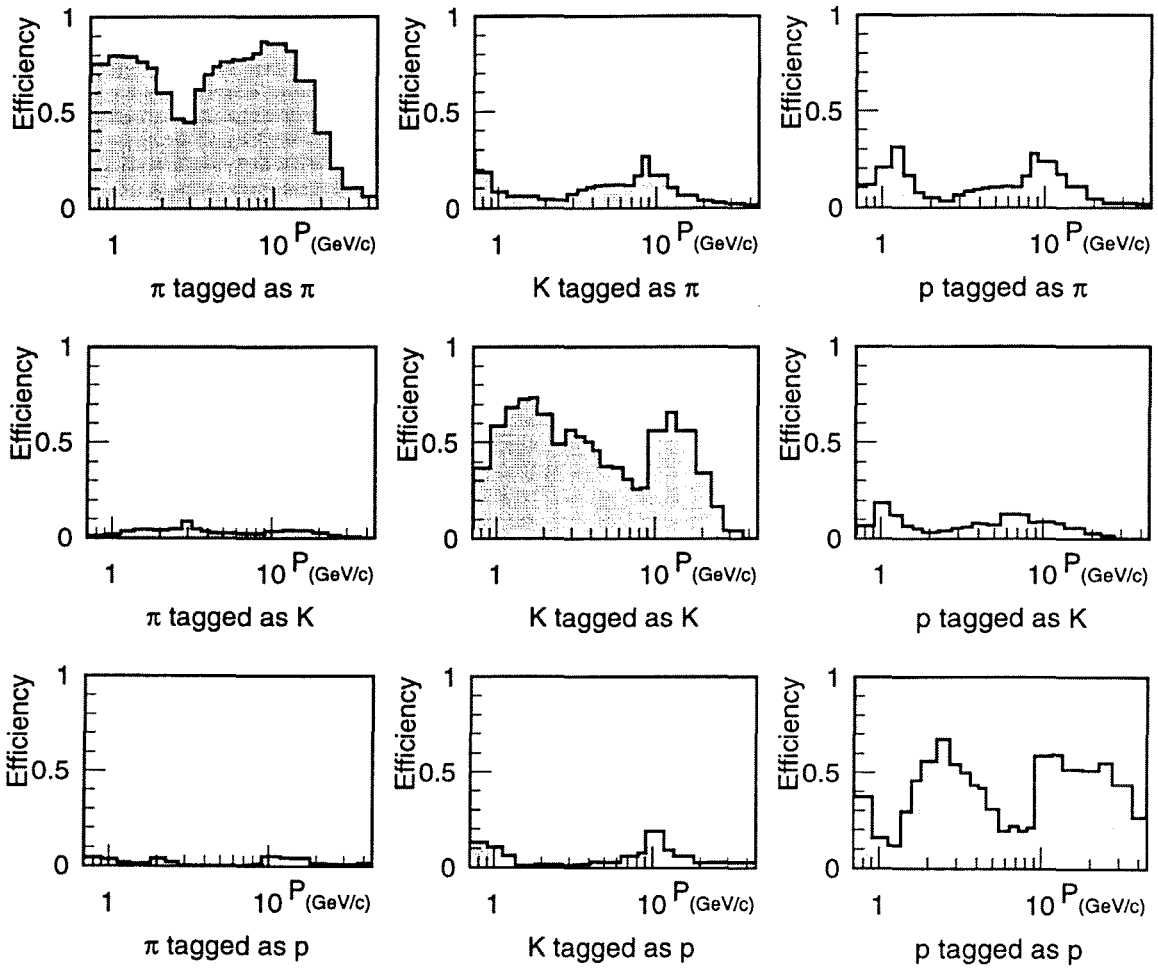

Figure 5.15: Identification efficiency matrix for the identification level corresponding to $p_{h'} \geq 2$, obtained with simulation.

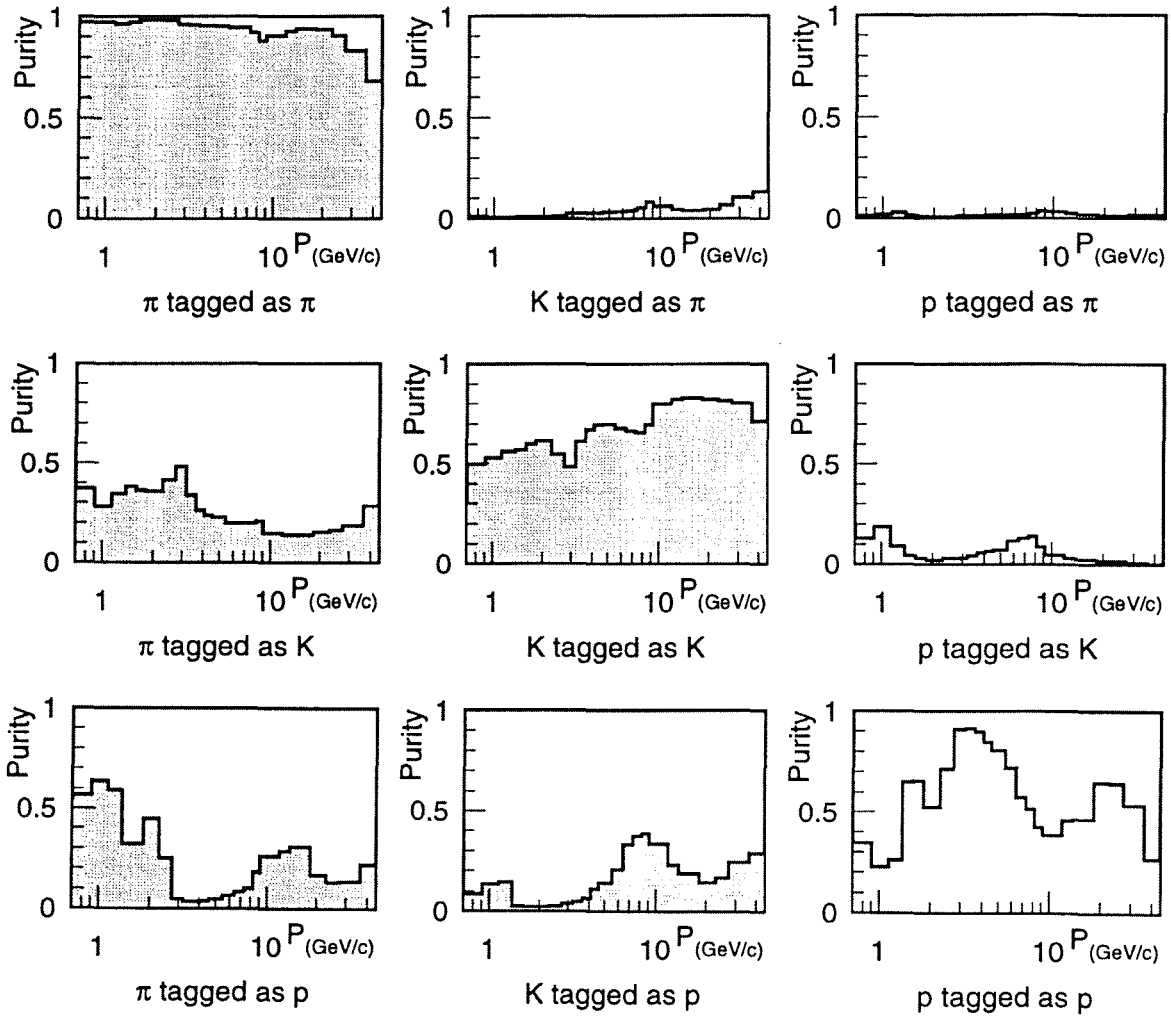

Figure 5.16: Identification purity matrix for the identification level corresponding to $p_{h'} \geq 2$, obtained with simulation.

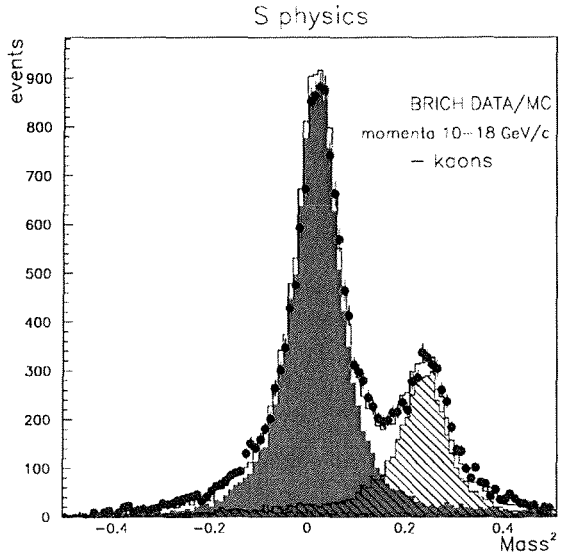

Figure 5.17: Mass squared distribution for charged particles with $10 < p < 18$ GeV/c identified by the Barrel RICH. The dots show the real data and the line, the simulation.

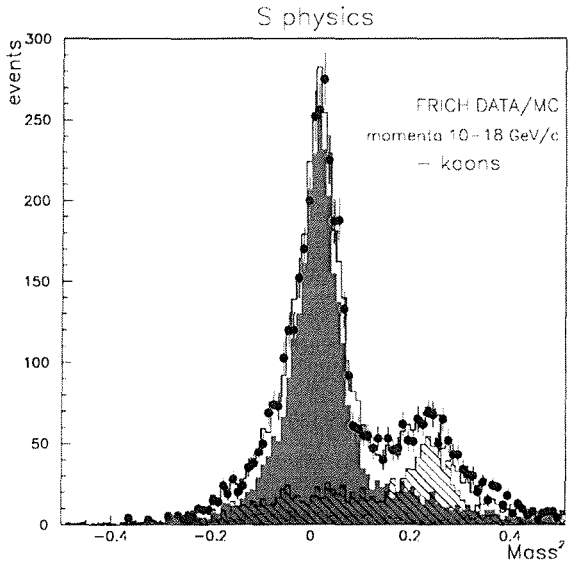

Figure 5.18: Mass squared distribution for charged particles with $10 < p < 18$ GeV/c identified by the Forward RICH. The dots show the real data and the line, the simulation.

Bibliography

[1] D. Braun, M. Frank, Tagging Bhadrons using track imp. param. ALEPH Note 92-135.

[2] DELPHI Coll., P. Abreu et al., *Nucl. Instr. and Meth.* **A378** (1996) 57; DELPHI report 94-125 PROG 208.

[3] JADE Coll., W. Bortel et al., *Z. Phys.* **C33** (1986) 23; S. Betwake, *Phys. Lett.* **B213** (1988) 235.

[4] DELPHI Coll., P. Abreu et al, *Z. Phys.* **C65** (1995) 555.

[5] W. Adam et al., *Nucl. Instr. and Meth.* **A371** (1996) 240.

[6] DELPHI report 96-133 RICH 90.

[7] DELPHI Coll., P. Abreu et al., *Nucl. Instr. and Meth.* **A378** (1996) 57.

[8] DELPHI Coll., P. Abreu et al, *Z. Phys.* **C67** (1995) 1.

[9] DELPHI report 96-103 RICH 89.

Chapter 6

Measurement of the forward-backward asymmetry in $e^+e^- \rightarrow Z^0 \rightarrow s\bar{s}$

As an introduction to this chapter, we remind briefly the different determinations of the $s\bar{s}$ forward-backward asymmetry to which we have collaborated and which are already published.
Then, we describe in details the method we have elaborated to improve the determination of the $s\bar{s}$ forward-backward asymmetry. It is deduced from the angular distribution of the charge kaons of high momentum individually identified both in the barrel region (thanks to the Barrel RICH) and in the forward region (thanks to the Forward RICH). We discuss the selection criteria applied to obtain a sample as pure as possible of $s\bar{s}$ events and the procedure to compute the $s\bar{s}$ forward-backward asymmetry from the charged kaon asymmetry. Finally we evaluate the systematic errors.

6.1 Introduction

The first measurement of the $s\bar{s}$ forward-backward asymmetry to which we have contributed was published by the DELPHI collaboration [1]. This analysis used the data collected in 1992 (about 0.7×10^6) and extracted the $s\bar{s}$ asymmetry from the distribution of two types of strange hadrons : charged kaons (with a momentum between 10 and 18 GeV/c identified by the Barrel RICH) and Λ^0 baryons with ($10 \leq p \leq 23$ GeV/c). In each case, the experimental procedure applied to enrich the sample of hadronic events in strange quark events relied only on the identification of the corresponding strange hadrons which led in both cases to a purity in $s\bar{s}$ events of about 43% .

The following results were obtained for the $s\bar{s}$ asymmetry at the Z^0 pole :

$$\begin{aligned} A^0_{s\bar{s}}(K^{\pm}) &= 0.128 \pm 0.037(stat.) \pm 0.013(syst.) \\ A^0_{s\bar{s}}(\Lambda^0) &= 0.164 \pm 0.109(stat.) \pm 0.057(syst.) \end{aligned} \tag{6.1}$$

Our preliminary analysis of the data collected during 1994 is presented in [2], based on the identification of the charged kaons only, leading to :

$$A^0_{s\bar{s}}(K^{\pm}) = 0.111 \pm 0.019(stat.) \pm 0.020(syst.) \tag{6.2}$$

Charged kaons were preferred among other strange hadrons (like Λ^0) produced in multihadronic decays of the Z^0 because of their relatively high mean multiplicity (about seven times greater than the Λ^0 one, see table 6.1). We notice that for the first results obtained with charged kaons and Λ^0 quoted in equations 6.1, the statistical error is about three times larger for the method using Λ^0 than the one using $K^{\pm}$. Moreover, unlike the present analysis, the previous results exploited only the Barrel RICH data.

Hadrons	**Multiplicity/event**
$K^{\pm}$	2.39 ± 0.12
K^0_S	2.01 ± 0.04
Λ	0.368 ± 0.014
$\phi(1020)$	0.100 ± 0.008
K^{*0}	0.742 ± 0.042
Ξ^-	0.0227 ± 0.0018

Table 6.1: Mean experimental multiplicity of hadrons with a strange quark, over the whole momentum spectrum [3].

The present measurement uses the capability of the DELPHI detector to identify individually charged kaons $K^{\pm}$ both in the barrel and in the forward region. It is based on the whole set of data which have been collected during 1994 (about 1.35×10^6 multihadronic Z^0 decays), period during which the largest statistics with a fully operational RICH detector (Barrel and Forward) was recorded.

Two different analysis have been performed :

- the first one (which is referred to as the **Barrel analysis**) is based on the identification of fast charged kaons in the Barrel RICH and on the reduction of the contamination of $b\bar{b}$ and $c\bar{c}$ events using the Brown and Frank

algorithm described in chapter 5. The purity in $s\bar{s}$ events of our sample is increased up to 55%.

- the second one (which is referred to as the **Forward analysis**) is simply based on the identification of fast charged kaons with the Forward RICH. It allows to measure the asymmetry in an angular region favoured from a statistical point of view by the cross-section and where the asymmetry is maximum and less sensitive to errors in the $s\bar{s}$ direction estimate. The purity reached in strange quarks is of 43%. The Brown and Frank algorithm, which needs precisely reconstructed tracks, was not applied in the forward region because of the little geometrical overlap of the Forward RICH with the acceptance of the Vertex Detector.

6.2 Data sample

6.2.1 Hadronic event selection

For the present analysis, we used only events registered when the DELPHI detector was running under optimum conditions (no trips, no power failure, no gas leak, etc...)[1].
The hadronic events (i.e. $q\bar{q}$ events) were selected using the standard DELPHI collaboration criteria [4] :

Momenta of charged tracks and event multiplicity are the only quantities on which the hadronic event selection criteria are based. To ensure that these quantities are reliably measured, only charged tracks satisfying the following criteria are used :

⋆ a momentum p larger than 0.4 GeV/c with a relative error $\frac{\sigma(p)}{p}$ less than 1;

⋆ a track length in the TPC longer than 30 cm ;

⋆ a polar angle θ in the range :

$$20^\circ \leq \theta \leq 160^\circ$$

⋆ an impact parameter with respect to the average interaction point smaller than 4 cm in the $r\phi$ plane (transverse to the beam) and smaller than 10 cm in $\mid z \mid$ (along the beam).

[1] Commonly called 'run selection'.

Restricting the impact parameter to a small volume around the interaction region, vetoes cosmic ray events and beam-related backgrounds (collisions between the incident e^- or e^+ and the beam pipe, or stray molecules in the beam pipe) occurring outside this volume.

An event is then selected as hadronic final state if it satisfies :

- ⋆ at least 4 charged tracks are present in the event ;
- ⋆ the total energy of all charged particles is greater than 15 GeV, evaluated from momenta assuming all particles to be pions ;
- ⋆ the total energy of the charged tracks in the forward direction ($\theta < 90°$) and in the backward direction ($\theta > 90°$) exceeds 3 GeV assuming all particles to be pions.

A total of 1.35×10^6 hadronic events were selected.
The multiplicity cut removes all muon pairs, Bhabha scattering events and the remaining cosmic background.
The number of $\tau\bar{\tau}$ events and beam-related background is significantly reduced, as is the number of $\gamma\gamma$ events : hadronic events were generated with the JETSET PS 7.3 model [5], as tuned by the DELPHI collaboration [6]. The Lund symmetric fragmentation function described the light quark hadronization process, while the Peterson function was used for the fragmentation of bottom and charm quarks (see section 2.3.1). The detector response was simulated with the DELPHI simulation program DELSIM (see section 2.3.1). By simulation of a sample of 2.4×10^6 hadronic events, the background due to $\tau^+\tau^-$ events has been estimated to be less than 0.2%, events due to beam-gas scattering and $\gamma\gamma$ interactions have been estimated to be less than 0.1%. The efficiency for selecting hadronic Z^0 decays was estimated to be over 95%.

6.3 Sample selection

6.3.1 Rejection of heavy quarks in the barrel region

After the general selection of hadronic events as given in the previous section, heavy flavour rejection is applied by a method based on the Brown and Frank algorithm (described in section 5.4.1). This method consists in separating events in which a group of particles are believed to be emitted from secondary vertices (B, D decays). It used the positive significance probability P_E^+ that the tracks of the event with a positive impact parameter originate from the

primary vertex. Since this algorithm relies on the Vertex Detector to compute this probability, it is important to obtain a good reconstruction, to limit the polar angle of the thrust axis of the events to the barrel region :

$$| \cos \theta_{\mathbf{thrust}} | \leq \mathbf{0.7} \tag{6.3}$$

Moreover this ensures stable performances of the Brown and Frank algorithm as a function of the polar angle of the event axis.
We accept events if :

$$\mathbf{P_E^+ > 0.15} \tag{6.4}$$

which leads to :
- a $b\bar{b}$ contamination $\leq 7\%$
- a $c\bar{c}$ contamination $\leq 18\%$
- an $s\bar{s}$ selection efficiency $\geq 80\%$

as evaluated from the full DELPHI simulation (See figure 6.1).

6.3.2 Charged kaon identification

Barrel analysis

After the rejection of the events having tracks which do not originate from the primary vertex, essentially $b\bar{b}$ and $c\bar{c}$, we select hadronic events with fast charged kaons, as identified by the Barrel RICH. This selection has two objectives :

- to increase the content of our sample of hadronic events in $s\bar{s}$ events, reducing the number of $u\bar{u}$ and $d\bar{d}$ events ;
- to gain information about the charge of the s quarks from the charge of the kaon ($K^- \equiv s\bar{u}$ and $K^+ \equiv \bar{s}u$).

Figure 6.2 shows the expected charged kaon momentum spectra separately for the 5 flavours using the JETSET PS Model. We see that for high momenta ($p > 10$ GeV/c), the $s\bar{s}$ contribution is larger than that of the other flavours.

Only tracks passing with success the following criteria are identified as kaons in the **barrel region** :

- their polar angle θ has to fall in the Barrel RICH angular acceptance :

$$\mathbf{0.04 <} | \cos \theta | \mathbf{< 0.68} \tag{6.5}$$

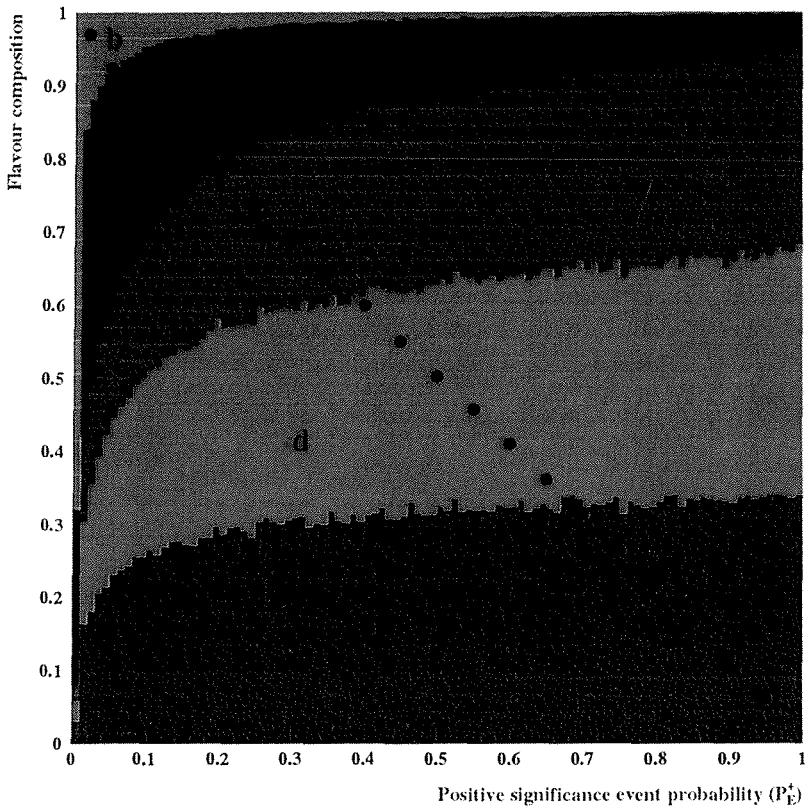

Figure 6.1: Flavour composition of a sample of hadronic events as a function of the event significance probability P_E^+. The superimposed dots show the selection efficiency of strange quark for the minimum value of P_E^+ required.

because the identification procedure uses the explicit reconstruction of the Cherenkov ring produced by the track crossing the Barrel RICH and reconstructed in the operational region of the photon detectors.

• they have to be associated to a signal in the Time Projection Chamber (**TPC**) and the Outer Detector (**OD**), the tracking detectors surrounding the Barrel RICH. This condition rejects the cases where an hadronic interaction occurs before the RICH or with the material of the RICH and ensures that only well reconstructed tracks crossing the Barrel RICH are used in the measurement.

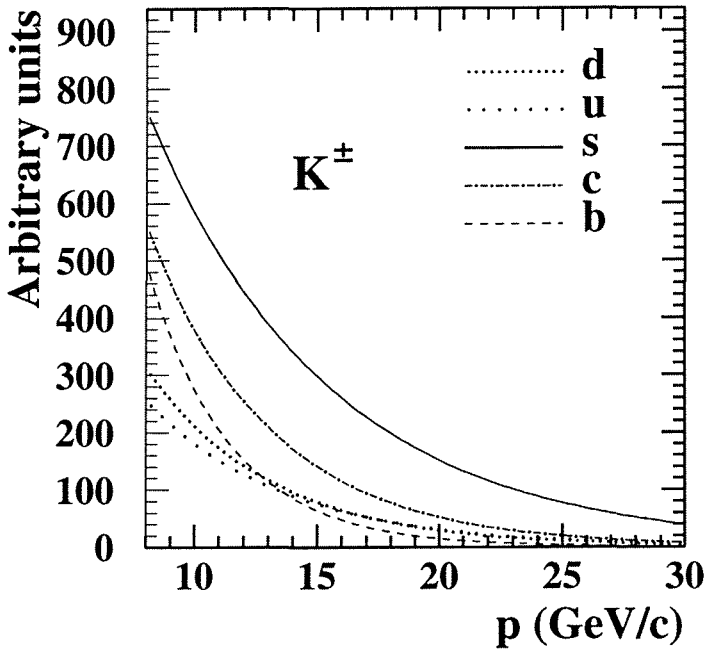

Figure 6.2: Expected charged kaon momentum spectra separately for the 5 flavours as obtained from the JETSET PS Model.

- their momentum has to be in the range :

$$10 \text{ GeV/c} \leq \mathbf{p} \leq 24 \text{ GeV/c} \tag{6.6}$$

The choice of this momentum window is dictated by the experimental capability to identify correctly the charged kaons and by the necessity to have a good compromise between the efficiency and the purity of the selection of the s-quark. The lower limit is constrained by the Cherenkov emission threshold ($p \sim 8.5$ GeV/c) in the gas radiator of both RICHes and is set to 10 GeV/c to be well above this threshold and thus to ensure good reconstruction of Cherenkov rings. The upper limit at 24 GeV/c is imposed to ensure that the kaon rings are still well separated from the fully saturated rings due to electrons, muons and pions (see figure 6.4).

- their measured average Cherenkov angle θ_{ring}^{meas} satisfies [7] :

$$| \theta_{\mathbf{ring}}^{\mathbf{meas}} - \theta_{\mathbf{c}}^{\mathbf{K}} | < \mathbf{2.5}\ \sigma_{\mathbf{ring}} \tag{6.7}$$

$$| \theta_{\mathbf{ring}}^{\mathbf{meas}} - \theta_{\mathbf{c}}^{\pi} | > \mathbf{2}\ \sigma_{\mathbf{ring}} \tag{6.8}$$

with σ_{ring} the corresponding expected error and θ_c^K (θ_c^π) the expected Cherenkov angle in the kaon (pion) hypothesis (see section 5.2.2).
Figures 6.3 show the resulting kaon identification purity and efficiency as a function of the kaon momentum for simulated $s\bar{s}$ events. We see that the kaon purity is almost constant in the whole momentum window used for our analysis. On the other hand, we notice the significant loss in efficiency when the kaon momentum exceed 24 GeV/c which is due mainly to the fact that that kaon band (in the plot of the average Cherenkov angle versus the particle momentum) gets closer to the saturated band of e, μ and π.

- the higher the momentum of the kaon used to tag the primary s or $\bar{s}$ quark is, the higher the probability that the kaon 'contains' the primary s or $\bar{s}$ quark is. This implies that if more than one charged kaon with the characteristics listed above is found, only **the highest momentum one** is considered.

A total of 43075 events with one identified $K^\pm$ were selected in the barrel region and will be used to deduce the $s\bar{s}$ asymmetry in this region.
Table 6.2 makes list of the computed flavour fractions in our sample for the barrel region as determined by simulation applying the criteria listed above. The purity reached in $s\bar{s}$ events is of about 55%.

Flavour	Fraction
d	14%
u	14%
s	55%
c	16%
b	1%

Table 6.2: Values for the flavour fractions in the barrel region as computed on simulation.

Forward analysis

In the forward region, the selection of $s\bar{s}$ events is based only on the identification of fast charged kaons by the Forward RICHes. The events defined as hadronic events by the selection given in section 6.2.1 have to fulfil the following criteria to be used in the Forward analysis :

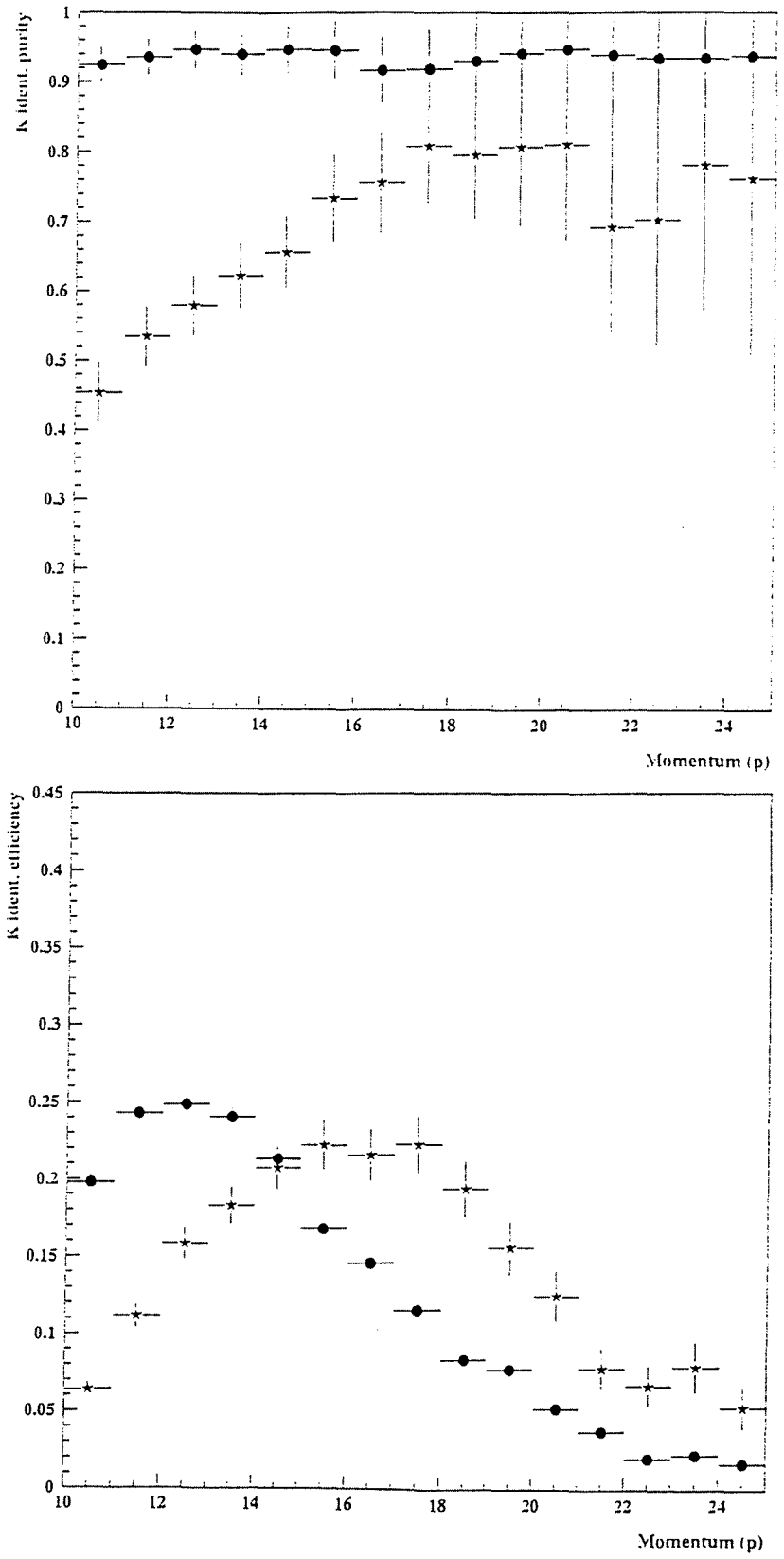

Figure 6.3: Kaon identification purity (top) and efficiency (bottom) as a function of the momentum, in the Barrel RICH (dots) and in the Forward RICH (stars).

• their thrust axis has to be in the angular region :

$$0.80 \leq | \cos\theta_{\mathbf{thrust}} | \leq 0.95 \tag{6.9}$$

The reason of this cut is to ensure that the estimation of the quark direction is reasonable. The lowest limit avoids injecting artificially in our sample, charged kaons with high transverse momentum with respect to the thrust axis (we reject events with the selected kaon in the FRICH acceptance but the thrust axis in the barrel region acceptance) which, moreover would give a larger contamination in bottom and charm quark events. The upper limit rejects events badly reconstructed because of the loss of tracks inside the beam pipe and the poor tracking efficiency in the very forward region.

The track selection listed above to identify fast charged kaons in the Barrel RICH stays valid for the Forward analysis excepted that :

• the tracks have to have their polar angle θ in the Forward RICH angular acceptance :

$$0.82 < | \cos\theta | < 0.94 \tag{6.10}$$

because the identification procedure uses the explicit reconstruction of the Cherenkov ring produced by the track crossing the Forward RICHes and reconstructed in the operational region of the photon detectors.

• only tracks associated to a signal in the **TPC** and the Forward Chamber B (**FCB**), the tracking detectors surrounding the Forward RICHes, are used (for the same reasons than in the Barrel analysis).

An additional cut on the polar angle of the track of $0.87 < | \cos\theta | < 0.94$ was applied for rings reconstructed in the odd-numbered drift chambers. For these chambers, the full Cherenkov ring could not be reconstructed for the tracks with their polar angle in the range $0.82 < | \cos\theta | < 0.87$, due to the fact that the photoelectrons drift under a Lorentz angle[2]. This zone was removed because it was found that the acceptance was different for positively and negatively charged pions. For even chambers, no dead zone is present. This is illustrated on figure 6.5 which shows the distribution of the Cherenkov photons in the driftbox of the Forward RICH. The effect of the Lorentz angle

[2]In the photon detector, the photoelectrons drift in a direction which forms an angle of about 50° (called the Lorentz angle) with respect to the electric field.

is clearly visible. About 20% of the particles were lost with this cut.

A total of 9396 events with one charged kaon identified by the Forward RICH were selected and used to compute the $s\bar{s}$ asymmetry in the forward region. The resulting purity in $s\bar{s}$ events is of 43% and the flavour fractions in our sample are given in table 6.3.

Flavour	Fraction
d	10%
u	10%
s	43%
c	23%
b	14%

Table 6.3: Computed values for the flavour fractions in the forward region.

6.4 The asymmetry measurement method

To facilitate the understanding, we give first the broad lines of the procedure we have followed to determine the $s\bar{s}$ asymmetry. Each step of the procedure will then be developed in the next sections.

For the reaction $e^+e^- \rightarrow Z^0 \rightarrow s\bar{s}$, the distribution of the s-quark angle θ relative to the electron direction (see figure 6.6) is expressed as :

$$\frac{d\sigma}{\cos\theta} \propto 1 + \frac{8}{3}A^s_{FB}\cos\theta + \cos^2\theta \qquad (6.11)$$

The term proportional to $\cos\theta$ expresses the forward-backward asymmetry A^s_{FB} which is fully defined in section 4.4.
In order to measure the asymmetry A^s_{FB}, we have to determine :

- the line of flight of the primary $s\bar{s}$ pair with respect to the axis of incidence of e^+e^-. The best estimator of this direction is given by the thrust axis common to the two jets (s and $\bar{s}$) (as defined in section 5.1.1) ;

- the angle of emission of the quark s relative to the incident e^- beam. This angle is determined considering the charge of the identified kaon : the quark polar angle θ is estimated by the thrust axis polar angle θ_{thr}, orienting the axis parallel (anti-parallel) to the K^- (K^+) projection along the axis itself (a negatively (positively) charged kaon K^- (K^+) is regarded as the

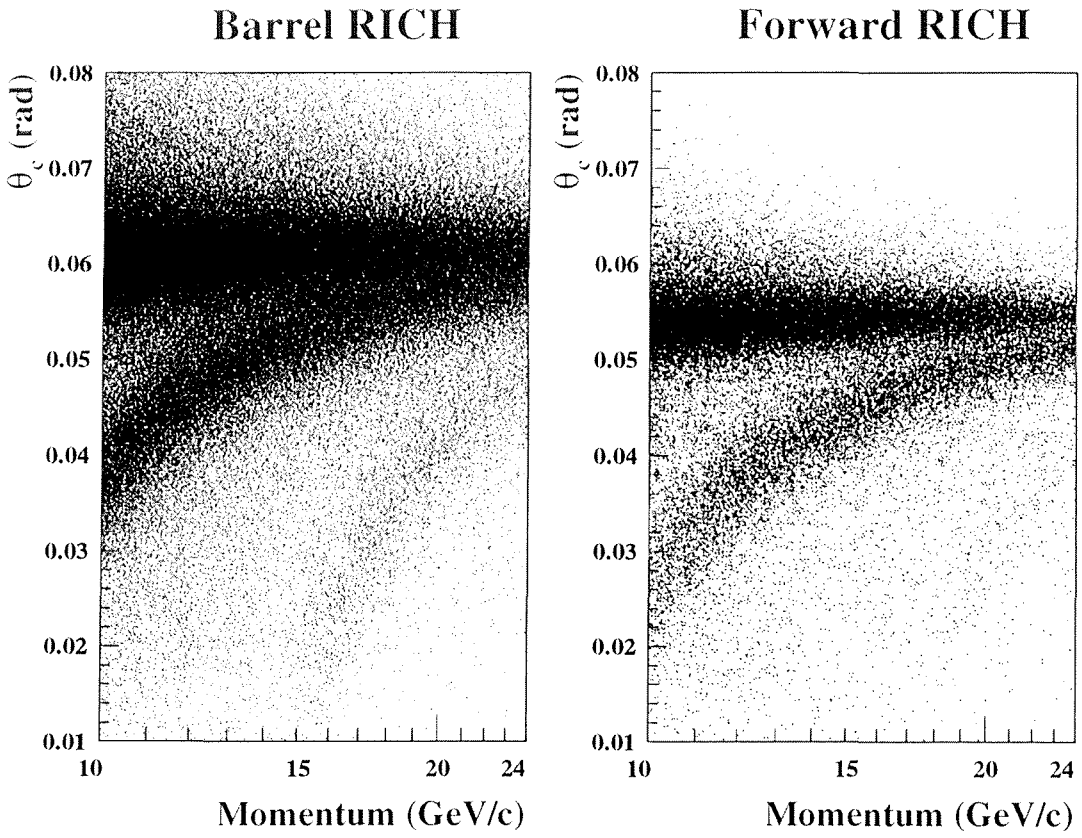

Figure 6.4: Reconstructed average Cherenkov angle in the gas radiator of the Barrel RICH (left) and the Forward RICH (right) as a function of the particle momentum (10 GeV/c $< p <$ 24 GeV/c).

signature of a quark s (an anti-quark $\bar{s}$), (see figure 6.6)).

In principle, the $s\bar{s}$ asymmetry A^s_{FB} could be obtained by counting the number of events with an s-quark emitted in the forward hemisphere ($\cos\theta > 0$ or $z > 0$) and the number of those with an s-quark emitted in the backward hemisphere ($\cos\theta < 0$ or $z < 0$). Since the s and the $\bar{s}$ quarks are expected to enter into a strange meson or baryon with relatively high momentum during the fragmentation process, the direction of emission of the quark can be estimated by the direction of emission of the corresponding kaon and the s-quark forward-backward asymmetry will be deduced from the asymmetry of the high energy charged kaons A^K_{FB} (we will see how later). In order to avoid correcting the asymmetry for the identification efficiency of the kaon

which is a function of the polar angle and to obtain a better sensibility of the measurement, we have exploited the theoretical expression which gives the forward-backward asymmetry as a function of the polar angle θ of the s quark produced :

$$A^K(\theta) = \frac{8}{3} A^K_{FB} \frac{\cos\theta}{1+\cos^2\theta} \tag{6.12}$$

By measuring the charged kaon asymmetry in angular intervals of θ and by making a fit of (6.12) to this angular distribution, the charged kaon forward-backward asymmetry A^K_{FB} can be determined. The details of this determination of A^K_{FB} of the charged kaon asymmetry are given in the following section. We have seen that our samples of events with one kaon are not 100% pure in $s\bar{s}$ events but are made of a mixing of the different quark flavours. For this reason, the $s\bar{s}$ asymmetry is extracted from the asymmetry A^K_{FB} (computed as explained in section 6.5) by inverting equation 6.13 which gives A^K_{FB} as a linear combination of the different quark forward-backward asymmetries A_q :

$$A^K_{FB} = \sum_q \alpha_q \, (2c_q - 1) \, A_q \quad (q = d, u, s, c, b) \tag{6.13}$$

where α_q is the fraction of selected events with flavour q as primary quark and c_q is the probability that the charge of the kaon tags correctly the event hemisphere, as defined by the thrust axis, in which the primary quark is present. The term $(2c_q - 1)$ is explained on figure 6.7.

In the next section, we discuss the measurement of A^K_{FB} while the details of the determination of A_s (from A^K_{FB}) are given in section 6.6.

6.5 Charged kaon asymmetry

6.5.1 Experimental procedure

The measurement of the charged kaon asymmetry could be performed using kaons of the same charge in opposite angular regions with respect to the e^- beam ($\cos\theta > 0$ and $\cos\theta < 0$). In order to avoid the evaluation of the relative identification efficiency of the kaons in both hemispheres, the charged kaon asymmetry $A^K(\theta)$ is evaluated using the number of events with negatively (N^-_K) and positively (N^+_K) charged kaon in the same angular

region :

$$\begin{aligned} &\text{for } z < 0 : \\ &A^K(\theta) = \frac{N_K^+(\cos\theta < 0) - N_K^-(\cos\theta < 0)}{N_K^+(\cos\theta < 0) + N_K^-(\cos\theta < 0)} \\ &\text{for } z > 0 : \\ &A^K(\theta) = \frac{N_K^-(\cos\theta > 0) - N_K^+(\cos\theta > 0)}{N_K^-(\cos\theta > 0) + N_K^+(\cos\theta > 0)} \end{aligned} \tag{6.14}$$

All efficiency factors, coming from geometry, detector malfunctioning, particle identification, cancel in the ratios. The obtained results for A_{FB}^K using the data, either for $z < 0$ or $z > 0$, will be seen (see section 6.5.4), as expected, to be compatible with each other.
Because of the fact that the kaon asymmetries 6.14 have to be corrected for two effects (see sections 6.5.2 and 6.5.3) :

- the contamination of our selected sample of events with a high momentum $K^\pm$ by events in which a pion has been wrongly identified as a kaon.
- the spurious asymmetry induced by the detector material in front of the RICH detectors. K^+ and K^- have different hadronic cross-sections and thus are absorbed differently by the material in front of the RICH detectors.

which depend on the polar angle of the kaons θ_K, they are computed in bins i of the polar angle of the $K^\pm$ ($A_i^K = A^K(< \theta_K >_i)$. The bins in θ_K were chosen such that the corrections applied vary only slightly ($< 5\%$) inside the interval i, and therefore an average value for each correction can be safely used for all the events with their kaon present in the given interval. To avoid evaluating the relative efficiencies of the mirrors of the RICH detectors, the angular intervals i were chosen in order to correspond to the angular coverage of each mirror. Considering globally both hemispheres ($z > 0$ and $z < 0$), we have $2 \times 6 = 12$ mirrors for the Barrel RICH and $2 \times 2 = 4$ mirrors for the Forward RICH, see table 6.4. To evaluate correctly the contribution to the asymmetry of each event j with a kaon present in the bin i and for which the thrust axis makes a polar angle θ_j, the observed asymmetry in each interval i of $\cos\theta_K$, corrected for the contamination and material interaction effects, A_i^{obs}, will be expressed as :

$$A_i^{obs} = w_i A_{FB}^K \tag{6.15}$$

	$\mid \cos\theta_K \mid$
BRICH	$0.68 - 0.61$
	$0.61 - 0.52$
	$0.52 - 0.42$
	$0.42 - 0.30$
	$0.30 - 0.17$
	$0.17 - 0.004$
FRICH	$0.94 - 0.89$
	$0.89 - 0.82$

Table 6.4: Angular acceptance for intervals i in the Barrel RICH and in the Forward RICH.

The coefficient w_i takes into account the thrust axis polar angle distribution in each bin i and is evaluated according to (6.12), substituting the quark polar angle θ by the polar angle of the thrust axis θ_j :

$$w_i = \frac{8}{3}\,\frac{1}{n_i}\sum_{j=1}^{n_i}\frac{\cos\theta_j}{1+\cos^2\theta_j} \tag{6.16}$$

where n_i is the number of events in the bin i.

Finally, the experimental charged kaon asymmetry A_{FB}^K will be extracted from the minimisation of the χ^2 function :

$$\chi^2 = \sum_{i=1}^{m}\left(\frac{w_i\,A_{FB}^K - A_i^{obs}}{\sigma_i}\right)^2 \tag{6.17}$$

where w_i are the coefficients defined above, σ_i is the statistical error on the observed asymmetry A_i^{obs} and i runs over the m bins (corresponding to the mirrors) in $\cos\theta_K$.

6.5.2 Correction for the contamination

The measured asymmetry A_i^K of the events with a kaon identified in the i-th angular interval has to be corrected for the contamination of our kaon sample : the presence of 'fake' kaons will modify the asymmetry measured on events with only 'correctly identified' or 'true' kaon. We will see that these 'fake' kaons are mainly pions coming from the fragmentation which are thus produced with a relatively small asymmetry and which tends therefore

to reduce the asymmetry measured compared to the correct (or 'true') one. The asymmetry corrected for this effect A_i^{corr} is thus obtained by :

$$A_i^{corr} = \frac{A_i^K - (1 - P_i^K)A^{bckg}}{P_i^K} \tag{6.18}$$

where P_i^K is the purity of our kaon sample in the angular interval i and A^{bckg} is the asymmetry for the misidentified particles (mainly pions).

Kaon identification purity evaluation

The kaon identification purity ($\mathcal{P}_K^K$) is defined (see equation 5.14) as the fraction of 'true' kaons identified as kaons in the sample of identified kaons :

$$\mathcal{P}_K^K \equiv P^K = \frac{\text{Numb. of 'true' } K \text{ identified as } K}{\text{Total numb. of identified } K} \tag{6.19}$$

More precisely, it can be written as a function of the 'efficiencies' $\mathcal{E}_X^K$ to identify a charged particle $X = e$, μ, $\pi^\pm$, $K^\pm$, p as a charged kaon $K^\pm$ and of the numbers of charged particles N_X present in the sample on which the identification procedure will be applied :

$$P^K = \frac{\mathcal{E}_K^K N_K}{\sum_X \mathcal{E}_X^K N_X} \tag{6.20}$$

in the following, the 'efficiencies' $\mathcal{E}_X^K$ with $X \neq K$ will be called misidentification efficiencies.
In figure 6.8, we show the composition of our sample of identified $K^\pm$ as a function of the particle momentum as it is obtained from the full DELPHI simulation. We see that the major contamination of our sample comes from misidentified pions (the contribution of the electrons and muons is less than 1%) and is almost constant in the momentum window useful for our analysis. Equation 6.21 can thus be developed as :

$$P^K \simeq \frac{\mathcal{E}_K^K N_K}{\mathcal{E}_K^K N_K + \mathcal{E}_\pi^K N_\pi} \tag{6.21}$$

Extensive checks have been made to control the consistency between real data and simulation and various detailed comparisons between real data and simulated data are shown in chapter 5, last section.
P^K was evaluated by simulation as justified by the following considerations :

• **Evaluation of N_K and N_π.**
Different studies about the production of charged hadrons at the Z^0 resonance have already been published from LEP experiments [8]. In the momentum range of interest for our analysis, they show discrepancies, of the order of 20% for charged kaons, between experimental results and predictions from theoretical hadronization models, including JETSET 7.3 PS. In [9] it is demonstrated that this difference comes mainly from an unsatisfactory description of the production of the charged kaons in heavy flavour events mainly due to the important uncertainties on the production rates of charged kaons from the decays of hadrons with b and c quarks.
Until now, the DELPHI collaboration has provided the unique measurement of the inclusive production of $K^\pm$ in B hadrons [10] : $BR(B \rightarrow K^\pm X = 0.88 \pm 0.05(stat) \pm 0.18(syst))$.
A more recent study on the comparison of the production of charged hadrons in b-quark events and uds events [11] seems to confirm indeed that the problem is mainly concentrated in heavy quark events whereas the description of the production of the charged kaons in light quark events as predicted by the JETSET 7.3 PS model (see figure 6.9) is satisfactory.

Concerning the evaluation of N_π, [11] shows that the experimental determinations are in agreement with the expectation of the theoretical model JETSET 7.3 PS (see figure 6.9).
For all these reasons, the terms N_K and N_π of equation 6.21 were therefore evaluated on simulation using the JETSET 7.3 PS Model.

• **Evaluation of $\mathcal{E}_K^K$.**
In principle, the best way to evaluate the efficiencies is by using real data. At LEP, real kaons can be obtained from a sample of mesons $\phi(1020)$ which decay into K^+K^- or from a sample of D^* decaying with production of $K^\pm$. But a reliable measurement of the kaon identification efficiency using these samples of charged kaons in the momentum region exploited in our analysis is illusive. There are two main problems :

- the first one is a problem of statistics. To select charged kaons with high momentum ($p > 10$ GeV/c), we have to use samples of $\phi(1020)$ or D^* with even higher momentum (for example, greater than 20 GeV/c in the case of the $\phi(1020)$) and a sufficient statistics is not available to perform a detailed study in function of the polar angle and the momentum of the $K^\pm$.

- the second one is a problem of event topology : the kaon identification efficiency in the RICHes depends on the event topology. The use of events with a particular topology as coming from the decay of $\phi(1020)$ or D^* leads to identification efficiencies which are not directly applicable to our case. For example, a $\phi(1020)$ with a momentum greater than 20 GeV/c decays into

two charged kaons $K^{\pm}$ with polar angles differing only by $\sim$ 16 mrad. Consequently, due to overlapping of rings, the reconstruction of the Cherenkov angles produced by these two tracks will be less efficient because of higher number of ambiguous photoelectrons.
A study about the determination of the identification efficiency of charged kaons based on the reconstruction of the invariant mass of the $\phi(1020)$ is presented in [12]. However, in the momentum region of interest for our analysis, the kaon identification efficiency integrated over the whole RICH acceptance and on the considered momentum window, has a relative error of at least 20%.
Therefore, the kaon identification efficiency was evaluated on simulation. In [13], one can find a test of the consistency of the kaon identification efficiency evaluated on real data and simulation, using the reconstruction of D^{*+} decaying into $(K^-\pi^+)\pi^+$.
The results obtained considering the whole momentum range of the kaons produced ($p > 2$ GeV/c) over the whole angular acceptance of the BRICH show a good agreement between the experimental results (82.5% $\pm$ 2.8%) and the simulation (80.7% $\pm$ 0.7%).

• **Evaluation of $\mathcal{E}_\pi^K$.**
At the end of chapter 5, we show some distributions (see figures 5.11, 5.12, 5.17, 5.18) which allow to control the consistency between data and simulation and which lead to the conclusion that the misidentification efficiency for Cherenkov angles close to saturation (pion misidentification efficiency) is underestimated.
This suggests to correct the pion misidentification efficiency $\mathcal{E}_\pi^K$ evaluated on simulation, and therefore to correct the fraction of pions in our sample of identified kaons.
In order to determine the scaling factor $\delta(\mathcal{E}_\pi^K)$ which will have to be applied on the misidentification efficiency computed on simulation $((\mathcal{E}_\pi^K)_{simulation})$ in order to reproduce the results obtained on real data $((\mathcal{E}_\pi^K)_{data})$:

$$(\mathcal{E}_\pi^K)_{data} = \delta(\mathcal{E}_\pi^K)(\mathcal{E}_\pi^K)_{simulation} \tag{6.22}$$

two distinct samples of real data were used (see figures 6.10 and 6.11) :

- muons coming from semi-leptonic decays identified by the Muon Chambers (at the momentum range of interest for our analysis, the RICH detector cannot distinguish between muons and pions) ;
- pions from reconstructed K_s^0 decays ($K_s^0 \rightarrow \pi^+\pi^-$).

These samples are not ideal :

- Again, there is a problem linked to their particular topology. Most of the muons come from the semi-leptonic decays of hadrons with b and c quarks and have therefore a large transverse momentum with respect to the jet axis to which they belong, which leads to reconstruct the average Cherenkov angle of well isolated tracks. On the other hand, at high momenta, the opening angle between the two outgoing pions coming from the decay of a K_s^0 is very small and the Cherenkov angle reconstruction is more complicated because of the pion rings overlap.
Therefore, these two samples taken separately are not considered as representative of the our kaon sample background but more as complementary in the topological point of view.

- Because of the very high background ($\pi^{\pm}/\mu$) rejection power of the kaon identification algorithm, the statistics left after the kaon identification was very small (of the order of hundred tracks) and no momentum or angular dependence of the correction to the pion misidentification efficiency could be studied. Only a global scaling factor with a notable uncertainty could thus be evaluated on each sample.

• About 10000 muons were available in the considered momentum window and the Barrel RICH angular acceptance. The purity in muons of this sample was estimated on simulation to be 92% with a contamination of pions of 4.5% and of kaons of 3%. In order to reduce as much as possible this kaon contamination, an additional cut on the loss of energy by ionization measured in the TPC was required which leads to a subsample of about 4000 muons with a residual kaon contamination of 0.67%.
The kaon identification algorithm used in our analysis was then applied and about 120 muons were wrongly called kaons. Figure 6.10 shows the comparison between the misidentification efficiencies evaluated on real data and simulation [7]. The ratio between the number of muons identified as kaons estimated on real data and simulation gives an estimation of the scaling factor :

$$\delta(\mathcal{E}_{\pi}^{K})_{\mu} = 1.4 \pm 0.2 \tag{6.23}$$

• About 2800 candidates pions coming from kinematically reconstructed K_s^0 decays were also used. The vertex corresponding to the decay of the K_s^0 was reconstructed as explained in [14]. The purity in pions of this sample was estimated on simulation to be greater than 97% with a kaon contamination of about 1.4%.
The same procedure as the one explained for the muon sample was applied

on this pion sample : about 150 pions were wrongly called kaons. Figure 6.11 shows the comparison between the misidentification efficiencies evaluated on real data and simulation [7]. The ratio between the number of pions wrongly called kaons estimated on real data and simulation gives :

$$\delta(\mathcal{E}_\pi^K)_\pi = 1.3 \pm 0.3 \tag{6.24}$$

The results found in the two samples are in agreement within the statistical errors. The weighted mean value of these two results gives :

$$\delta(\mathcal{E}_\pi^K) = 1.37 \pm 0.17 \tag{6.25}$$

Another method based on the actual average Cherenkov angle distribution is described in [16]. The Cherenkov angle distribution has two components : a Gaussian component centred around the expected Cherenkov angle for a given particle hypothesis and an almost linear shaped background term. Particles can be misidentified as kaons either because a separation of only two standard deviations with respect to the pion hypothesis is required to reject them, or because of the presence of this non-Gaussian background term. To study these effects, particles outside the pion and kaon signal regions were selected in real and simulated data. Two regions were defined (A and B, see figure 6.12) where the number of particles were counted in real data and simulation :

$$\begin{aligned} A &: \frac{\theta_{ring}^{meas} - \theta_c^\pi}{\sigma_{ring}} > 2.5 \\ B &: \frac{\theta_{ring}^{meas} - \theta_c^K}{\sigma_{ring}} > 2.5 \quad \text{and} \quad \frac{\theta_{ring}^{meas} - \theta_c^\pi}{\sigma_{ring}} < -2.5 \end{aligned} \tag{6.26}$$

An average scaling factor of 1.4 ± 0.1 in the barrel region and of 1.05 ± 0.1 in the forward region was found and was applied to the pion misidentification efficiency estimated on simulation. These scaling factors are similar for regions A and B, and compatible with the one as determined on the muon and pion samples.
After scaling up the background, for each bin in $\cos\theta_K$, the kaon purity extracted from simulated data was decreased by a factor going from 0.4% to 4.9% as a function of the polar angle (the correction factor decreases when $\mid \cos\theta_K \mid$ increases.

The kaon purity corrected this way is shown on figure 6.13 for each angular interval i.

As it can be noticed on this figure 6.13, the kaon identification purity depends strongly on the kaon polar angle. This dependence can be explained as follows : the smaller the track polar angle is,

- the longer the track inside the tracking system (TPC) is and thus the better the track reconstruction is, which gives a smaller error on the track extrapolation inside the RICH ;

- the smaller the distance that the photoelectrons have to cross inside the drift volume to reach the MWPC is. Consequently, the probability that they are absorbed during their drift and the possibility of distortions are reduced.

For all these reasons the reconstruction of the Cherenkov angle is better.
The steps between the four dots corresponding to the Forward RICH data and the Barrel RICH dots is due to the poorer tracking in the very forward region which induces a poorer Cherenkov angle reconstruction in the Forward RICH.

Background asymmetry evaluation

To correct the asymmetry for the problem of the contamination (see equation 6.18), we still have to evaluate the asymmetry of the events which constitute the background, i.e. events with a particle misidentified as a kaon, A^{bckg} in equation 6.18. For this purpose, counting the number of background events with K^+ and K^- in angular intervals on the full detector simulation is sufficient. In order to reduce the uncertainty due to the limited statistics of the simulation, A^{bckg} was computed explicitly over all quark flavours, and extracted using the relation 6.13 for the background events :

$$A^{bckg} = \sum_q \alpha_q^{bckg} \, (2c_q^{bckg} - 1) \, A_q \quad (q = d, u, s, c, b) \tag{6.27}$$

where α_q^{bckg} is the fraction of $q\bar{q}$ events with a misidentified kaon, c_q^{bckg} is the probability that the primary quark charge is correctly tagged by the misidentified kaon and A_q are the quark asymmetries. In order to reduce the statistical error, only the coefficients α_q^{bckg} and c_q^{bckg} were computed directly on the simulation, while all the quark asymmetries were fixed at their Standard Model values as predicted by the ZFITTER program[3] [15].

[3]The free parameters of the model were fixed to : the mass of the Z^0 $M_Z = 91.186$ GeV/c^2, the mass of the top quark $m_t = 175$ GeV/c^2, the mass of the Higgs boson $m_H = 300$ GeV/c^2 and the strong coupling constant $\alpha_s = 0.122$ [17].

The background asymmetry computed in this way is found to be almost negligible :

$$A^{bckg} = 0.0012 \pm 0.0016 \tag{6.28}$$

6.5.3 Material asymmetry evaluation

The hadronic cross-sections of the charged kaons are different :

$$\sigma(K^-) > \sigma(K^+) \tag{6.29}$$

which means that negatively charged kaons (K^-) are more absorbed by the detector material they have to cross before entering the RICH detectors than positively charged kaons (K^+). This induces an artificial asymmetry due to material (A^{mat}). This asymmetry is in first approximation proportional to the material length crossed and, assuming the detector made of concentrical homogeneous cylindrical shells of material, has a $(1/\sin\theta_K)$ angular dependence on the kaon polar angle and varies between 2% (in the forward region) to 0.7% (in the barrel region).
For a given angular interval i, the observed kaon asymmetry (which is, in fact, the 'true' asymmetry at the production level, i.e. before entering the detector) can be written as :

$$A_i^{obs} = \frac{N_i^0(K^-) - N_i^0(K^+)}{N_i^0(K^-) + N_i^0(K^+)} \tag{6.30}$$

where $N_i^0(K^-)$ and $N_i^0(K^+)$ are the numbers of K^- and K^+ really produced in the angular interval i.
These numbers are related to the numbers of kaons detected in a bin i appearing in equation 6.14 by :

$$\begin{aligned} N_K^-(\cos\theta_i) &= \epsilon_i^{K^-}\ N_i^0(K^-) \\ N_K^+(\cos\theta_i) &= \epsilon_i^{K^+}\ N_i^0(K^+) \end{aligned} \tag{6.31}$$

with ϵ^{K^-} (ϵ^{K^+}) the probability for a K^- (K^+) not to have interacted before getting out of the RICH detectors (i.e. the probability to reach the OD (for the barrel analysis) or the FCB (for the forward analysis) without interacting with the detector material).
Defining, for a given interval i in $\cos\theta_K$, the ratio r_i between these probabilities :

$$r_i = \epsilon_i^{K^+}/\epsilon_i^{K^-} \tag{6.32}$$

the observed asymmetry becomes :

$$\begin{aligned} A_i^{obs} &= \frac{(r_i - 1) + A_i^{corr}(r_i + 1)}{(r_i + 1) + A_i^{corr}(r_i - 1)} \\ &\simeq A_i^{corr} + \frac{1}{2}(r_i - 1) \quad \text{for} \mid r_i - 1 \mid << \end{aligned} \tag{6.33}$$

where A_i^{corr} is the asymmetry corrected for the contamination in the angular interval i or, in other words, the asymmetry of the events with the charged kaon correctly identified (see section 6.5.2).
For the angular interval i, the material asymmetry A_i^{mat} is therefore defined as :

$$A_i^{mat} = \frac{1}{2}(r_i - 1) \tag{6.34}$$

and was evaluated on a sample of 2.4×10^6 hadronic events simulated through the full DELPHI simulation.
For each angular interval i, the ratios :

$$\begin{aligned} \epsilon_i^{K^-} &= \frac{N_K^-(\cos\theta_i)}{N_i^0(K^-)} \\ \epsilon_i^{K^+} &= \frac{N_K^+(\cos\theta_i)}{N_i^0(K^+)} \end{aligned} \tag{6.35}$$

between the number of K^- and K^+ at the production level and the number of charged kaons entering the OD (for the barrel region) or the FCB (for the forward region) are computed and the correction factors r_i evaluated. To reduce the statistical uncertainty on the material asymmetry, a fit was done to the distribution of the material asymmetry versus the number of charged kaons interacting with the material.
The material asymmetry as a function of cosine of the kaon polar angle is shown on figure 6.14, it ranges from 2% to 0.7%. The systematic error on A^{mat} is 10% mainly coming from the uncertainties in the difference in the nuclear cross-sections of p(n)K^+ and p(n)K^-.
In order to reduce the statistical uncertainty on A_i^{mat} obtained as explained above, another technique to evaluate the asymmetry due to material is presented in [16]. It is based on a fast analytical calculation using the DELPHI database which contained the description of the material of the various components of the detectors and the nuclear interaction cross-section calculation of the full simulation for a grid of points in the 3-dimensional space of K momenta, polar and azimuthal angles. A weighted mean according to the

distributions of these three variables was computed for each mirror. The statistical error on this procedure is negligible. Moreover, the method allows to evaluate the sensibility of this correction to the pK cross-section parametrisation by using an alternative one given in [3] : this uncertainty source was found to be 0.0015 on average.

6.5.4 Charged kaon asymmetry: results

Due to the different event selection for the barrel analysis and the forward analysis, the experimental charged kaon asymmetry A_{FB}^{K} was evaluated separately for each analysis (barrel and forward).
The procedure described in section 6.5.1 allows, for each polar angle interval i, to compute the observed asymmetry A_i^{obs}, corrected for the charged kaon purity and the interaction of the $K^{\pm}$ with the detector material. The minimisation of the function (6.17) gives the following values for the experimental charged kaon asymmetries :

Barrel analysis

$$A_{FB}^{K} = 0.0460 \pm 0.0064(stat.) \pm 0.0003(syst.) \tag{6.36}$$

for all mirrors, with a χ^2 per degree of freedom of : $\chi^2/11 = 0.65$ (see figure 6.15).

To check the consistency of the measurement, the fitting procedure was repeated for each hemisphere separately :

$$\begin{aligned} A_{FB}^{K}(z>0) &= 0.0466 \pm 0.0088(stat.) \\ A_{FB}^{K}(z<0) &= 0.0453 \pm 0.0093(stat.) \end{aligned} \tag{6.37}$$

which are compatible with each other within one standard deviation and which therefore demonstrate, as expected, the compatibility between the experimental asymmetries evaluated in each hemisphere separately. The charged kaon asymmetry (A_i^{obs}) versus the weights w_i are shown on figure 6.16 separately for each hemisphere. The solid line show the result of the fit and the dashed lines represent one standard deviation. The χ^2 per degree of freedom are $\chi^2/5 = 0.51$ for $z > 0$ and $\chi^2/5 = 0.93$ for $z < 0$.

Forward analysis

$$A_{FB}^{K} = 0.031 \pm 0.011(stat.) \pm 0.0006(syst.) \quad (6.38)$$

with a χ^2 per degree of freedom of $\chi^2/3 = 1.42$ (see figure 6.17).
The contributions to the systematic error are listed in table 6.5 for both analysis. They come from the the propagation of the systematic error due to the correction coefficients for the kaon purity and the interaction with detector material.
As it is expected, the charged kaon asymmetry evaluated separately in the

Contribution to the systematic error on A_{FB}^{K} ($\times 10^{-4}$)	Barrel	Forward
Kaon sample contamination	0.30	0.50
K^+/K^- different interaction with material	0.22	0.70
A^{bckg}	2.60	5.70
Total	2.63	5.80

Table 6.5: Contributions to the systematic error on the charged kaon asymmetry for the barrel analysis and for the forward analysis.

barrel region and in the forward region are compatible with each other within one standard deviation.

6.6 s-quark asymmetry

6.6.1 From the kaon asymmetry to the s-quark asymmetry

The kaon asymmetry measured experimentally (A_{FB}^{K}) is in fact a statistical average of the kaon asymmetries from all quark flavour asymmetries weighted by a Monte Carlo estimated factor. This factor depends on the fractions of kaons produced in each flavour event and on the probability to correctly tag the primary quark charge. Accordingly, the experimental kaon asymmetry can be expressed in terms of the $q\bar{q}$ asymmetries as :

$$A_{FB}^{K} = \sum_{q} \alpha_q \, (2c_q - 1) \, A_q \quad (q = d, u, s, c, b) \quad (6.39)$$

where :

- α_q are defined as the fractions of kaons produced in the events of flavour q. They can be expressed in terms of the original fractions of $q\bar{q}$ events in the selected hadronic sample $R_q = \Gamma_{q\bar{q}}/\Gamma_{had}$ and of the flavour selection efficiencies ϵ_q :

$$\alpha_q = \frac{R_q \epsilon_q}{\sum_{f=d,u,s,c,b} R_f \epsilon_f} \tag{6.40}$$

  The terms appearing in equation 6.40 were evaluated by simulation. R_q was calculated thanks to the ZFITTER program with the values of the input parameters fixed at the same values than for the evaluation of the A_q (see section 6.5.2). To take into account the experimental effects of the detector acceptance and efficiency, the ϵ_q were evaluated with JETSET PS 7.3 and the full DELPHI simulation.

- c_q are defined as the probabilities that the sign of the charge of the identified kaon points out correctly the event hemisphere, as defined by the reconstructed thrust axis, containing the primary quark after the QCD parton cascade. With this definition, it is possible to restrict the corrections coming from the perturbative QCD phase of the hadronization only to the primary quark direction estimator. The c_q were evaluated with JETSET PS 7.3 and the full DELPHI simulation.

As it can be noticed in table 6.6, the evaluation of α_q gives different values following the analysis region (barrel or forward) because they depend on the flavour selection efficiencies ϵ_q which are different for each analysis, while the values of the c_q are, as expected, independent of the data treated.

Flavour	Barrel		Forward	
	α_q	c_q	α_q	c_q
d	0.1425 ± 0.0013	0.328 ± 0.004	0.1038 ± 0.0021	0.329 ± 0.009
u	0.1356 ± 0.0012	0.264 ± 0.004	0.0979 ± 0.0020	0.246 ± 0.009
s	0.5523 ± 0.0029	0.868 ± 0.002	0.4290 ± 0.0048	0.878 ± 0.003
c	0.1600 ± 0.0013	0.835 ± 0.003	0.2331 ± 0.0033	0.859 ± 0.005
b	0.0091 ± 0.0003	0.809 ± 0.013	0.1359 ± 0.0024	0.809 ± 0.007

Table 6.6: Computed values for the flavour selected fractions (α_q) and quark charge identification efficiencies (c_q) for the Barrel and the Forward regions. The errors given are due to the limited simulation statistics.

From equation 6.39 we then extract the measured s-quark asymmetry A_s.

To obtain the pole asymmetry $A^0_{s\bar{s}}$ from this measured asymmetry, a few corrections have to be applied :

- **QED correction.**
  Correction due to initial state radiation : the emission of a photon in the initial state has the effect of reducing the centre of mass energy of the system e^+e^-. Due to the fast evolution of the cross-section in function of the energy around the Z^0 resonance peak, this correction induces a modification of the asymmetry which varies rapidly around the peak (see figure 4.2) ;

- Effects of the **energy shift** .
  The centre of mass energy at which LEP was running deviates somewhat from $\sqrt{s} = M_Z$;

- Correction due to γ **exchange and** γZ **interference.**

These corrections $((\delta A_q)_i)$ have been calculated for each flavour q using the ZFITTER program according to the procedure described in [17]. They are generally small for quarks. The corrected asymmetry $(A^0_{q\bar{q}})$ can be written as :

$$A^0_{q\bar{q}} = A_q + \sum_i (\delta A_q)_i \tag{6.41}$$

The values of the correction coefficients $(\delta A_q)_i$ are given in table 6.7.

Flavour	QED	$\sqrt{s} = M_Z$	$\gamma, \gamma Z$
d	0.0042	-0.0015	-0.0003
u	0.0108	-0.0040	-0.0007
s	0.0042	-0.0015	-0.0003
c	0.0108	-0.0040	-0.0007
b	0.0042	-0.0015	-0.0003

Table 6.7: Correction coefficients $((\delta A_q)_i)$ calculated with the ZFITTER program as described in [17].

- **QCD correction.**
  This is the correction due to the fact that the estimated quark direction using the thrust axis differs from the true one because of gluon emission, hadronization and decays, and experimental reconstruction problems of the thrust axis (undetected particles, resolution of the charged particle momentum and neutral particle showers energy).

It has been estimated for each flavour according to the procedure described in [18] using the JETSET PS 7.3 simulation program.
The pole asymmetry $A^0_{q\bar{q}}$ is finally obtained from the measured asymmetry A_q according to the following expression :

$$A^0_{q\bar{q}} = (A_q(1 + C_q^{thrust}) + \sum_i (\delta A_q)_i) \tag{6.42}$$

where C_q^{thrust} are terms which take into account the QCD correction explained above. They were computed according to the procedure described in [18] using JETSET PS 7.3 and the full DELPHI detector simulation.
On figure 6.18, we show the difference between the polar angle of the primary quark and the polar angle made by the measured thrust axis (oriented in the direction of the primary quark). The values of the C_q^{thrust} coefficients as computed on simulation are given in table 6.8. The errors are due to the limited simulation statistics. Since only heavy flavour asymmetries are

Flavour	C_q^{thrust}	
	Barrel	Forward
d	-0.029 ± 0.006	-0.013 ± 0.004
u	-0.029 ± 0.006	-0.018 ± 0.005
s	-0.025 ± 0.003	-0.012 ± 0.002
c	-0.020 ± 0.005	-0.011 ± 0.003
b	-0.035 ± 0.015	-0.005 ± 0.002

Table 6.8: Correction coefficients for bias on primary quark direction due to QCD gluon emission, fragmentation and thrust axis reconstruction when the thrust axis direction is used as an estimator.

experimentally known, assumptions on light quarks asymmetries must be made, according to the Standard Model predictions :

$$\begin{aligned} A^0_{s\bar{s}} &= A^0_{d\bar{d}} \\ A^0_{u\bar{u}} &= \lambda A^0_{d\bar{d}} \end{aligned} \tag{6.43}$$

with $\lambda = 0.7122$, the Standard Model prediction computed from ZFITTER. This choice has been done in order to use the measurement of $A^0_{s\bar{s}}$ as a check of the coupling universality in the light quark sector (the Standard Model predicts the same asymmetry for b and s quark asymmetry) since the heavy flavour contribution is computed from independent measurements. The heavy flavour quark asymmetries are taken from their own experimental

value [19] :

$$\begin{aligned} A^0_{b\bar{b}} &= 0.0979 \pm 0.0023 \\ A^0_{c\bar{c}} &= 0.0735 \pm 0.0048 \end{aligned} \tag{6.44}$$

The careful analysis described above leads to the following results :

$$\begin{aligned} A^0_{s\bar{s}} &= 0.127 \pm 0.021(stat.) \quad \text{for the Barrel analysis} \\ A^0_{s\bar{s}} &= 0.052 \pm 0.045(stat.) \quad \text{for the Forward analysis} \end{aligned} \tag{6.45}$$

which taking into account only the statistical errors (coming from the propagation of the statistical errors on A^K_{FB}) differ by about 1.5σ. Before going further comparing these two measurements and drawing definite conclusion, the systematic errors which are different for the Barrel and the Forward analysis should be evaluated.

Let us notice that we have checked that these results are stable for a variation of the λ obtained by varying the values of m_H and m_{top} used in the ZFITTER program.

6.6.2 Systematic errors

Sine the extraction of the $s\bar{s}$ asymmetry from the observed $K^{\pm}$ asymmetry requires the evaluation of various quantities by simulation of the fragmentation model and of the response of the DELPHI detector, the systematic uncertainties on $A^0_{s\bar{s}}$ (6.45) can come from the following different sources : the limited simulation statistics, the experimental method, the input quark asymmetries, and the parametrisation of the fragmentation model (JETSET 7.3 input parameters). Among them, all but the fragmentation model uncertainties will be treated under the topic 'experimental systematic errors'.
Due to the different event selection used they have been studied and evaluated separately in the Barrel and in the Forward regions. The difference is given by the sources of errors specifically connected with the Brown and Frank procedure and by the different amount of $b\bar{b}$ events, almost negligible in the Barrel while sizeable in the Forward.
The detailed breakdown of all the error sources discussed and of their specific effect on $A^0_{s\bar{s}}$ is given in table 6.9.

A. Experimental systematic errors

- The **uncertainties on $A^0_{b\bar{b}}$ and $A^0_{c\bar{c}}$** (6.44) were propagated, taking into account the 10% correlation between these two quantities. The

resulting uncertainties on $A^0_{s\bar{s}}$ are of 0.0018 in the Barrel region and of 0.0035 in the Forward region.

- The **systematic errors on the experimental asymmetry** A^K_{FB} listed in table 6.5 : systematic uncertainty due to the different absorption of the K^+ and K^- with the material and the systematic uncertainty on the correction for the contamination (which is due to the uncertainty on the correction of the misidentification of the kaons using the simulation), induce uncertainties on $A^0_{s\bar{s}}$ of 0.0009 and 0.0023 in the Barrel and in the Forward region, respectively.

- The **error due to the limited simulation statistics** for the evaluation of the coefficients α_q and c_q was found to be 0.0011 and 0.0044 for the Barrel and the Forward region respectively.

- The **uncertainty due to the momentum resolution** of the selected $K^\pm$. In principle, this effect could be studied independently of the simulation by varying the lower and upper limits of the momentum window of a quantity corresponding to the momentum resolution in the region around these limits. However, this approach presents two disadvantages :

  - first, the global variation of the momentum window would overestimate the effect of the migration and thus would tend to overestimate the error ;

  - secondly, it does not allow a study of the possible migration inside the momentum window used. Moreover, the uncertainty on the 'true' momentum of the charged kaon presents an intrinsic limit due to the threshold of the emission of the Cherenkov light in the gas radiator. Therefore, the effect of the resolution on the $K^\pm$ momentum was computed with the full DELPHI simulation, selecting events according to the true $K^\pm$ momentum instead of the reconstructed one and evaluating the corresponding variation induced on the coefficients α_q and c_q. The obtained systematic errors on $A^0_{s\bar{s}}$ is 0.0011 and 0.0044 in the Barrel and in the Forward region, respectively.

- In the Barrel region, where the Brown and Frank algorithm was used, a source of error is given by the quality of the simulation to describe the significance of the tracks which are used to compute the probability P^+_E. An estimate of this error is obtained by comparing the probability computed using negative impact parameters P^-_E in the sample with the selection cut $P^+_E > 0.15$, where the contribution of heavy flavours and

secondary decay vertices to P_E^- is highly suppressed. The difference between the selection efficiencies computed using real and simulated distribution of P_E^- is used as an estimate on the **uncertainty coming from the detector resolution on impact parameters** which is found to be 0.00004.

B. Simulation model uncertainties

The uncertainties which come from the Monte Carlo modelling (see section 2.3.1) can be split into three classes which will be detailed in the following : (1) systematic uncertainties from charm quarks, (2) bottom quarks and (3) light quarks. They were evaluated following different approaches for the heavy flavour sector (classes (1) and (2)) and the light flavour sector (class (3)). This is due to the following considerations :

- The $K^{\pm}$ production in the selected momentum range in the light flavours is strongly dominated by the fragmentation process, while in the heavy flavour sector it is due mainly to the weak decays of the hadrons with b and c quarks. Therefore, the Brown and Frank procedure does not affect significantly the $K^{\pm}$ production in the light flavour sector while it introduces biases in the heavy one.

- Moreover, in the light flavour sector, the fragmentation model parameters play a dominant role while in the heavy flavour sector an important source of theoretical errors is given by the uncertainties in the D and B mesons branching ratios into channels with $K^{\pm}$.

- **(1) For charm quarks** the following quantities related to the fragmentation were taken into account: the fractions of different charmed hadrons $f(D^{\pm})$, $f(D_s)$, $f(c_{bar})$ (taking into account the correlations among the fractions), the average decay multiplicity of c hadrons, the charm quark fragmentation (through the mean energy taken by the charmed hadrons $< x_c >$) and (for the Barrel region only) the D meson lifetimes. The uncertainties in these quantities were taken from [18] and treated as described in this reference. Another source of error is coming from the uncertainties on the branching ratios of charmed particles into kaons BR($D \to K_s^0 X$), BR($D^0 \to K^- X$), BR($D^0 \to K^+ X$), BR($D^+ \to K^- X$), BR($D^+ \to K^+ X$), BR($D_s \to K^- X$), BR($D_s \to K^+ X$). These various hadrons with a c-quark which could have been produced have different probability to contribute to the event selection from the point of view of the Brown and Frank algorithm. The decays of these hadrons can produce charged kaons $K^{\pm}$ which obviously influences the selection efficiency and the correlation between the charge of

the $K^{\pm}$ and the charge of the primary quark.
The values of these branching ratios quoted in [3] were used.
In order to evaluate the corresponding uncertainties on $A^0_{s\bar{s}}$, the simulated events were re-weighted according to the uncertainties in all the observables listed, and the variations in $A^0_{s\bar{s}}$ due to the variations in the coefficients α_q and c_q were used as an estimate of the systematic error due to this sources.

- **(2) For bottom quarks** a procedure similar to the one used for the c quark was followed. The study has been done in a slightly different way for the Barrel analysis and the Forward analysis, due to the significant difference in the b-quark content of the selected sample of events.
For the Barrel analysis the following quantities related to the b-quark fragmentation were considered: the B lifetime, B hadron decay multiplicity, the fragmentation function of b-quark (i.e. $< x_b >$), where the range of variations quoted in [18] were used. In addition the uncertainty in the branching ratio of bottom quarks into kaons BR($b \to K^{\pm}X$) was propagated to the selection efficiency, and the uncertainty in the average of the branching ratios of the mixture $B^{\pm} - B^0$ in K^+ and K^- separately BR($B^{\pm} - B^0 \to K^+/K^-X$) was propagated to the charge selection efficiency c_b.
For the Forward analysis, due to the absence of the Brown and Frank mechanism, no error from the B lifetime was considered. Furthermore, the error on c_q was studied in larger detail, due to the bigger importance of this coefficient in the final result. The influence of the uncertainties in the fractions of $B^{\pm}$, B^0, B_s and bottom hadrons as computed in [3] on c_b were taken into account. Moreover the uncertainties on the individual branching ratios BR($B^{\pm} \to K^+X$), BR($B^{\pm} \to K^-X$), BR($B^0 \to K^+X$) and BR($B^0 \to K^-X$) as measured in [20] instead were used. In events with D_s coming from a B_s, the error on the branching ratios of D_s decays into $K^{\pm}$ was considered.

  Another possible source of errors is the gluon splitting mechanism which leads to c and b quark production in the fragmentation process. The $g \to c\bar{c}$ and $g \to b\bar{b}$ rates were conservatively varied by 50% in order to evaluate the effects on $A^0_{s\bar{s}}$.

- **(3) In the light quark sector** the Brown and Frank mechanism applied in the Barrel region implies that the light quark selection has uncertainties due to the presence of secondary vertices (due to photon conversion and hyperon decay) which tend to bias P_E^+ towards low val-

ues. Following the same approach than the one used in [21], the rate of photon conversion was varied by 30% and that of K_s^0 and Λ decays of 10%.
The other important source of errors for the light quarks is due to the model which was used to describe the $K^{\pm}$ production in $u\bar{u}$, $d\bar{d}$, $s\bar{s}$ and to compute the flavour selection efficiencies ϵ_q and the charge selection efficiencies c_q for these events. The JETSET PS model which was used depends on several phenomenological input parameters which must be adjusted in order to reproduce the real data. The physical phenomenon studied being the production of fast $K^{\pm}$, only the 10 Lund parameters to which the $K^{\pm}$ is most sensitive (following the study described in [6]) where considered, e.g. the fundamental fragmentation parameters $a, \sigma_q, \Lambda_{QCD}, Q_0$, the s-quark production suppression γ_s, the diquark production suppression $\frac{P(qq)}{P(q)}$, and the rate of probability of production of the different multiplets of particles $P(^1S_0), P(^3S_1), P(^1S_0), P(^3S_1)$ [4]. These parameters which describe the fragmentation process were varied (see Appendix B) applying the method explained in [6] and [22] and the corresponding uncertainties on the coefficients ϵ_d,c_d,ϵ_u,c_u,ϵ_s,c_s were evaluated both in the Barrel and the Forward region (see table 6.9).

The total systematic error on the $s\bar{s}$ pole asymmetry $A_{s\bar{s}}^0$ is found to be 0.0043 for the Barrel analysis and 0.0087 for the Forward analysis.

Finally, the results obtained for $A_{s\bar{s}}^0$ as determined in the Barrel and in the Forward regions with systematic errors are :

$$\begin{aligned} A_{s\bar{s}}^0 &= 0.127 \pm 0.021(stat.) \pm 0.0043(syst.) \quad \text{for the Barrel anal.} \\ A_{s\bar{s}}^0 &= 0.052 \pm 0.045(stat.) \pm 0.0087(syst.) \quad \text{for the Forward anal.} \end{aligned} \tag{6.46}$$

which are compatible within one standard deviation.

Combining these two asymmetries, we get the following result for $A_{s\bar{s}}^0$:

$$A_{s\bar{s}}^0 = 0.114 \pm 0.019(stat.) \pm 0.005(syst.) \tag{6.47}$$

[4] In JETSET, mesons are produced according to their quark contents in the six multiplets with smallest mass : if L is the orbital angular momentum of the quark, S is its spin, $J = L + S$ is the total angular momentum, using the notation $^{2s+1}L_S$ commonly applied in atomic physics, these six states are $^1S_0$, $^3S_0$, $^1P_1$, $^3P_0$, $^3P_1$ and $^3P_2$.

The conclusions concerning our result are summarize in the next chapter.

Systematic source	$\delta A^0_{s\bar{s}}$ ($\times 10^{-4}$)	
	Barrel	Forward
$A^0_{c\bar{c}}$ and $A^0_{b\bar{b}}$	17.6	34.5
Experimental asymmetry fit	8.7	22.5
Simulation statistics	11.4	43.9
$K^{\pm}$ momentum resolution	8.4	6.2
Impact parameters resolution	0.4	-
$f(D^{\pm}) = 0.233 \pm 0.028$	0.3	0.6
$f(D_s) = 0.102 \pm 0.037$	0.5	1.0
$f(c_{bar}) = 0.065 \pm 0.029$	0.8	3.6
c hadrons decay multiplicity $= 2.35 \pm 0.06$	6.7	2.4
$< x_c >= 0.484 \pm 0.008$ (charm fragmentation)	10.7	35.5
BR$(D \to K^0_s X) = 0.46 \pm 0.06$	2.2	5.8
D mesons lifetimes	0.1	-
BR$(D^0 \to K^- X) = 53 \pm 4\%$	5.4	0.6
BR$(D^0 \to K^+ X) = 3.4 + 0.6 - 0.4\%$	2.8	4.6
BR$(D^+ \to K^- X) = 24.2 \pm 2.8\%$	1.0	1.1
BR$(D^+ \to K^+ X) = 5.8 \pm 1.4\%$	4.4	8.9
BR$(D_s \to K^- X) = 13 + 14 - 12\%$	2.0	1.1
BR$(D_s \to K^+ X) = 20 + 18 - 14\%$	18.6	33.5
B hadron decay multiplicity $= 5.73 \pm 0.35$	0.1	10.8
$< x_b >= 0.702 \pm 0.008$ (bottom fragmentation)	0.1	16.3
B hadrons lifetimes	0.1	-
BR$(b \to K^{\pm} X) = 88 \pm 19\%$	0.6	26.6
BR$(B^{\pm} - B^0 \to K^+/K^- X)$	0.1	-
$f(B^{\pm}) = 37.8 \pm 2.2\%$	-	1.4
$f(B^0) = 37.8 \pm 2.2\%$	-	1.4
$f(B_s) = 11.2 \pm 1.9\%$	-	4.0
$f(b_{bar}) = 13.2 \pm 4.1\%$	-	7.6
BR$(B^0 \to K^- X) = 0.73 \pm 0.08$	-	3.9
BR$(B^0 \to K^+ X) = 0.13 \pm 0.04$	-	0.7
BR$(B^+ \to K^- X) = 0.58 \pm 0.08$	-	10.1
BR$(B^+ \to K^+ X) = 0.13 \pm 0.05$	-	4.8
BR$(D_s \to K^- X)$ from B_s	-	4.1
BR$(D_s \to K^+ X)$ from B_s	-	5.0
photon conversion $\pm 30\%$	1.5	-
$K^0_s(u,d,s) \pm 10\%$	0.4	-
$\Lambda(u,d,s) \pm 10\%$	0.4	-
$g \to c\bar{c} \pm 50\%$	0.6	-
$g \to b\bar{b} \pm 50\%$	0.1	-
ϵ_d	9.0	4.2
ϵ_u	14.8	11.1
ϵ_s	8.0	8.1
c_d	13.6	2.9
c_u	4.4	6.3
c_s	9.7	3.9
Total systematic error	42.7	86.5

Table 6.9: Summary of the systematic errors on the pole asymmetry of s quark measurement.

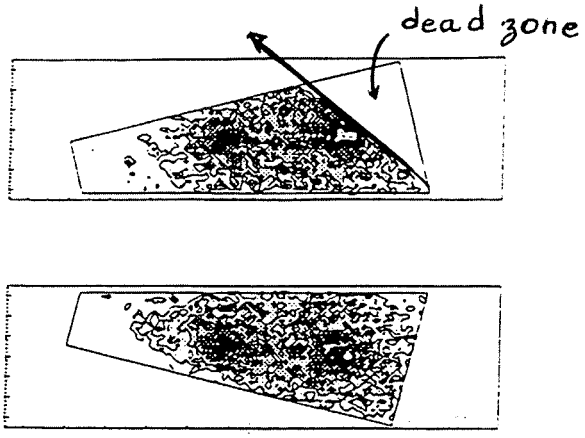

Figure 6.5: Distribution of the Cherenkov photons in the photon detector (also called driftbox) of the Forward RICH, .

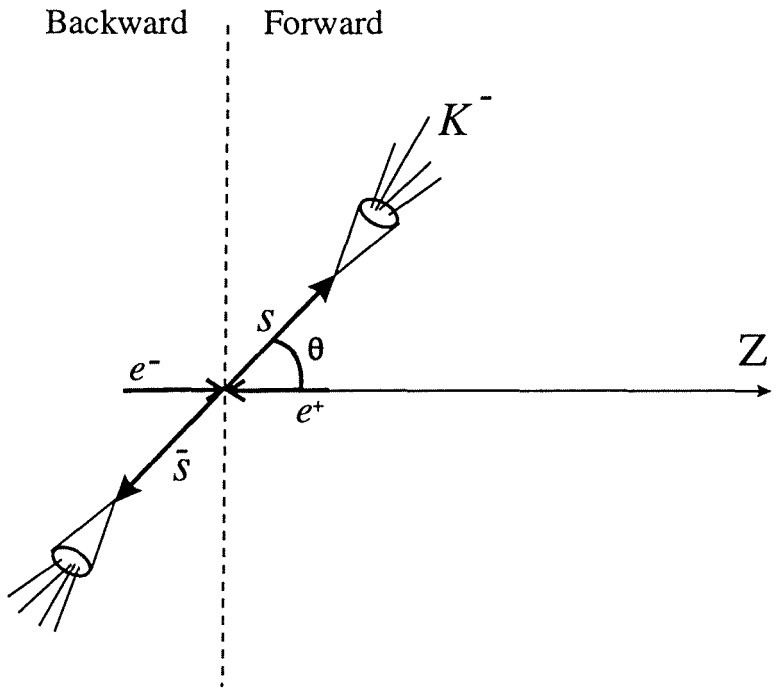

Figure 6.6: Illustration of an $s\bar{s}$ event with an identified charged kaon.

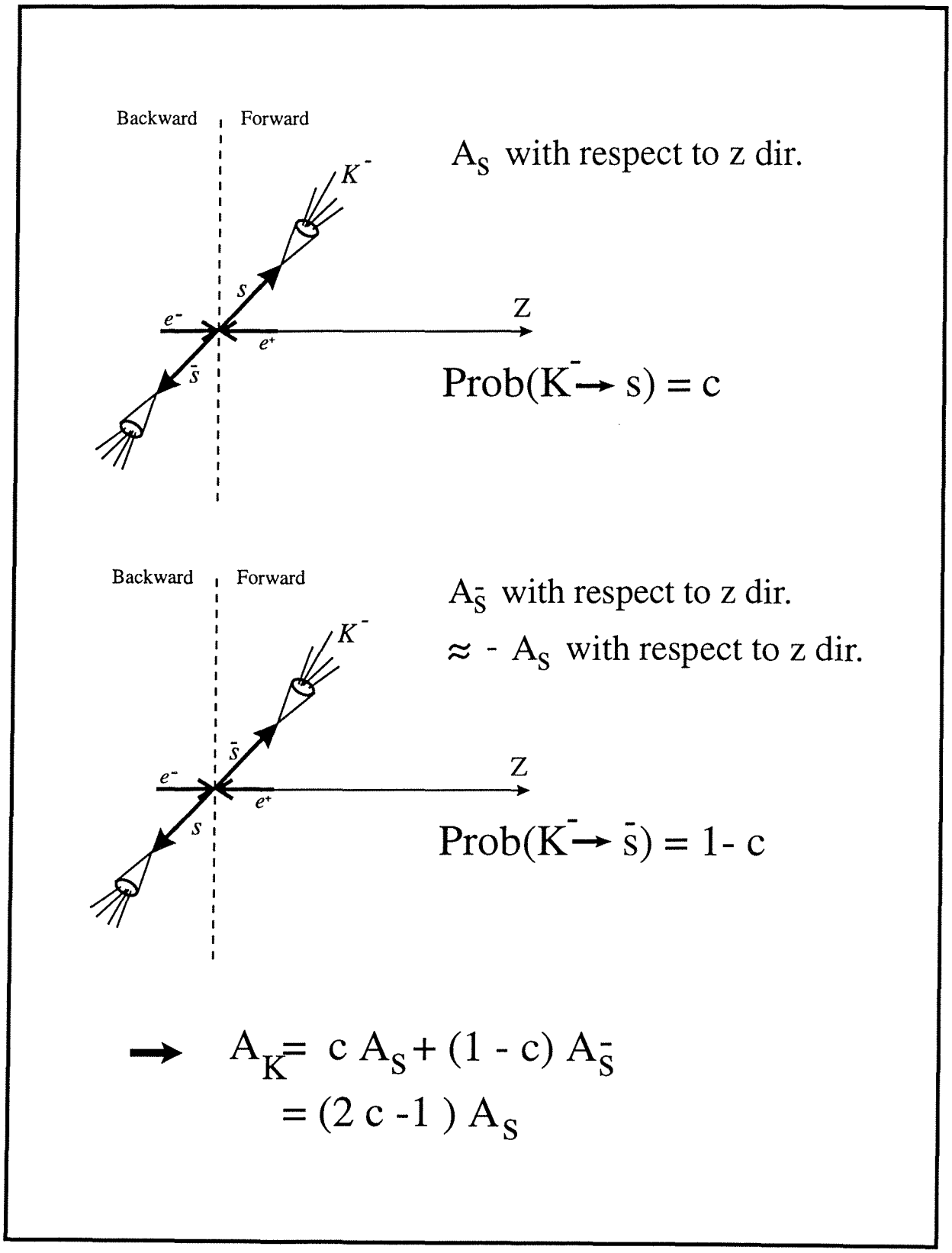

Figure 6.7: Illustration of the term (2c-1) in equation 6.13 with c the probability that a negative kaon correctly tagged an s-quark.

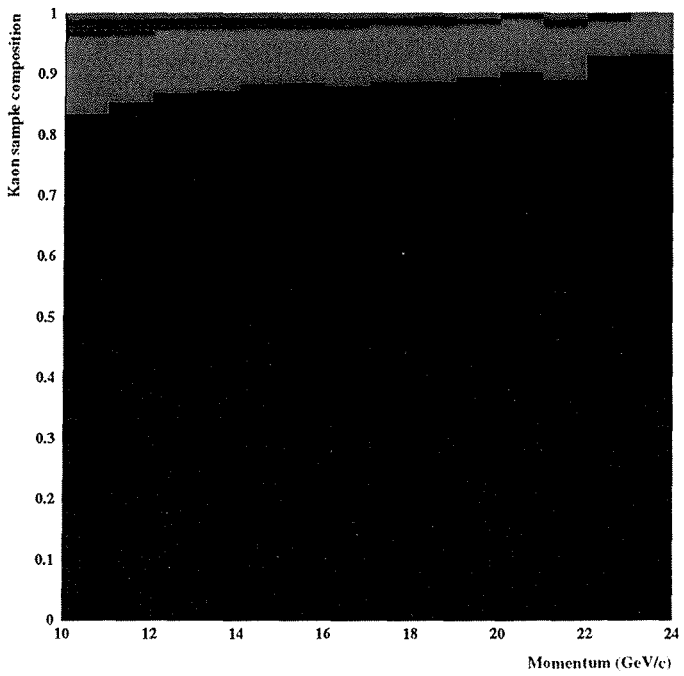

Figure 6.8: Composition of our sample of identified kaons as a function of the kaon momentum. Starting at the bottom, we show the fraction of well identified kaons, pions and protons in the Barrel region.

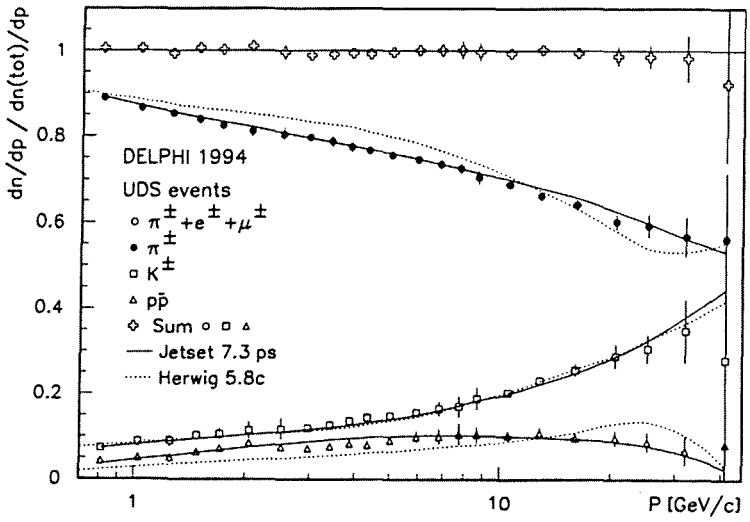

Figure 6.9: Fractions of charged particles measured in a sample of light quark events (the rejection of the b-quark events being obtained requiring the Brown and Frank probability for tracks in the total event with positive significance to be : $P_E^+ > 0.15$). We notice that the experimental spectra are in good agreement with the ones predicted by the JETSET PS 7.3 Model.

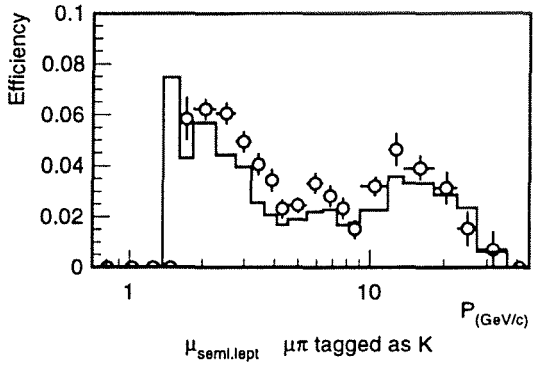

Figure 6.10: Misidentification efficiencies evaluated on data (dots) and simulation (lines) for semi-leptonic muons versus momentum (Barrel RICH).

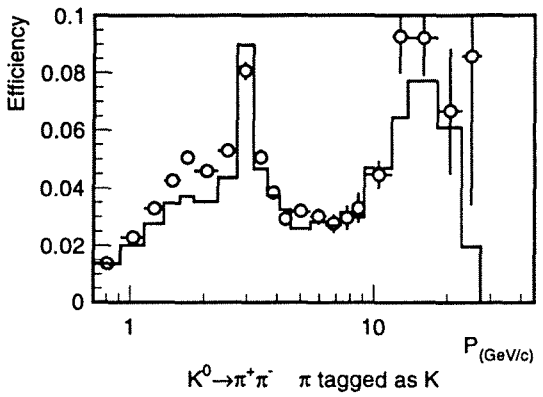

Figure 6.11: Misidentification efficiencies evaluated on data (dots) and simulation (lines) for pions from K^0 decays versus momentum (Barrel RICH).

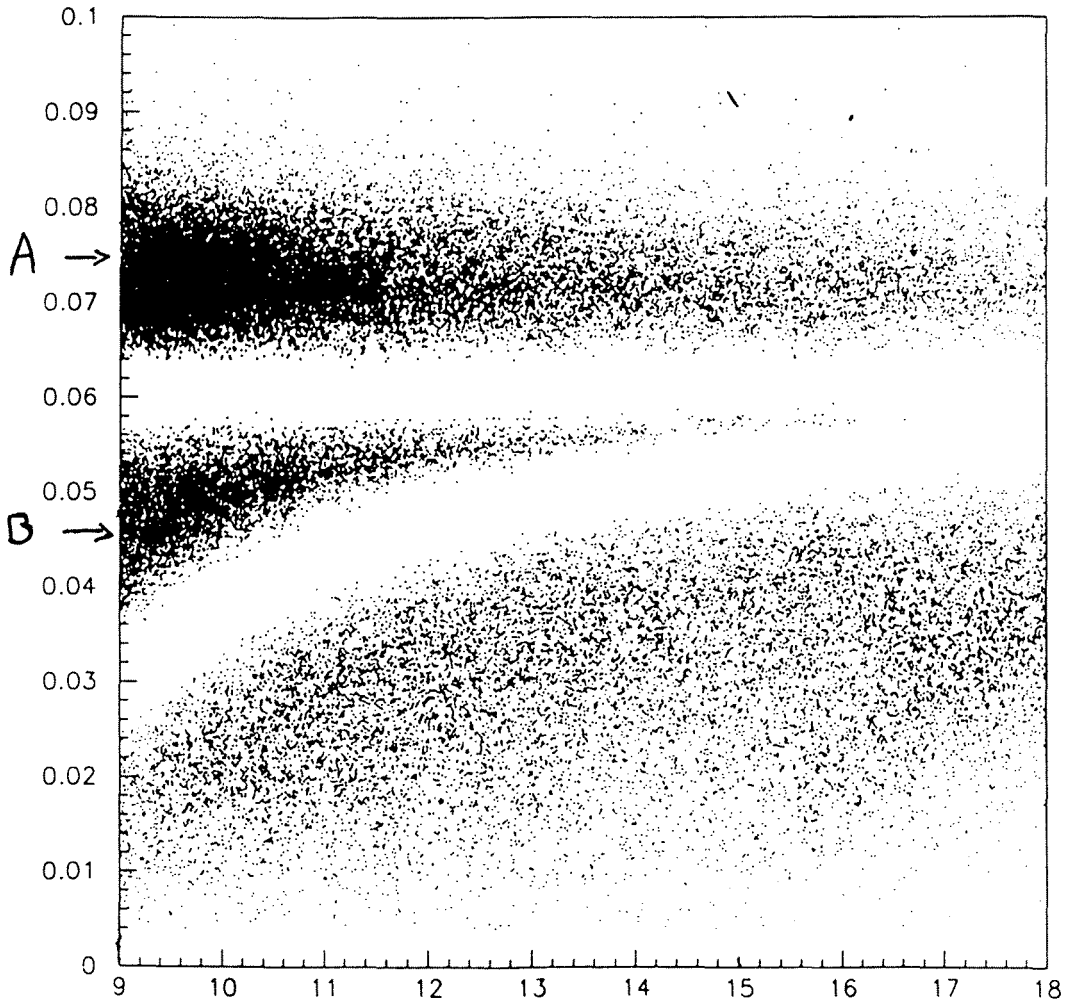

Figure 6.12: Distribution of the Cherenkov angle versus particle momentum showing the two regions of background as defined by expressions 6.26.

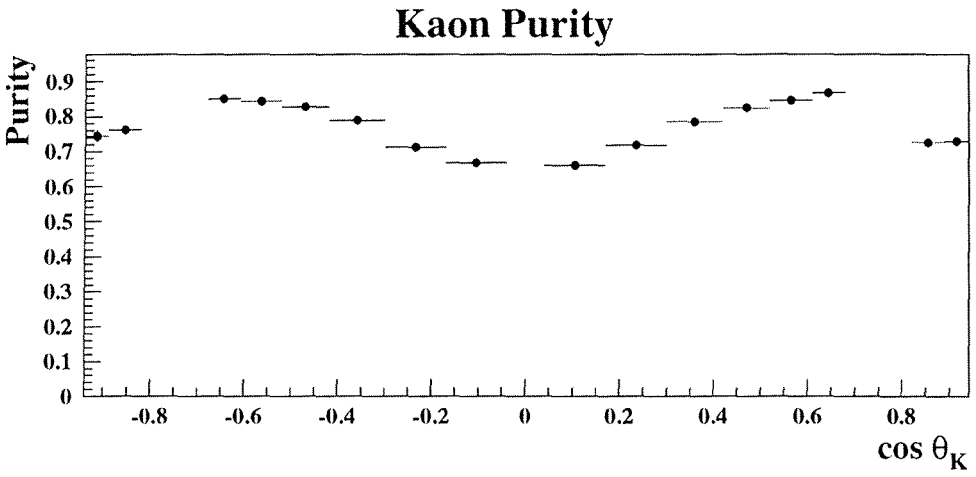

Figure 6.13: Charged kaon purity in the momentum range $10 < p < 24$ GeV/c in both RICHes as a function of the cosine of the kaon polar angle ($\cos\theta_K$).

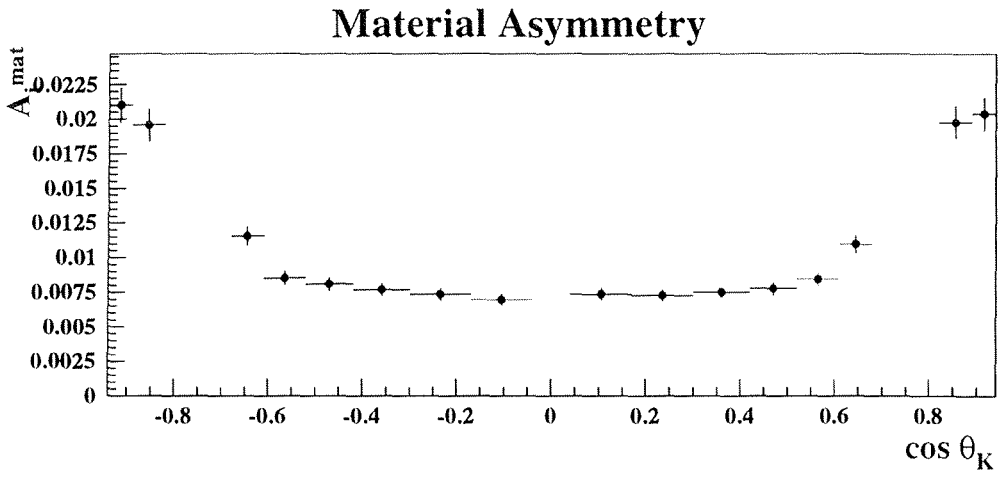

Figure 6.14: Material asymmetry as a function of the cosine of the polar angle of the kaon in both RICHes.

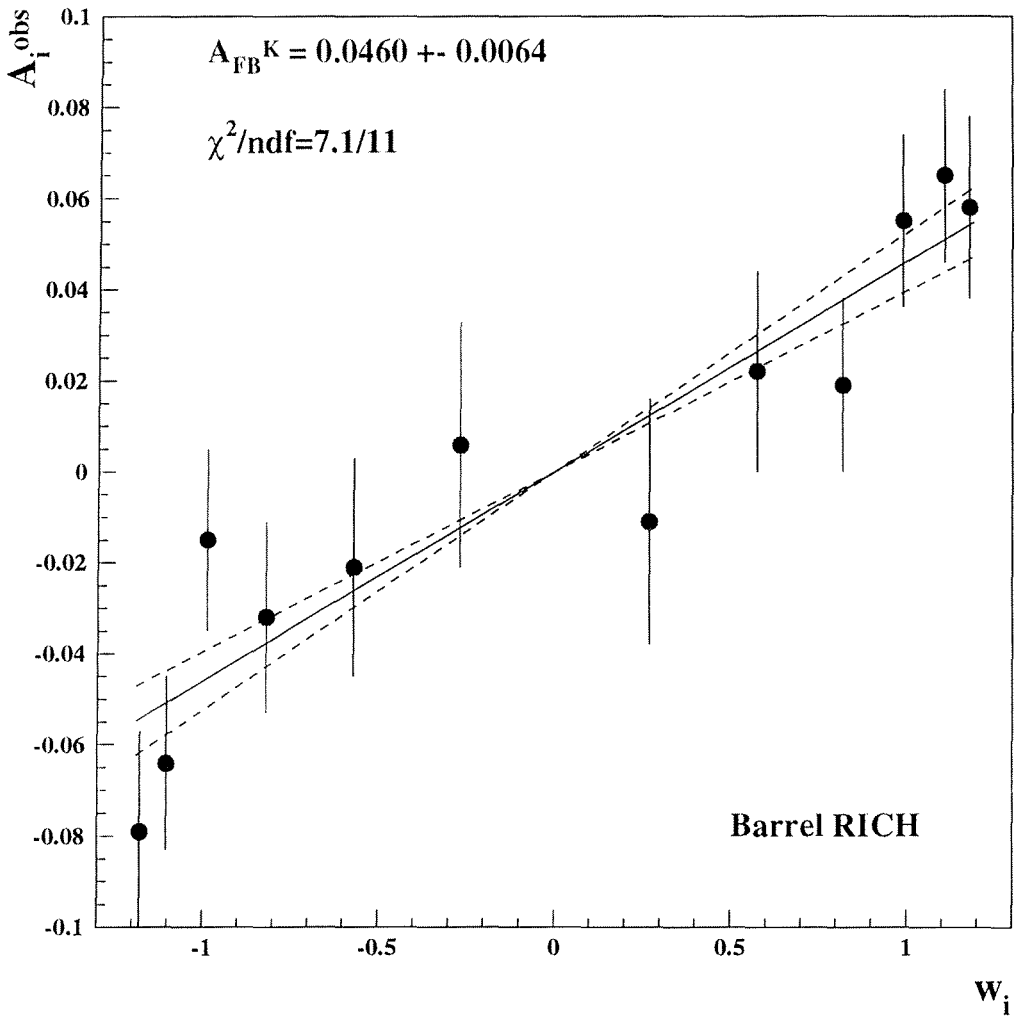

Figure 6.15: A_i^{obs} as a function of w_i (defined by equation 6.116) in the Barrel RICH, with the superimposed fitted function (solid line). The dashed line show the result of one standard deviation.

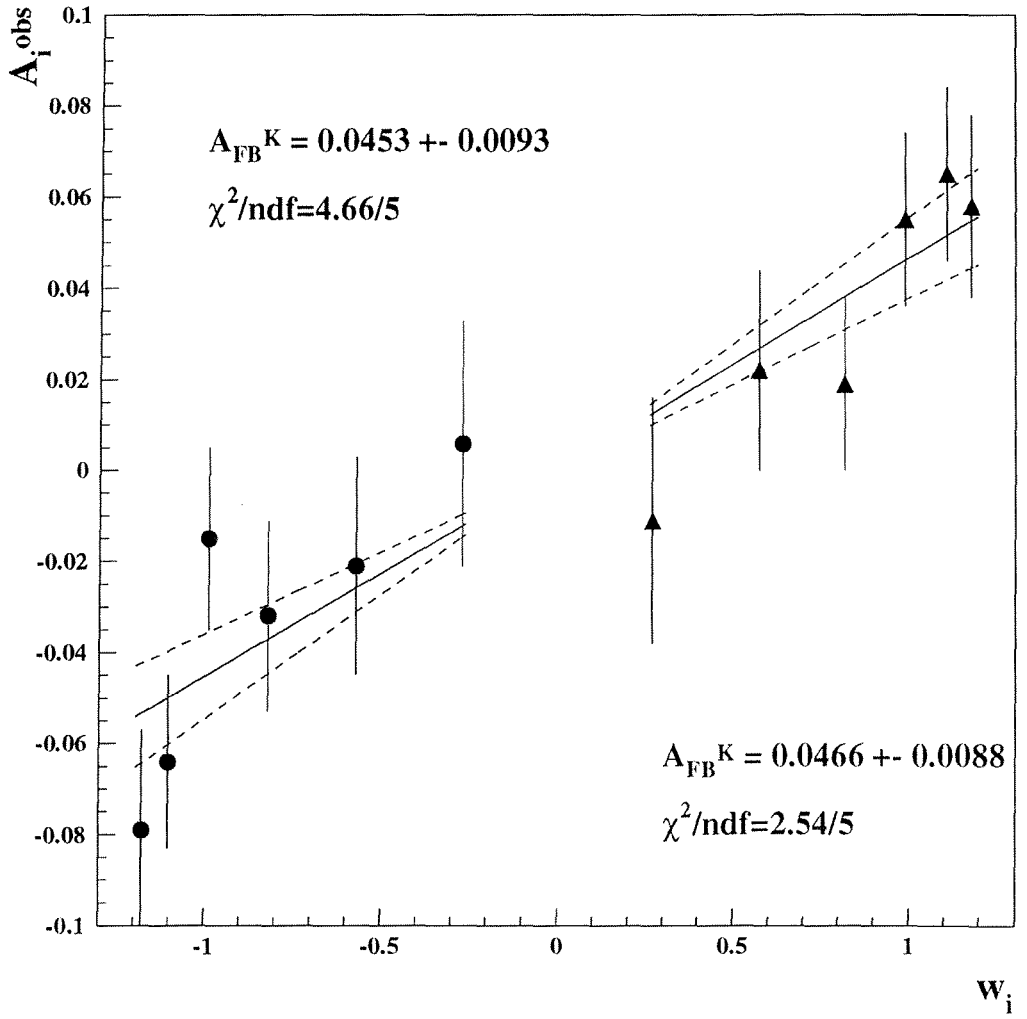

Figure 6.16: A_i^{obs} as a function of w_i (defined by equation 6.116) in the Barrel RICH, separately for each hemisphere $z < 0$ and $z > 0$ with the superimposed fitted functions (solid line). The dashed lines show the result of one standard deviation.

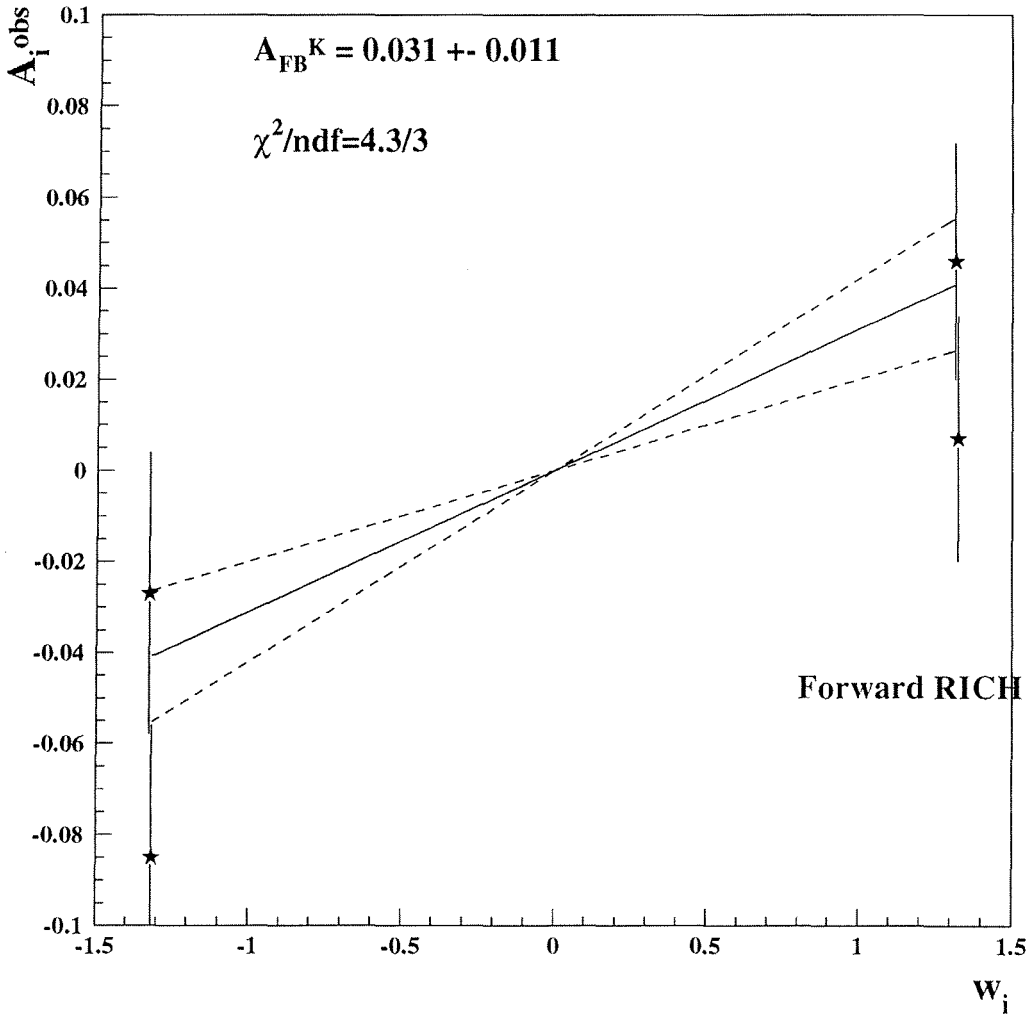

Figure 6.17: A_i^{obs} as a function of w_i (defined by equation 6.116) in the Forward RICH, with the superimposed fitted function (solid line). The dashed lines show the result of one standard deviation.

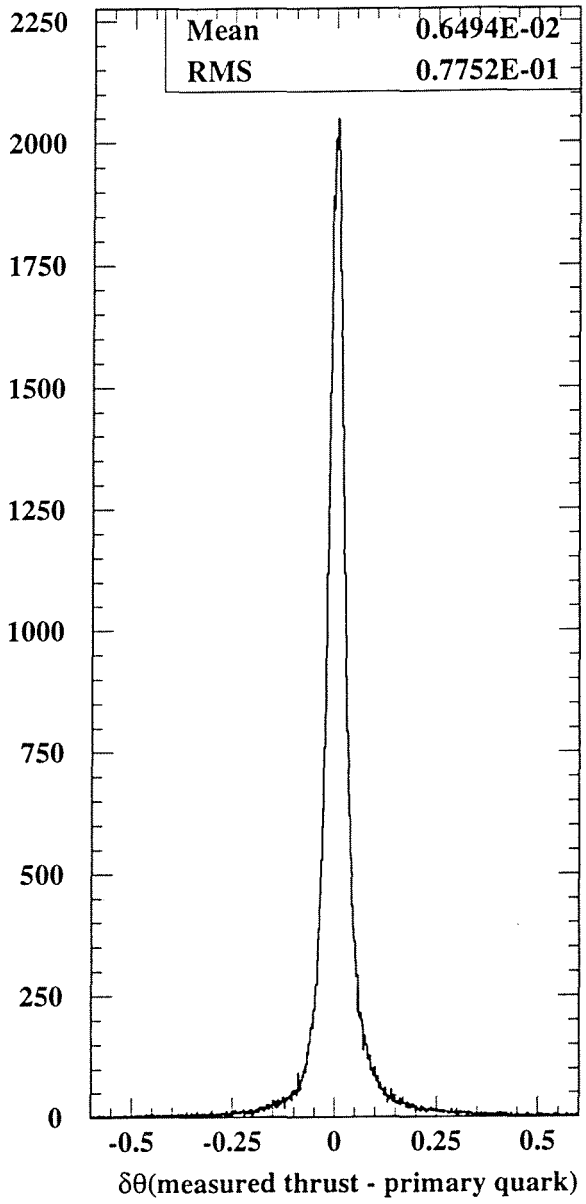

Figure 6.18: Difference between the the polar angle of the primary quark and the polar angle made by the measured thrust axis (oriented in the direction of the primary quark).

Bibliography

[1] DELPHI Coll., P. Abreu et al., *Z. Phys.* **C67** (1995) 1.

[2] DELPHI report 95-151 PHYS 573. (contribution to EPS-HEP-95 Brussels)

[3] R.M. Barnett et al., *Phys. Rev.* **D54** (1996) 1.

[4] DELPHI Coll., P. Abreu at al., *Nucl. Inst. and Meth.* **A378** (1996) 57.

[5] T. Sjostrand, *Comp. Phys. Comm.* **82** (1994) 74.

[6] DELPHI Coll., P. Abreu et al., *Z. Phys.* **C73** (1996) 11.

[7] DELPHI report 96-103 RICH 89 (1996)

[8] P. Abreu et al., DELPHI Coll., *Nucl. Phys.* **B444** (1995) 3. ;
D. Buskulic et al., ALEPH Coll., *Z. Phys.* **C66** (1995) 355. ;
R. Ackers et al., OPAL Coll., *Z. Phys.* **C63** (1994) 181.

[9] P. Abreu et al., DELPHI Coll., *Z. Phys.* **C73** (1996) 11.

[10] P. Abreu et al., DELPHI Coll., *Phys. Lett.* **B347** (1995) 447.

[11] E. Schyns thesis, *"Measurement of $\pi^{\pm}$, $K^{\pm}$, $p(\bar{p})$ production in $Z^0 \to q\bar{q}$, $Z^0 \to b\bar{b}$, and $Z^0 \to u\bar{u}, d\bar{d}, s\bar{s}$ - Particle identification with the DELPHI Barrel Ring Imaging Cherenkov Counter."*, University of Wuppertal (1997).

[12] P.Pages thesis, *"Etude de la production inclusive de mesons ϕ^0 et mesure du rapport de branchement du boson Z^0 en paires etranges aupres de l'experience DELPHI au LEP."*, Universite Louis Pasteur, Strasbourg (1996).

[13] E. Markus thesis, *"Messung der Vorwärts- Rückwärts-Asymmetrien für Charm- und Bottom- Quarks bei Energien nahe der Z-Resonanz."*, University of Wuppertal (1996).

[14] P. Abreu et al., *Nucl. Instr. and Meth.* **A378** (1996) 57.

[15] D. Bardin et al., *Z. Phys.* **C44** (1989) 493. ;
D. Bardin et al., *Comp. Phys. Comm.* **59** (1990) 303. ;
D. Bardin et al., *Nucl. Phys.* **B351** (1991) 1. ;
D. Bardin et al., *Phys. Lett.* **B255** (1991) 290. ;
D. Bardin et al., CERN report CERN-TH 6443/92 (1992).

[16] DELPHI note 97-115 CONF 97 (1997).

[17] LEPWWG/96-02, ALEPH 96-107 PHYSIC 96-98, DELPHI 96-121 PHYS 631, L3 Note 1975, OPAL Technical Note TN 399, SLD Physics Note 52 (1996) ;
The LEP Collaborations, ALEPH, DELPHI, L3, OPAL and the LEP Electroweak Working Group, CERN-PPE/95-172 (1995).

[18] LEPHF/96-01, ALEPH 96-099, DELPHI 96-67 PHYS 627, L3 Note 1969, OPAL Technical Note TN 391 (1996).

[19] The LEP Collaborations, Contributions of the LEP experiments to the ICHEP, Warsaw, 25-31 July (1996), CERN-PPE/96-183 (1996).

[20] H. Albrecht et al., ARGUS Coll., *Z. Phys.* **C62** (1994) 371.

[21] P.Abreu et al., DELPHI Coll., *Z. Phys.* **C66** (1995) 323.

[22] *Eine genaue Bestimmung der Ladungsseparation : Systematische Untersuchung des Einflusses von Fragmentationseffekten und ihre Beschreibung durch Monte Carlo Modelle*, Diploma thesis presented at Bergische Universitat, Wuppertal (1995).

[23] F. James, M. Goosens, *MINUIT, Function Minimisation and Error Analysis*, Reference Manual, CERN Program Library Long Writeup **D506** (1992).

[24] P. Abreu et al., DELPHI Coll., *Z. Phys.* **C65** (1995) 587.

[25] Y.J. Pei, L3 Coll., *"Studies of meson production in Z decays"*, CERN Seminar, September 6 1994 (not published).

[26] D. Buskulic et al., ALEPH Coll., *Z. Phys.* **C64** (1994) 361.

[27] R. Akers et al., OPAL Coll., *Z. Phys.* **C67** (1995) 389.

[28] D. Buskulic et al., ALEPH Coll., *Z. Phys.* **C66** (1995) 355.

[29] P. Abreu et al., DELPHI Coll., *Nucl. Phys.* **B444** (1995) 3.

[30] R. Akers et al., OPAL Coll., *Z. Phys.* **C63** (1994) 181.

[31] D. Buskulic et al., ALEPH Coll., *Z. Phys.* **C69** (1996) 379;
Holger Hepp, Diplomarbeit, HD-IHEP 93-04, Heidelberg (1993).

[32] R. Akers et al., OPAL Coll., *Z. Phys.* **C68** (1995) 1.

[33] P. Abreu et al., DELPHI Coll., *Z. Phys.* **C67** (1995) 543.

Chapter 7

Conclusion

The Standard Model which describes the strong and electroweak interactions predicts a forward-backward asymmetry in the final state of the e^+e^- collisions at the Z^0 pole.
This thesis, based on 1.35×10^6 hadronic Z^0 events collected by the DELPHI detector at LEP during 1994, presents for the first time in details a complete study of the determination of this asymmetry in the case of the process :

$$e^+e^- \rightarrow Z^0 \rightarrow s\bar{s}$$

This process which lies within the light quark sector is, until now, only poorly investigated because of the experimental difficulty to isolate a sample of such events with relatively **high purity** :

- **In the barrel region**, our method of enrichment which exploits the Vertex Detector in association with the Ring Imaging CHerenkov (Barrel RICH) detector allowed to reach a purity never attained of about **55%**.
- **In the forward region**, although the procedure used to reduce the contamination of heavy quark events can not be applied because of the little overlap of the Forward RICH with the acceptance of the Vertex Detector, we reached a purity of **43%**.

The measurement of the $s\bar{s}$ asymmetry was deduced from the angular distribution of the **high momentum charged K mesons** ($10 < p < 24$ GeV/c) which have been **individually identified** by means of the **RICH detectors** of DELPHI. For this purpose, the performances of such detectors have been extensively studied.
The method has the advantage of using charged states, because of the relative tight relation expected between the identified K^- (K^+) with the primary s ($\bar{s}$).

The charged kaon asymmetry evaluated experimentally has been corrected for two effects :

- the contamination of the sample of identified charged kaons by pions;
- the fake asymmetry induced by the fact that K^+ and K^- are differently absorbed by the detector material.

The method to extract the $s\bar{s}$ asymmetry from the resulting charged kaons asymmetry allowed us to obtain a precise value for the $s\bar{s}$ asymmetry at the Z^0 pole. The following result is obtained (see (6.51)) :

$$A^0_{s\bar{s}} = 0.114 \pm 0.019(stat.) \pm 0.005(syst.)$$

The present result can be compared to the measurement of $A^0_{s\bar{s}}$ on 1992 data to which we have contributed and which is already published in [2] :

$$A^0_{s\bar{s}} = 0.131 \pm 0.035(stat.) \pm 0.013(syst.)$$

No significant difference is observed between both measurements at 1 σ level.

The measurement of $A^0_{s\bar{s}}$ provides :

- a test of the universality of the electroweak coupling constants which predicts the same asymmetry for s-quark and b-quark. Comparing our result with the $b\bar{b}$ pole asymmetry obtained at LEP [1] :

$$A^0_{b\bar{b}} = 0.0979 \pm 0.0023$$

we notice that the measurements are compatible within one standard deviation.

- a sensitive determination of $\sin^2\theta_{eff}$ (see section 4.4) which corresponds to :

$$\sin^2\theta_{eff} = 0.2296 \pm 0.0035$$

To be compared to the world average [3] : $\sin^2\theta_w = 0.2315(4)$. On figure 7.1, we show the comparison between the measurements of $A^0_{s\bar{s}}$ performed on 1992 and 1994 data, and the Standard Model prediction (using the simulation program ZFITTER with $m_{top} = 175$ GeV/c^2). It is clearly seen that our result is more precise and compatible with the Standard Model predictions.

Compared to the 1992 measurement, our new analysis presents the following **advantages** :

- it exploits the originality of the **DELPHI** detector to be **the only LEP experiment equipped with RICH detectors.**

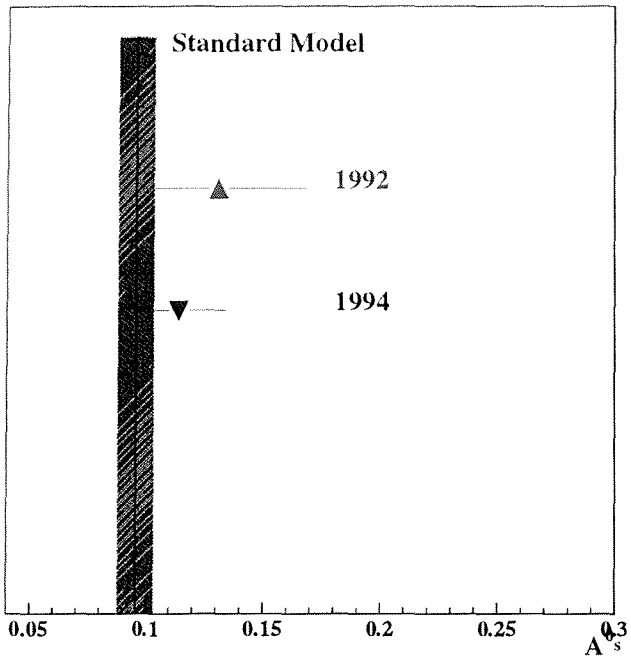

Figure 7.1: Comparison between the $A^0_{s\bar{s}}$ measurement on 92 data, 94 data and the Standard Model prediction.

• it presents the first measurement which uses the capability of the DELPHI detector to **identify charged particles** particularly **in the forward region**, region which is favoured from a statistical point of view by the cross-section and where the evaluation of the asymmetry is more sensitive.

• it has been performed on 1.35×10^6 hadronic Z^0 events registered in 1994, period during which the **largest statistics with a fully operational RICH** detector (Barrel RICH and Forward RICH) was recorded.

• it allows to use a purer sample of $s\bar{s}$ events by the exploitation of the Brown and Frank algorithm in the barrel region.

We have investigated the **improvements** which could still be brought to the present analysis :

• In order **to improve the precision** on the measurement of $A^0_{s\bar{s}}$, we have considered the possibility to extend the present method to the whole statistics collected by the DELPHI detector at the Z^0 pole between 1992 and

1995 with operational RICH detectors. This would lead to a decrease of the statistical error by about 30% but at the expense of a thorough study of the systematics specific to each data taking period.

• One could think of selecting hadronic $s\bar{s}$ events by requiring the presence of two high momentum charged kaon of opposite charge, one in each hemisphere. This would lead to an enriched sample of $s\bar{s}$ events with purity as high as 60% but this advantage would be largely watch out by the considerable reduction of the statistics (of a factor ~ 20).

The result presented in the present thesis is already the subject of a DELPHI paper [4] which was submitted to the HEP'97 Conference at Jerusalem in August 1997.

Bibliography

[1] The LEP Collaborations, Contributions of the LEP experiments to the ICHEP, Warsaw, 25-31 July (1996), CERN-PPE/96-183 (1996).

[2] P. Abreu et al., DELPHI Coll., *Z. Phys.* **C67** (1995) 1.

[3] R.M. Barnett et al., *Physical Review* **D54** (1996) 1.

[4] DELPHI note 97-115 CONF 97

Appendix A

Matrix representation

The metric tensor is :

$$g_{\mu\nu} = g^{\mu\nu} = \begin{pmatrix} 1 & 0 & 0 & 0 \\ 0 & -1 & 0 & 0 \\ 0 & 0 & -1 & 0 \\ 0 & 0 & 0 & -1 \end{pmatrix} \tag{A.1}$$

Derivatives with respect to contravariant or covariant coordinates are abbreviates as :

$$\partial_\mu \equiv \frac{\partial}{\partial x^\mu} \tag{A.2}$$

$$\partial^\mu \equiv \frac{\partial}{\partial x_\mu} \tag{A.3}$$

The Pauli matrices are :

$$\tau^1 = \begin{pmatrix} 0 & 1 \\ 1 & 0 \end{pmatrix} \quad \tau^2 = \begin{pmatrix} 0 & -i \\ i & 0 \end{pmatrix} \quad \tau^3 = \begin{pmatrix} 1 & 0 \\ 0 & -1 \end{pmatrix} \tag{A.4}$$

In the Dirac representation, the γ matrices are defined in the following way :

$$\gamma^0 = \begin{pmatrix} \mathbf{1} & 0 \\ 0 & -\mathbf{1} \end{pmatrix} \quad \gamma^k = \begin{pmatrix} 0 & \tau^k \\ -\tau^k & 0 \end{pmatrix} \quad (k = 1, 2, 3) \tag{A.5}$$

where $\mathbf{1}$ is the unit matrix :

$$\begin{pmatrix} 1 & 0 \\ 0 & 1 \end{pmatrix} \tag{A.6}$$

We also have :

$$\gamma^5 \equiv i\gamma^0\gamma^1\gamma^2\gamma^3 = \begin{pmatrix} 0 & \mathbf{1} \\ \mathbf{1} & 0 \end{pmatrix} \tag{A.7}$$

Appendix B

JETSET PS Parameters

The JETSET 7.3 PS input parameters as optimised in the DELPHI experiment are listed in the following table. For a detailed definition of these parameters, the reader is sent to [1].

Parameter	Reference Value	Range
Λ_{QCD}	0.4	0.25 - 0.35
Cut-off value Q_0 of parton	1.0	1.0 - 2.0
Param. a of Lund fragm. funct.	0.5	0.1 - 0.5
Param. b of Lund fragm. funct.	0.9	0.844
σ_q	0.35	0.36 - 0.44
$P(^1S_0)_{ud}$	0.5	0.3 - 0.5
$P(^3S_1)_{ud}$	0.5	0.2 - 0.4
Supp. of $s\bar{s}$ pair prod. γ_s/γ_u	0.30	0.27 - 0.31
$P(^1S_0)_s$	0.4	0.3 - 0.5
$P(^3S_1)_s$	0.6	0.2 - 0.4
Param. ϵ_c of Peterson fragm. funct.	-	variable
$P(^1S_0)_c$	0.25	0.26
$P(^3S_1)_c$	0.75	0.44
$P(Pstates)_c$	0.	0.3
Param. ϵ_b of Peterson fragm. funct.	-	variable
$P(^1S_0)_b$	0.25	0.175
$P(^3S_1)_b$	0.75	0.525
$P(Pstates)_b$	0.	0.3
Supp. of strange diquark prod. $(\gamma_{us}/\gamma_{ud})/(\gamma_s/\gamma_d)$	0.34	0.27 - 0.41
extra supp. factor for η prod.	1.0	0.65
extra supp. factor for η' prod.	1.0	0.23

[1] T. Sjostrand, *Comp. Phys. Comm.* **82** (1994) 74 and DELPHI Coll.,

P. Abreu et al., *Z. Phys.* **C73** (1996) 11.